



HAL
open science

CLASSY IV. Exploring UV Diagnostics of the Interstellar Medium in Local High-z Analogs at the Dawn of the JWST Era

Matilde Mingozzi, Bethan L. James, Karla Z. Arellano-Córdova, Danielle A. Berg, Peter Senchyna, John Chisholm, Jarle Brinchmann, Alessandra Aloisi, Ricardo O. Amorín, Stéphane Charlot, et al.

► **To cite this version:**

Matilde Mingozzi, Bethan L. James, Karla Z. Arellano-Córdova, Danielle A. Berg, Peter Senchyna, et al.. CLASSY IV. Exploring UV Diagnostics of the Interstellar Medium in Local High-z Analogs at the Dawn of the JWST Era. *The Astrophysical Journal*, 2022, 939, 10.3847/1538-4357/ac952c . hal-03974058

HAL Id: hal-03974058

<https://hal.science/hal-03974058v1>

Submitted on 7 Feb 2023

HAL is a multi-disciplinary open access archive for the deposit and dissemination of scientific research documents, whether they are published or not. The documents may come from teaching and research institutions in France or abroad, or from public or private research centers.

L'archive ouverte pluridisciplinaire **HAL**, est destinée au dépôt et à la diffusion de documents scientifiques de niveau recherche, publiés ou non, émanant des établissements d'enseignement et de recherche français ou étrangers, des laboratoires publics ou privés.



Distributed under a Creative Commons Attribution 4.0 International License



CLASSY IV. Exploring UV Diagnostics of the Interstellar Medium in Local High- z Analogs at the Dawn of the JWST Era*

Matilde Mingozzi¹, Bethan L. James², Karla Z. Arellano-Córdova³, Danielle A. Berg³, Peter Senchyna⁴, John Chisholm³, Jarle Brinchmann⁵, Alessandra Aloisi¹, Ricardo O. Amorín^{6,7}, Stéphane Charlot⁸, Anna Feltre⁹, Matthew Hayes¹⁰, Timothy Heckman¹¹, Alaina Henry^{1,11}, Svea Hernandez², Nimisha Kumari², Claus Leitherer¹, Mario Llerena^{6,7}, Crystal L. Martin¹², Themiya Nanayakkara¹³, Swara Ravindranath¹, Evan D. Skillman¹⁴, Yuma Sugahara^{15,16,17}, Aida Wofford¹⁸, and Xinfeng Xu¹¹

¹ Space Telescope Science Institute, 3700 San Martin Drive, Baltimore, MD 21218, USA; mmingozzi@stsci.edu

² AURA for ESA, Space Telescope Science Institute, 3700 San Martin Drive, Baltimore, MD 21218, USA

³ Department of Astronomy, The University of Texas at Austin, 2515 Speedway, Stop C1400, Austin, TX 78712, USA

⁴ Carnegie Observatories, 813 Santa Barbara Street, Pasadena, CA 91101, USA

⁵ Instituto de Astrofísica e Ciências do Espaço, Universidade do Porto, CAUP, Rua das Estrelas, PT4150-762 Porto, Portugal

⁶ Instituto de Investigación Multidisciplinar en Ciencia y Tecnología, Universidad de La Serena, Raul Bitrán 1305, La Serena 2204000, Chile

⁷ Departamento de Astronomía, Universidad de La Serena, Av. Juan Cisternas 1200 Norte, La Serena 1720236, Chile

⁸ Sorbonne Université, CNRS, UMR7095, Institut d'Astrophysique de Paris, F-75014, Paris, France

⁹ INAF—Osservatorio di Astrofisica e Scienza dello Spazio di Bologna, Via P. Gobetti 93/3, I-40129 Bologna, Italy

¹⁰ Stockholm University, Department of Astronomy and Oskar Klein Centre for Cosmoparticle Physics, AlbaNova University Centre, SE-10691, Stockholm, Sweden

¹¹ Center for Astrophysical Sciences, Department of Physics & Astronomy, Johns Hopkins University, Baltimore, MD 21218, USA

¹² Department of Physics, University of California, Santa Barbara, Santa Barbara, CA 93106, USA

¹³ Swinburne University of Technology, Melbourne, Victoria, AU, Australia

¹⁴ Minnesota Institute for Astrophysics, University of Minnesota, 116 Church Street SE, Minneapolis, MN 55455, USA

¹⁵ Institute for Cosmic Ray Research, The University of Tokyo, Kashiwa-no-ha, Kashiwa 277-8582, Japan

¹⁶ National Astronomical Observatory of Japan, 2-21-1 Osawa, Mitaka, Tokyo 181-8588, Japan

¹⁷ Waseda Research Institute for Science and Engineering, Faculty of Science and Engineering, Waseda University, 3-4-1, Okubo, Shinjuku, Tokyo 169-8555, Japan

¹⁸ Instituto de Astronomía, Universidad Nacional Autónoma de México, Unidad Académica en Ensenada, Km 103 Carr. Tijuana-Ensenada, Ensenada 22860, México

Received 2022 June 6; revised 2022 September 1; accepted 2022 September 20; published 2022 November 11

Abstract

The Cosmic Origins Spectrograph (COS) Legacy Archive Spectroscopic SurveY (CLASSY) provides the first high-resolution spectral catalog of 45 local high- z analogs in the ultraviolet (UV; 1200–2000 Å) to investigate their stellar and gas properties. Here we present a toolkit of UV interstellar medium (ISM) diagnostics, analyzing the main emission lines of CLASSY spectra (N IV] $\lambda\lambda$ 1483,87, C IV $\lambda\lambda$ 1548,51, He II λ 1640, O III] $\lambda\lambda$ 1661,6, Si III] $\lambda\lambda$ 1883,92, C III] λ 1907,9). Specifically, our aim is to provide accurate diagnostics for the reddening $E(B - V)$, electron density n_e , electron temperature T_e , metallicity $12 + \log(\text{O}/\text{H})$, and ionization parameter $\log(U)$, taking the different ISM ionization zones into account. We calibrate our UV toolkit using well-known optical diagnostics, analyzing archival optical spectra for all CLASSY targets. We find that UV density diagnostics estimate n_e values that are ~ 1 – 2 dex higher (e.g., $n_e(\text{C III}] \lambda\lambda$ 1907,9) $\sim 10^4 \text{ cm}^{-3}$) than those inferred from their optical counterparts (e.g., $n_e(\text{S II}] \lambda\lambda$ 6717,31) $\sim 10^2 \text{ cm}^{-3}$; $n_e(\text{Ar IV}] \lambda\lambda$ 4714,41) $\sim 10^3 \text{ cm}^{-3}$). T_e derived from the hybrid ratio [O III] λ 1666/ λ 5007 proves to be reliable, implying differences in determining $12 + \log(\text{O}/\text{H})$ compared to the optical counterpart O III] λ 4363/[O III] λ 5007 within $\sim \pm 0.3$ dex. We also investigate the relation between the stellar and gas $E(B - V)$, finding consistent values at high specific star formation rates (sSFRs; $\log(\text{sSFR}) \gtrsim -8 \text{ yr}^{-1}$), while at low sSFRs we confirmed an excess of dust attenuation in the gas. Finally, we investigate UV line ratios and equivalent widths to provide correlations with $12 + \log(\text{O}/\text{H})$ and $\log(U)$, but note that there are degeneracies between the two. With this suite of UV-based diagnostics, we illustrate the pivotal role CLASSY plays in understanding the chemical and physical properties of high- z systems that JWST can observe in the rest-frame UV.

Unified Astronomy Thesaurus concepts: Dwarf galaxies (416); Ultraviolet astronomy (1736); Galaxy chemical evolution (580); Galaxy spectroscopy (2171); High-redshift galaxies (734); Emission line galaxies (459)

1. Introduction

The galaxies that host a substantial fraction of the star formation (SF) in the high- z universe ($z \gtrsim 6$) and likely play a key

role in the reionization era tend to be compact, metal-poor, with a low-mass and large specific star formation rates (sSFRs; e.g., Wise et al. 2014; Madau & Haardt 2015; Robertson et al. 2015; Stanway et al. 2016; Stark 2016). Deep rest-frame UV spectra of several of these high-redshift galaxies ($z \sim 5 - 7$) already revealed prominent high-ionization nebular emission lines, such as He II λ 1640, O III] $\lambda\lambda$ 1661, 66, [C III] λ 1907 and C III] λ 1909 (C III] hereafter), and C IV $\lambda\lambda$ 1548, 1551 (C IV hereafter; e.g., Stark et al. 2015; Mainali et al. 2017, 2018). In the upcoming era of the James Webb Space Telescope (JWST) and extremely large telescopes (ELTs), the UV spectroscopic frontier is pushed to higher redshifts than ever before, finally

* Based on observations made with the NASA/ESA Hubble Space Telescope, obtained from the Data Archive at the Space Telescope Science Institute, which is operated by the Association of Universities for Research in Astronomy, Inc., under NASA contract NAS 5-26555.

revealing detailed rest-frame UV observations of statistically significant samples of galaxies in the distant universe. As such, the time to sharpen our understanding of UV nebular emission and exploit its diagnostic power is upon us.

Far- and near-ultraviolet (FUV, $\sim 1200\text{--}1700 \text{ \AA}$; NUV, $\sim 1700\text{--}2000 \text{ \AA}$) spectra can foster our understanding of star-forming galaxies in terms of the stellar populations hosting massive stars and their impact on the interstellar medium (ISM) physical conditions, chemical evolution, feedback processes, and reionization. Due to the line production mechanisms alone, nebular UV emission can be used to *directly* calculate the physical and chemical conditions under which they are produced. For instance, both C III] and [Si III] $\lambda 1883$, [Si III] $\lambda 1892$ (Si III] hereafter) doublets are direct tracers of the electron density (Jaskot & Ravindranath 2016; Gutkin et al. 2016; Byler et al. 2018), the line intensity ratio C III]/O III] $\lambda 1666$ can be used to estimate the elemental carbon abundances (Garnett et al. 1995; Berg et al. 2016; Pérez-Montero & Amorín 2017; Berg et al. 2018), and He II $\lambda 1640$ and the C IV/C III] ratio both have the potential to constrain the level of ionization (Feltre et al. 2016). Moreover, the combination of all these UV lines can provide information about the nature of the ionizing sources in general (Feltre et al. 2016; Gutkin et al. 2016; Jaskot & Ravindranath 2016; Nakajima et al. 2018). UV emission lines therefore have the capacity to provide the community with a “diagnostic toolkit”, with which we can directly diagnose the ISM properties in star-forming galaxies.

Due to the intrinsic faintness of several UV emission lines, an alternative form of “*indirect*” diagnostics, which evolve from empirical calibrations between ISM conditions (e.g., metallicity) and properties of the stronger emission-line properties (e.g., equivalent widths of C III]), is also needed. To this end, several past studies have taken big steps forward in the interpretation of UV emission in the local universe. For example, Rigby et al. (2015) showed that C III] can be used to pick out low-metallicity galaxies with strong bursts of SF, whereas Senchyna et al. (2017) suggested that nebular He II and C IV emission has the potential to constrain metallicity. Additionally, Senchyna et al. (2019) demonstrated that C IV emission is ubiquitous in extremely metal-poor systems with very high sSFRs—albeit with equivalent widths smaller than those measured at high- z . With regards to the strength of the ionizing radiation, Ravindranath et al. (2020) found a strong correlation between C III] and O III] emission and the O32 ratio (a proxy for the ionization parameter), confirming that a hard radiation field is required to produce the high-ionization nebular lines. Using two nearby extreme UV emitting galaxies, Berg et al. (2019a) showed us that a combination of strong C IV and He II emission may identify galaxies that not only produce but also transmit a substantial number of high-energy photons—i.e., potential contributors to cosmic reionization (see also Schaerer et al. 2022). While each of these studies provided a significant step forward in understanding the conditions required for UV emission, these works have been limited to single peculiar objects or small nearby samples and lack the large statistics that we need to interpret the high volume of high- z UV spectroscopy that will arrive in the next decade.

Statistically larger rest-UV spectroscopic studies do exist, typically targeting $2 < z < 4$ star-forming galaxies. For instance, using deep Very Large Telescope (VLT) Multi Unit Spectroscopic Explorer (MUSE) spectroscopy, Maseda et al. (2017) collected a sample of 17 unlensed C III] emitters at

$1.5 \lesssim z \lesssim 4$, which provided an unbiased sample toward the lowest-mass, bluest galaxies. Stacked spectra of 15 gravitationally lensed galaxies at redshifts $1.68 < z < 3.6$ from project MEGaSaURA by Rigby et al. (2018), produced a new spectral composite of star-forming galaxies at redshift $z \sim 2$, which clearly revealed strong C III] and Mg II $\lambda\lambda 2796, 2803$ as well as weaker lines, such as He II and Si III]. Llerena et al. (2022) exploited a broader representative sample of 217 C III] emitters ($\sim 30\%$ of the total sample) from the VANDELS survey (McLure et al. 2018), collecting main-sequence galaxies at $z \sim 2\text{--}4$ to investigate their average properties using the spectral-stacking technique. Finally, Schmidt et al. (2021) presented an even larger sample, collecting 2052 spectroscopically confirmed emission-line galaxies at $1.5 \lesssim z \lesssim 6.4$, providing line properties of the main UV lines and subsequently confirming the wealth of information and physical properties that rest-frame UV emission features redward of Ly α can probe. These works currently represent our most comprehensive rest-FUV spectral data sets at high redshift. However, the majority of them have focused mainly on C III] emitters, as C III] is the strongest UV emission line after Ly α , and it is extremely challenging to obtain the required high signal-to-noise ratio (S/N) to detect fainter lines even employing the stacking technique. Moderate spectral resolution ($R \sim 18000$) and broad wavelength coverage are also necessary to fully investigate the potential of UV diagnostics. Also, the limited wavelength range available for each of these studies has prevented us from carrying out a comparison of multiwavelength diagnostics for the ISM properties within the same targets.

Indeed, in order for us to derive an accurate and detailed UV toolkit, we not only need to cover the full UV regime but also optical wavelengths. Historically, ISM tracers have relied heavily on optical diagnostics, and as such they are very well calibrated. A crucial step in understanding the conditions that produce UV emission would therefore be comparing UV line strengths with ISM conditions derived from preexisting optical diagnostics within the same targets, to effectively calibrate a toolkit that depends solely on UV emission lines. This aspect is particularly important because the entire optical wavelength range on which our current diagnostic toolkit relies (from [O II] $\lambda\lambda 3727, 9$ to [S III] $\lambda 9069$), which is easily accessible in the local universe, will not be available for sources in the reionization epoch. Specifically, JWST instruments such as NIRSpec will cover blueward of 7000 \AA and 4500 \AA only in objects between $z \sim 6$ and $z \sim 10$, respectively. As such, a UV toolkit will be essential for characterizing and interpreting the spectroscopic observations of high- z systems.

The ideal framework from which a UV toolkit can be built would consist of high S/N spectra with the possibility of extensive wavelength coverage that spans UV-to-optical wavelengths. Each of these essential elements are offered by local high- z analogs. In this context, the Cosmic Origins Spectrograph (COS) Legacy Spectroscopic Survey (CLASSY) treasury (Berg et al. 2022; James et al. 2022, Paper I and Paper II hereafter) represents the first high-quality ($S/N_{1500\text{\AA}} \gtrsim 5$ per resolution element, resel), high-resolution ($R \sim 15,000$), and broad-wavelength range ($\sim 1200\text{--}2000 \text{ \AA}$) UV database of 45 nearby ($0.002 < z < 0.182$) star-forming galaxies. These objects were selected to include properties similar to reionization-era systems, in terms of the sSFR, direct gas-phase metallicity, ionization level, reddening, and nebular density (see Paper I for more details). Moreover, optical observations

are in hand for all the galaxies of the sample, allowing us to make detailed comparisons of UV and optical diagnostics. As such, CLASSY provides the ideal UV atlas with which we can tailor our UV diagnostic toolkit.

This is the first in a series of two CLASSY papers in which we present a FUV-based toolkit and show how this compares to well-known optical diagnostics. Specifically, in this work we provide detailed calculations of dust attenuation, the electron density n_e , the electron temperature T_e , the gas-phase metallicity $12+\log(\text{O}/\text{H})$, and the ionization parameter $\log(U)$, using both UV and optical direct diagnostics, taking the different ionization zones of the ISM into account. Then, from their comparison, we provide a set of diagnostic equations to estimate ISM properties only from UV emission lines. In Section 2 we describe the CLASSY sample, covering both the UV and optical data, while in Section 3 we present the spectroscopic analysis, including stellar-continuum and emission-line fitting. In Section 4 we discuss the chemical and physical diagnostics used in our analysis, showing and comparing the derived ISM properties in Section 5. Then, in Section 6, we introduce and discuss our UV-based toolkit, providing also a comparison with previous works. Finally, in Section 7 we summarize our main findings.

The data presented in this paper were obtained from the Mikulski Archive for Space Telescopes (MAST) at the Space Telescope Science Institute. The specific observations analyzed can be accessed via [10.17909/m3fq-jj25](https://archive.stsci.edu/m3fq-jj25). All the products of this paper (UV and optical line fluxes; UV and optical z ; UV–optical flux offsets; ISM properties, i.e., $E(B - V)$, n_e , T_e , optical and UV $12+\log(\text{O}/\text{H})$) will be provided on the [CLASSY MAST webpage](#) as downloadable tables. In Appendices B, C, and D we show which information will be provided. Throughout this paper, we adopt the solar metallicity scale of Asplund et al. (2009), where $12+\log(\text{O}/\text{H})_{\odot} = 8.69$.

2. Sample Presentation

CLASSY is a sample of 45 star-forming UV-bright ($m_{\text{FUV}} < 21AB \text{ arcsec}^2$), relatively compact ($GF_{\text{WHM}}_{\text{NUV}} < 2''5$) galaxies in the local universe ($0.002 < z < 0.182$), spanning a wide range of stellar masses ($6.22 < \log(M_*/M_{\odot}) < 10.06$), star formation rates (SFRs; $-2 < \log(\text{SFR}/M_{\odot} \text{ yr}^{-1}) < +2$), oxygen abundances ($6.98 < 12+\log(\text{O}/\text{H}) < 8.77$), electron densities ($10 < n_e/\text{cm}^{-3} < 1120$), degree of ionization ($0.54 < \text{O3O2} < 38.0$, with $\text{O3O2} = [\text{O III}] \lambda 5007 / [\text{O II}] \lambda \lambda 3727,9$), and reddening values ($0.001 < E(B - V) < 0.673$). This broad sampling of the parameter space makes the CLASSY sample representative of star-forming galaxies across all redshifts, with a bias toward more extreme O3O2 values, low stellar masses, and high SFRs, typical of high- z systems (see Paper I). In Paper I, we presented our sample, explaining in detail the selection criteria and giving an extensive overview of the Hubble Space Telescope (HST) COS and archival optical spectra. To summarize, from the Hubble Spectral Legacy Archive (HSLA), 101 nearby ($z < 0.2$) galaxies were selected on the basis of the high S/N ($\gtrsim 7$ per 100 km s^{-1} resolution element) COS spectroscopy in at least one medium resolution grating (i.e., G130M, G160M, or G185M), applying further selection criteria to assemble a high-quality, comprehensive rest-frame set of FUV spectra for a large and diverse sample of star-forming galaxies. Specifically, any targets with secondary classifications or visually confirmed spectra features of quasi-stellar objects (QSO) or Seyferts were removed. The data reduction has been

presented in detail in Paper II, including spectra extraction, co-addition, wavelength calibration, and vignetting.

In this work, we account for the properties of the CLASSY galaxies in terms of the redshift, stellar mass, SFR, $12+\log(\text{O}/\text{H})$, and galaxy half-light radius (r_{50}), estimated from Paper I, which for completeness we also show in Table 1. Specifically, the redshifts have been taken from the Sloan Digital Sky Survey (SDSS), where available; r_{50} was estimated from Panoramic Survey Telescope And Rapid Response System (Pan-STARRS) imaging; while the stellar masses and SFRs have been estimated from the spectra energy distribution (SED) fitting via the Bayesian Analysis of GaLaxy sEds (BEAGLE; Chevallard & Charlot 2016), as explained in Paper I (see Section 4.7). Finally, the calculation of $12+\log(\text{O}/\text{H})$ is explained in detail in Paper I Section 4.5, and is based on the direct T_e method, using $[\text{S II}] \lambda 6717 / \lambda 6731$ and $[\text{O III}] \lambda 4363 / \lambda 5007$ as electron density and temperature tracers, respectively. The UV redshifts z_{UV} instead are obtained from the analysis of UV emission lines and are part of the results of this paper.

As described in Paper I, both UV and optical CLASSY spectra have been corrected for the total Galactic foreground reddening along the line of sight of their coordinates using the PYTHON dustmaps (Green 2018) interface to query the Bayestar 3D dust maps of Green et al. (2015). The Green et al. (2015) map was adopted over more recent versions due to its more optimal coverage of the CLASSY sample. Galactic foreground reddening correction was then applied using the Cardelli et al. (1989) reddening law.

In the following, we briefly summarize the UV and optical data sample and properties.

2.1. UV Data

CLASSY combines 135 orbits of new HST data (PID: 15840, PI: Berg) with 177 orbits of archival HST data, for a total of 312 orbits. In order to achieve nearly panchromatic FUV spectral coverage with the highest spectral resolution possible, CLASSY combines the G130M, G160M, G185M, G225M, and G140L gratings, spanning from 1150 \AA to $2100\text{--}2500 \text{ \AA}$ to allow synergistic co-spatial studies of stars and gas within the same galaxy.

Each HST/COS grating has a different spectral resolution that must be accounted for when combining data from multiple gratings. This co-addition process is explained in Section 2.3 of Paper I and in Paper II, which presents all the details of this multistage technical process, concerning extracting, reducing, aligning, and coadding the spectra from the different gratings. This paper focuses on the analysis of all the emission lines (except for $\text{Ly}\alpha$) in the range $1150\text{--}2000 \text{ \AA}$. We used the so-called *high-resolution* (HR: G130M+G160M; $R \sim 10,000\text{--}24,000$) and *moderate-resolution* (MR: G130M+G160M+G185M+G225M; $R \sim 10,000\text{--}20,000$) co-added spectra with a dispersion of $12.23 \text{ m\AA pixel}^{-1}$, and a resolution of 0.073 \AA per resolution element (\AA resel^{-1} , where 1 resel equates to 6 native COS pixels), and $33 \text{ m\AA pixel}^{-1}$ and $0.200 \text{ \AA resel}^{-1}$, respectively.

For galaxies J1044+0353 and J1418+2102, instead of the MR co-added spectra, we used the so-called *low-resolution* (LR: G130M+G160M+G140L or G130M+G160M+G185M+G225M+G140L; $R \sim 1500\text{--}4000$) co-adds, with a nominal point-source resolution of $80.3 \text{ m\AA pixel}^{-1}$ or $0.498 \text{ \AA resel}^{-1}$. Additionally, the COS G185M and G225M observations for

Table 1
CLASSY Sample Main Properties

Target	Name	$z_{\text{lit.}}$	Tot. $\log M_*$ z_{UV}	$\log \text{SFR}$ (M_{\odot})	($M_{\odot} \text{ yr}^{-1}$)	12+log(O/H)	r_{50}
1. J0021+0052		0.09839	...	$9.09^{+0.18}_{-0.38}$	$+1.07^{+0.14}_{-0.11}$	8.17 ± 0.07	0.784
2. J0036-3333	Haro 11 knot	0.02060	...	$9.14^{+0.26}_{-0.23}$	$+1.01^{+0.19}_{-0.21}$	8.21 ± 0.17	2.846
3. J0127-0619	Mrk 996	0.00540	0.00547	$8.74^{+0.18}_{-0.15}$	$-0.75^{+0.15}_{-0.13}$	7.68 ± 0.02	2.374
4. J0144+0453	UM133	0.00520	0.00533	$7.65^{+0.24}_{-0.29}$	$-0.81^{+0.29}_{-0.46}$	7.76 ± 0.02	2.851
5. J0337-0502	SBS0335-052 E	0.01352	0.01346	$7.06^{+0.24}_{-0.21}$	$-0.32^{+0.07}_{-0.11}$	7.46 ± 0.04	1.433
6. J0405-3648		0.00280	...	$6.61^{+0.28}_{-0.28}$	$-1.81^{+0.31}_{-0.27}$	7.04 ± 0.05	3.557
7. J0808+3948		0.09123	...	$9.12^{+0.30}_{-0.17}$	$+1.26^{+0.18}_{-0.25}$	8.77 ± 0.12	1.114
8. J0823+2806	LARS9	0.04722	0.04741	$9.38^{+0.33}_{-0.19}$	$+1.48^{+0.15}_{-0.32}$	8.28 ± 0.01	2.134
9. J0926+4427	LARS14	0.18067	0.18000	$8.76^{+0.30}_{-0.26}$	$+1.03^{+0.13}_{-0.13}$	8.08 ± 0.02	0.889
10. J0934+5514	I zw 18 NW	0.00250	0.00264	$6.27^{+0.15}_{-0.20}$	$-1.52^{+0.09}_{-0.07}$	6.98 ± 0.01	2.606
11. J0938+5428		0.10210	0.10210	$9.15^{+0.18}_{-0.29}$	$+1.05^{+0.29}_{-0.17}$	8.25 ± 0.02	1.095
12. J0940+2935		0.00168	...	$6.71^{+0.23}_{-0.40}$	$-2.01^{+0.42}_{-0.37}$	7.66 ± 0.07	5.151
13. J0942+3547	CG-274, SB 110	0.01486	0.01482	$7.56^{+0.21}_{-0.29}$	$-0.76^{+0.19}_{-0.12}$	8.13 ± 0.03	1.328
14. J0944-0038	CGCG007-025, SB 2	0.00478	0.00487	$6.83^{+0.44}_{-0.25}$	$-0.78^{+0.19}_{-0.16}$	7.83 ± 0.01	0.984
15. J0944+3442		0.02005	0.02005	$8.19^{+0.40}_{-0.23}$	$-0.01^{+0.28}_{-0.65}$	7.62 ± 0.11	2.458
16. J1016+3754	1427-52996-221	0.00388	0.00390	$6.72^{+0.27}_{-0.22}$	$-1.17^{+0.18}_{-0.18}$	7.56 ± 0.01	1.835
17. J1024+0524	SB 36	0.03319	0.03326	$7.89^{+0.37}_{-0.24}$	$+0.21^{+0.14}_{-0.12}$	7.84 ± 0.03	1.325
18. J1025+3622		0.12650	0.12717	$8.87^{+0.25}_{-0.27}$	$+1.04^{+0.14}_{-0.18}$	8.13 ± 0.01	0.843
19. J1044+0353		0.01287	0.01286	$6.80^{+0.41}_{-0.26}$	$-0.59^{+0.11}_{-0.14}$	7.45 ± 0.03	1.204
20. J1105+4444	1363-53053-510	0.02154	0.02147	$8.98^{+0.29}_{-0.24}$	$+0.69^{+0.28}_{-0.22}$	8.23 ± 0.01	2.646
21. J1112+5503		0.13164	...	$9.59^{+0.33}_{-0.19}$	$+1.60^{+0.20}_{-0.25}$	8.45 ± 0.06	0.920
22. J1119+5130		0.00446	0.00444	$6.77^{+0.15}_{-0.28}$	$-1.58^{+0.21}_{-0.12}$	7.57 ± 0.04	1.870
23. J1129+2034	SB 179	0.00470	0.00467	$8.09^{+0.37}_{-0.27}$	$-0.37^{+0.38}_{-0.56}$	8.28 ± 0.04	3.098
24. J1132+5722	SBSG1129+576	0.00504	0.00504	$7.31^{+0.23}_{-0.26}$	$-1.07^{+0.27}_{-0.27}$	7.58 ± 0.08	2.249
25. J1132+1411	SB 125	0.01764	0.01760	$8.68^{+0.28}_{-0.19}$	$+0.44^{+0.24}_{-0.27}$	8.25 ± 0.01	7.289
26. J1144+4012		0.12695	0.12700	$9.89^{+0.18}_{-0.29}$	$+1.51^{+0.20}_{-0.29}$	8.43 ± 0.20	1.158
27. J1148+2546	SB 182	0.04512	0.04522	$8.14^{+0.34}_{-0.24}$	$+0.53^{+0.17}_{-0.14}$	7.94 ± 0.01	0.874
28. J1150+1501	SB 126, Mrk 0750	0.00245	0.00246	$6.84^{+0.28}_{-0.30}$	$-1.33^{+0.29}_{-0.23}$	8.14 ± 0.01	1.760
29. J1157+3220	1991-53446-584	0.01097	0.01101	$9.04^{+0.32}_{-0.18}$	$+0.97^{+0.21}_{-0.42}$	8.43 ± 0.02	2.894
30. J1200+1343		0.06675	0.06699	$8.12^{+0.47}_{-0.42}$	$+0.75^{+0.20}_{-0.16}$	8.26 ± 0.02	0.908
31. J1225+6109	0955-52409-608	0.00234	0.00234	$7.12^{+0.34}_{-0.24}$	$-1.08^{+0.26}_{-0.26}$	7.97 ± 0.01	2.596
32. J1253-0312	SHOC391	0.02272	0.02267	$7.65^{+0.51}_{-0.23}$	$+0.56^{+0.15}_{-0.15}$	8.06 ± 0.01	1.079
33. J1314+3452	SB 153	0.00288	0.00282	$7.56^{+0.30}_{-0.21}$	$-0.67^{+0.23}_{-0.55}$	8.26 ± 0.01	1.765
34. J1323-0132		0.02246	0.02246	$6.31^{+0.26}_{-0.10}$	$-0.72^{+0.08}_{-0.09}$	7.71 ± 0.04	0.698
35. J1359+5726	Ly 52, Mrk 1486	0.03383	0.03381	$8.41^{+0.31}_{-0.26}$	$+0.42^{+0.20}_{-0.14}$	7.98 ± 0.01	1.395
36. J1416+1223		0.12316	...	$9.59^{+0.32}_{-0.26}$	$+1.57^{+0.21}_{-0.25}$	8.53 ± 0.11	0.985
37. J1418+2102		0.00855	0.00858	$6.22^{+0.49}_{-0.35}$	$-1.13^{+0.15}_{-0.16}$	7.75 ± 0.02	1.130
38. J1428+1653		0.18167	...	$9.56^{+0.15}_{-0.23}$	$+1.22^{+0.29}_{-0.29}$	8.33 ± 0.05	0.933
39. J1429+0643		0.17350	0.17340	$8.80^{+0.35}_{-0.21}$	$+1.42^{+0.11}_{-0.17}$	8.10 ± 0.03	0.859
40. J1444+4237	HS1442+4250	0.00230	0.00220	$6.48^{+0.17}_{-0.17}$	$-1.94^{+0.11}_{-0.08}$	7.64 ± 0.02	2.760
41. J1448-0110	SB 61	0.02741	0.02744	$7.61^{+0.41}_{-0.24}$	$+0.39^{+0.13}_{-0.14}$	8.13 ± 0.01	1.070
42. J1521+0759		0.09426	...	$9.00^{+0.29}_{-0.30}$	$+0.95^{+0.16}_{-0.17}$	8.31 ± 0.14	0.983
43. J1525+0757		0.07579	...	$10.06^{+0.28}_{-0.42}$	$+1.00^{+0.69}_{-0.24}$	8.33 ± 0.04	1.319
44. J1545+0858	1725-54266-068	0.03772	0.03772	$7.52^{+0.43}_{-0.26}$	$+0.37^{+0.13}_{-0.17}$	7.75 ± 0.03	1.075
45. J1612+0817		0.14914	...	$9.78^{+0.28}_{-0.26}$	$+1.58^{+0.28}_{-0.24}$	8.18 ± 0.19	0.878

Note. CLASSY sample properties derived from UV+optical photometry and spectra. Columns 1 and 2 indicate the target name used in this work and alternative names, respectively. Columns 3 and 4 give the target redshift from the literature and FUV–UV emission lines, respectively. Columns 5 and 6 list the total stellar masses and SFRs derived from *Beagle* SED fitting in Paper I. Column 7 gives the oxygen abundances derived in Paper I. Column 8 lists the galaxy half-light radius (r_{50}), estimated from Pan-STARRS imaging, from Paper I.

the J1112+5503 galaxy were impacted by guide-star failures, and thus we excluded this galaxy from the sample.

We performed the stellar-continuum subtraction with the method described in Section 3.1.1 from the HR spectra, binned by 15 native COS pixels. We also fit the MR co-added spectra,

after binning them by 6 native COS pixels, in order to fit all the main emission lines not covered by the HR co-adds. Finally, we doubly rebinned both configurations (i.e., binning the HR and MR coadds by 30 and 12 native COS pixels, respectively), to improve the fit of the faintest emission lines when possible.

2.2. Optical Data

High-quality optical spectra have been collected for the entire CLASSY sample to ensure uniform determinations of galaxy properties and to allow comparisons between properties derived from optical and UV diagnostics, thus enabling an accurately calibrated suite of UV diagnostics.

Data release (DR) 7 Apache Point Observatory (APO) SDSS spectra with a $3''$ aperture exist for 38 of the CLASSY galaxies (Abazajian et al. 2009), while for one galaxy, J1444+4237, there are DR13 BOSS spectrograph data with a $2''$ aperture (Albareti et al. 2017; Guseva et al. 2017). These spectra are in the wavelength range of 3800–9200 Å (3600–10,400 Å for BOSS), with a spectral resolution of $R \sim 1500 - 2500$ (Eisenstein et al. 2011).

For the remaining galaxies of the sample (J0036-3333, J0127-0619, J0337-0502, J0405-3648, J0934+5514, and J0144+0453), we used integral-field spectroscopy data, when available, or long-slit spectroscopy, instead of SDSS. Specifically, we used the VLT Visible Multi Object Spectrograph (VIMOS) integral-field unit (IFU) from James et al. (2009) for J0127-0619, MMT Blue Channel Spectrograph spectra from Senchyna et al. (2019) for J0144+0453, Keck Cosmic Web Imager (KCWI) IFU spectra from Rickards Vaught et al. (2021) for J0934+5514, and VLT/MUSE IFU spectra for the remaining three galaxies. MUSE spectra are also available for galaxies J0021+0052 (PI: Göran Östlin), J1044+0353, and J1418+2102 (PI: Dawn Erb). We used these data to retrieve emission-line ratios involving faint auroral lines, if undetected ($S/N < 3$) in SDSS spectra. Finally, for galaxies J0808+3948, J0944-0038, J1148+2546, J1323-0132, and J1545+0808, Multi-Object Double Spectrographs (MODS) data from the Large Binocular Telescope (LBT), presented in Arellano-Córdova et al. 2022, are also available (Paper V hereafter). Information on each of the optical data sets is provided in the following paragraphs.

Concerning the IFU data available for J0021+0052, J0036-3333, J0127-0619, J0337-0502, J0405-3648, J0934+5514, J1044+0353, and J1418+2102, we extracted a spectrum from a $2''.5$ aperture centered at the same coordinates of COS observations to match the COS aperture (see also Paper I and Paper V). Specifically, the integrated VIMOS spectrum of J0127-0619 is obtained combining the high-resolution blue and orange grisms, covering the wavelength range 4150–7400 Å with a spectral resolution of $R \sim 1150 - 2150$ (see James et al. 2009 for more details). The KCWI spectrum of J0934+5514 is in the wavelength range 3500–5600 Å at a median spectral resolution of $R \sim 3600$. Finally, the MUSE spectra are in the wavelength range 4300–9300 Å at a spectral resolution of $R \sim 2000 - 3500$.

Regarding the long-slit data, the MMT spectrum of J0144+0453 was taken with the 300 lines mm^{-1} grating with a $10'' \times 1''$ slit, oriented along the parallactic angle to minimize slit losses (see Senchyna et al. 2019 for more details). The wavelength coverage is 3200–8000 Å with a resolution of $R \sim 740$. For galaxies J0808+3948, J0944-0038, J1148+2546, J1323-0132, and J1545+0808, instead of the SDSS, we took advantage of the MODS data from LBT obtained using the G400L and G670L. The MODS long-slit data were taken with a $60'' \times 1''$ slit, with an extraction aperture of $2''.5 \times 1''$, and a slit orientation along the parallactic angle (see Paper V for more details). The wavelength coverage extends from 3200 to 10,000 Å with a moderate spectral resolution of $R \sim 2000$.

Paper V compares the SDSS, LBT, and MUSE integrated spectra for the galaxies with multiple observations, demonstrating that flux calibration issues or aperture differences do not introduce significant discrepancies in the optical ISM properties in terms of gas attenuation, density, temperature, metallicity, and SFRs. This result supports our comparison of the physical properties obtained using these different sets of optical data. The UV and optical fluxes, highlighting which telescope and instrument was considered for each galaxy, as well as the products of the analysis of this paper will be provided on the CLASSY MAST webpage as downloadable tables. In Appendices B, C, and D, we show which information will be provided.

3. Data Analysis

The UV and optical spectra were analyzed making use of a set of customized python scripts in order to first fit and subtract the stellar continuum and then fit the main emission lines with multiple Gaussian components where needed. This allowed us to estimate the stellar population properties (i.e., age, metallicity, and stellar dust attenuation), emission-line properties (fluxes, velocities, velocity dispersions, and equivalent widths), the UV–optical flux offset (discussed in Appendix A), and the ISM gas properties. In the following, all the steps are explained in detail.

3.1. Stellar Continuum

3.1.1. UV Spectra

The analysis of UV spectra relies on a robust stellar-continuum fitting procedure both for determining the properties of the stellar population and for accurately measuring nebular UV emission lines, such as He II $\lambda 1640$ or C IV $\lambda \lambda 1548, 51$. For the purposes of subtracting the UV stellar continuum in the HR spectra¹⁹ for this paper, we compare the results of two sets of fits, which will be described in detail in P. Senchyna et al. (2022, in preparation; S22 hereafter). Both fits considered here are based on a flexible linear combination of spectra of simple stellar populations (SSPs) spanning a wide range of metallicities and ages, as described by Chisholm et al. (2019), and assume a Reddy et al. (2016) attenuation law. The primary difference between the two sets of results is the stellar population synthesis framework used to generate the basis of SSP spectra. The first uses the STARBURST99 theoretical UV predictions described by Leitherer et al. (1999, 2010), while the second relies on the latest version of the Bruzual & Charlot (2003) models (S. Charlot & G. Bruzual, in preparation, hereafter C&B; see also Gutkin et al. 2016; Vidal-García et al. 2017; Plat et al. 2019). These population synthesis models adopt different prescriptions for the evolution and atmospheres of massive stars, resulting in particularly significant differences for lines such as He II $\lambda 1640$ that can be powered in the dense optically thick winds of very luminous stars (e.g., Senchyna et al. 2021).

In addition to stellar light and dust attenuation, the other crucial constituent of the UV light of star-forming galaxies is the nebular continuum. Both sets of models include the contribution of the nebular continuum computed in a self-

¹⁹ It is not necessary to fit the stellar continuum in the MR spectra, as the NUV range does not contribute significantly to the stellar population analysis, and in that range there are no significant absorption or resonant emission lines due to stars.

consistent manner and assuming a closed geometry, as described in Leitherer et al. (1999), and Gutkin et al. (2016) and Plat et al. (2019), respectively. The STARBURST99 predictions do not include variable parameters describing this emission, but the Cloudy-computed nebular continuum for the C&B models are presented at varying $\log(U)$, which can have an impact in the UV (see, e.g., Senchyna et al. 2022). Our fiducial assumed volume-averaged $\log(U) = -2.5$ (defined as in Gutkin et al. 2016) represents the median value inferred for the full CLASSY sample from fitting the UV continuum with different $\log(U)$ in the range $[-3; -1]$, and it is also typical of the values inferred from fitting the nebular line emission of similar local star-forming galaxies (Plat et al. 2019; Senchyna et al. 2022). However, we stress that the choice of fixing this parameter has a minimal impact on the fidelity of the UV continuum fits, with a negligible median difference in the reduced chi-square (i.e., $\lesssim 0.01$; S22). Moreover, Chisholm et al. (2019) explored variations with the $\log(U)$ and density, finding no changes in the shape of the nebular continuum and in the relative contribution of the nebular/stellar-continuum ratio over the expected $\log(U)$ range (see also Byler et al. 2017).

In most other respects, the fits proceed in a similar manner. The observed HR spectra are fitted after first rebinning by 15 pixels and after smoothing the models with a Gaussian kernel to best represent the achieved resolution and S/N. In both cases, we adopt the maximum initial mass function (IMF) upper mass cutoff provided for the models (using Kroupa 2001 and Chabrier (2003), for STARBURST99 and C&B, respectively); this is $100 M_{\odot}$ for STARBURST99 and $600 M_{\odot}$ for C&B (see, e.g., Plat et al. 2019; Senchyna et al. 2022). The uncertainties in the fits were calculated via a Monte Carlo technique, modulating the observed flux with a Gaussian kernel centered on zero with a width equal to the formal estimated error on the flux. To summarize, the two stellar-continuum fits provide independent estimates of the intrinsic stellar $E(B - V)_{\text{UV}}$ reddening, and the light-weighted ages and metallicities of the ionizing stellar populations, alongside full fits to the UV continuum.

For the purpose of this work, the stellar-continuum fitting is used to subtract the stellar contribution from the observed UV spectra, thus allowing us to accurately measure the nebular emission lines in the range 1150–2000 Å. After carefully checking that the subtraction of either STARBURST99 or the C&B stellar-continuum best fit gave similar results for our emission-line fitting, we ultimately decided to use the C&B best fit, as it takes the stellar He II $\lambda 1640$ contribution into account. Moreover, the C&B models can be extended to wavelengths of ~ 9000 Å in the optical, which allowed us to perform accurate flux scaling between the optical and UV spectra.

The full flux-scaling analysis is described in Appendix A, where we explain our method to properly scale the flux of the optical spectra to the UV. In summary, a flux offset between COS and the optical spectra is expected as they have been obtained via different instruments with slightly different apertures and pointing position. The median value that we find for this UV–optical flux offset is 0.78 ± 0.03 , and we report the value obtained for each galaxy on the CLASSY MAST webpage, as shown in Appendix C. We multiplied the observed optical spectra of each CLASSY galaxy by its corresponding UV–optical flux offset to correct them. We highlight that this

flux correction has no impact on the properties derived from the flux ratios within each galaxy, but only when ratios between UV and optical emission lines (e.g., $\text{O III} \lambda 1666 / [\text{O III}] \lambda 5007$) are considered.

3.1.2. Optical Spectra

As the UV stellar-continuum models were optimized for the young stellar population, it was not feasible to use the UV models to perform a self-consistent fit of the optical wavelength portion of the spectrum, due to the dominant contribution from the older population of stars in this wavelength regime (e.g., Leitherer et al. 1999). Thus, in order to remove any stellar absorption components present in the Balmer emission lines, we model the optical stellar continuum using *Starlight*²⁰ spectral synthesis code of Fernandes et al. (2005a) and the stellar models of Bruzual & Charlot (2003) with the IMF of Chabrier (2003). The set of the stellar models taken into account comprises 25 ages (1 Myr–18 Gyr) and six metallicities ($0.05 < Z_{\star}/Z_{\odot} < 2.5$). It should be noted that, while the *Starlight* models do not include a nebular continuum component, the nebular continuum contribution in this wavelength regime is known to be negligible ($< 10\%$; Byler et al. 2017).

As a preliminary step, we corrected the spectra for the Galactic foreground reddening correction (see Section 2.1) and uniformly sampled the rest-frame wavelength, the flux, and the error in steps of $\Delta\lambda = 1$ Å. For reddening the models, we used the attenuation law of Cardelli et al. (1989). The *Starlight* models are fitted over the wavelength range 3700–9100 Å. In Figure 17, included in Appendix A, we show our UV and optical stellar-continuum best fit for galaxies J0021+0052 and J1144+4012 as an example.

3.2. Emission Lines

The analysis of the emission lines in the UV and optical spectra (after the subtraction of the best-fit stellar continuum, described in Section 3.1) was performed separately but with a similar approach. We simultaneously fit each spectrum accounting for a set of UV and optical emission lines in the wavelength range 1265–2000 Å and 3700–9100 Å, respectively, with a linear baseline centered on zero and a single Gaussian, making use of the code MPFIT (Markwardt 2009), which performs a robust nonlinear least-squares curve fitting. We list the final fluxes, corrected for dust reddening, of all fitted UV and optical emission lines in the CLASSY MAST webpage, as shown in Appendices B and C.

In our procedure the main Milky Way absorption lines were masked, and the fitting was performed only in windows of 3000 km s^{-1} centered around each emission line. We tied together the velocity (i.e., the line center) and in optical spectra also the velocity dispersion (or line width) for all the emission lines, to better constrain weak or blended features, while allowing the line flux to vary freely (in general). An exception was made for the line center of the UV emission lines C III] and C IV, because they can be significantly shifted in velocity with respect to the others due to their origin, as we will discuss in a forthcoming paper focused on the kinematics and ionization source of the gas in the CLASSY galaxies (M. Mingozzi et al. 2022, in preparation; M22 hereafter).

²⁰ www.starlight.ufsc.br

In order to robustly determine uncertainties, we followed the Monte Carlo method where we perturbed N times (with $N = 100$) the observed spectra by adding to each spectral element a random value drawn from a Gaussian distribution centered on zero with a standard deviation equal to the observed spectrum uncertainty. We then fitted each configuration with MPFIT (Markwardt 2009), obtaining 100 estimates of the free parameters of the fit, which are the flux, velocity, and velocity dispersion. Finally, we calculated the 50th (i.e., the median) and the (50th–16th) and (84th–50th) percentiles of the distributions of the fitted perturbed spectra and of the free parameters of the fit. The median of each free parameter is considered as the best-fit value, with a lower and upper uncertainty given by the sum in quadrature of the (50th–16th) and (84th–50th) percentiles, divided by the square root of N , and the MPFIT error. The S/N associated to each line is then defined as the ratio between the flux and the flux uncertainty. All emission lines with S/N higher than 3 are considered to be reliable detections.

3.2.1. Special Constraints

In our fitting procedure the line flux of each emission line must be nonnegative but it is left free to vary, apart from the doublets [N II] $\lambda\lambda 6548, 6584$ and [O I] $\lambda\lambda 6300, 64$, where we consider the transition probability of the doublets and assumed a fixed line ratio of 0.333 between the fainter and the brighter line (Osterbrock 1989). We did not fix the [O III] $\lambda\lambda 4959, 5007$ fluxes because in the KCWI data of J0934+5514 and SDSS data of J1253-0312 the [O III] $\lambda 5007$ line is saturated. For these objects we obtained an estimate of the [O III] $\lambda 5007$ by applying the fixed line ratio of 3 with respect to [O III] $\lambda 4959$ (Osterbrock 1989). We notice that for J1253-0312 the H α line is also clipped, so we discarded its flux.

Concerning C III] $\lambda\lambda 1907, 9$, we constrained the line ratios [C III] $\lambda 1907$ /C III] $\lambda 1909$ to vary up to 1.6 (Osterbrock 1989), to avoid nonphysical values. Our procedure allows us to fit this doublet with two well-separated Gaussians, as the distance between the centroids of the two emission lines of the doublet is fixed. Conversely, the resolution of the COS/G185M ($R \sim 20000@2100 \text{ \AA}$) does allow us to resolve the C III] doublet even after the 6–12 native pixel binning (i.e., $\sim 40\text{--}80 \text{ km s}^{-1}$), as long as the width of the fitted emission lines is smaller than half of their wavelength separation (i.e., $\sim 300 \text{ km s}^{-1}$). Among the galaxies with significant C III] emission (S/N > 3), the latter condition is not satisfied in J1044+0353 and J1418+2102 because of the lower resolution of COS/G140L. Concerning the [O II] $\lambda\lambda 3727, 29$ doublet, blended in the SDSS, MOD, and MMT data, the distribution of flux between these two Gaussians is not reliable enough to derive an accurate line ratio. Therefore, the [O II] ratio is derived only for the KCWI data of J0934+5514 (the doublet is not covered by the wavelength range of MUSE).

Another aspect we took into account in our fitting procedure is that optical lines such as [O III] $\lambda 4363$ and [Ar IV] $\lambda 4714$ can suffer from contamination due to the Fe II $\lambda 4360$ and He I $\lambda 4714$, respectively (see, e.g., Curti et al. 2017; Arellano-Cordova et al. 2020). For instance, Arellano-Cordova et al. (2020) demonstrated that the use of a contaminated [O III] $\lambda 4363$ could lead to differences in metallicity of up to 0.08 dex. In order to mitigate this problem, we fitted these faint features simultaneously with the other emission lines, tying them to the brighter He I $\lambda 4471$ and Fe II $\lambda 4288$, assuming a

ratio of 0.728 and 0.125 (valid at $n_e = 100 \text{ cm}^{-3}$ and $T_e = 10^4 \text{ K}$, from PyNeb), respectively.²¹

3.2.2. Multicomponent Fitting

After careful inspection of the optical spectra, we noticed that the H α profile (in particular) shows a broad component in many CLASSY galaxies. We therefore performed two-component Gaussian fits to the main optical emission lines (i.e., H δ , H γ , H β , [O III] $\lambda\lambda 4959, 5007$, [O I] $\lambda\lambda 6300, 74$, [N II] $\lambda\lambda 6548, 84$, H α , [S II] $\lambda\lambda 6717, 31$). Specifically, we considered one narrow component, with an observed velocity dispersion $\sigma < 200 \text{ km s}^{-1}$, that is a representative cutoff for the galaxies of our sample, and a broad component ($\sigma < 1000 \text{ km s}^{-1}$). Their velocity and velocity dispersion are tied to be the same for all the emission lines. To understand if the addition of a second component is significant, we calculated the reduced chi-square $\tilde{\chi}^2$ of the single- and double-component fits in the rest-frame wavelength range 6540–6590 \AA covering H α (4950–5010 \AA for J1253-0312 and J0934+5514, for which H α is unavailable), and chose the model with more components only if the $\tilde{\chi}^2$ was at least 0.1 dex smaller. This condition is satisfied in 24 out of 44 galaxies of our sample.

In our UV spectra, the S/N is usually not high enough to detect faint broad components in the emission lines of interest here. However, after a visual inspection we did notice a clear broad profile in the emission lines of J1044+0353 and J1418+2102 (see also Berg et al. 2021), J1016+3754, J0337-0502, J1323-0132, and J1545+0858. For these objects we fitted the He II $\lambda 1640$ and [O III] $\lambda\lambda 1661, 6$ with two components. We tested a two-Gaussian component fitting also on the C III] doublet, without finding a significant improvement in our results. This is due to the very small wavelength separation of the C III] doublet lines, which results in degenerate line centroids that make it difficult to use multiple components. Interestingly, for J0337-0502, J1044+0353, J1418+2102, and J1323-0132 (see Figure 2) we also observed a doubled-peak profile in the C IV doublet. As discussed in Berg et al. (2021), such profiles are the result of resonant scattering, whereas broadening can be due to radiation transport/scattering. Due to the different line processes responsible for C IV emission, it should be noted that the properties of the multicomponent fits to this line were not constrained with the same kinematics as the nebular emission lines.

For the purpose of this work, we chose to only consider the narrow (and dominant) component of our emission lines, which on average constitutes >70% of the total flux. This allows us to maintain the highest accuracy in the emission-line diagnostics derived here, as each emission-line component originates in gas with different physical conditions (ionization degree, temperature, density, velocity, etc.; see, e.g., James et al. 2009). Indeed, broad emission indicates large velocities that can be driven by different mechanisms such as stellar winds, galactic outflows, or turbulence, and are possibly linked to different ionization sources, such as photoionization and/or shocks (e.g., Izotov & Thuan 2007; James et al. 2009; Amorín et al. 2012; Bosch et al. 2019; Hogarth et al. 2020; Komarova et al. 2021).

It should be noted that we were unable to fit a broad component emission in the UV nebular lines of all the galaxies that displayed broad component emission in the optical due to

²¹ We fitted the Fe II $\lambda 4288$ only for galaxies in which this line is visible, that is, at $12 + \log(\text{O}/\text{H}) \gtrsim 7.7$.

S/N limitations and the faintness of UV emission lines. For these cases, we are confident that the possible contribution from broad component emission to the single (narrow) component fit is negligible and within the uncertainties on the emission lines. We will investigate possible differences of the conditions of the broad component in our next paper focused on the kinematics and ionization mechanisms (M22).

3.2.3. UV Emission-line Detections

While there is a plethora of strong optical emission lines that are uniformly detected throughout the sample, UV emission lines can be mostly faint and sometimes not detected at all. It is therefore important for us to highlight in how many galaxies the UV emission lines are clearly detected. As explained in Section 2.1, we fitted the HR and MR/LR co-added spectra, after performing different levels of binning. We consider UV emission lines with $S/N > 3$ to be detections. We considered the results from the doubly rebinned spectra (of 30 and 12 pixels for the HR and MR/LR co-adds, respectively) only for the emission lines with $S/N < 3$. If the S/N is still lower than the chosen threshold, then we consider the flux as an upper limit, while if the line is not observed at all, as a nondetection. As an example, in Figure 1 we show the UV emission lines fitted by our fitting routine for galaxy J0337-0502 (i.e., SBS0335-052 E). The spectrum and the fit are reported in black and red, while the spectrum and fit uncertainties are shown in shaded gray and red, respectively. The id and S/N of each zoomed line are indicated on top of each panel, whose margins are colored according to the binning applied to the spectrum before the fitting (HR rebinned of 15 in blue, HR rebinned of 30 in cyan, MR rebinned of 6 in dark green, MR rebinned of 12 in light green). In Figure 2 instead we show the fitted CLASSY COS spectra of the C IV $\lambda\lambda 1548,51$ and C III] $\lambda\lambda 1907,9$ emission lines for all the galaxies in which the lines are detected with $S/N > 3$. In Appendix B, in Figures 19–23 we show analogous figures for the N IV] $\lambda\lambda 1483,87$, He II $\lambda 1640$, [O III] $\lambda\lambda 1661,6$, [N III] $\lambda\lambda 1747,54$, and Si III] $\lambda\lambda 1893,92$ emission lines, respectively, with $S/N > 3$. In the following we describe the detection of each of these lines within the CLASSY sample.

C IV $\lambda\lambda 1548,51$ is observed in pure emission with $S/N > 3$ in only 9 CLASSY galaxies (see Figure 2), while in the other galaxies it shows a P-Cygni profile or is only in absorption. Generally, the C IV doublet is dominated by a broad P-Cygni profile due to winds of luminous O stars (e.g., Shapley et al. 2003; Steidel et al. 2016; Rigby et al. 2018; Llerena et al. 2022). Only high-resolution spectra such as those of the CLASSY survey can allow to successfully separate the stellar and the nebular components of C IV emission (see also Crowther 2007; Quider et al. 2009). Pure nebular emission in C IV $\lambda\lambda 1548,51$ has been recently detected in $z > 6$ targets (Stark et al. 2015; Mainali et al. 2017; Schmidt et al. 2017) and, rarely, in local galaxies (Berg et al. 2016; Senchyna et al. 2017, 2019; Berg et al. 2019b; Wofford et al. 2021; Senchyna et al. 2022). For this paper, we only take the 9 CLASSY galaxies with C IV in pure emission into account, without considering the galaxies that show a P-Cygni or pure absorption line profile. All these galaxies also show C III] $\lambda\lambda 1907,9$, He II $\lambda 1640$, and [O III] $\lambda 1666$, apart from J0934+5514 (i.e., Izw 18), where the [O III] $\lambda 1666$ is undetected because of Milky Way (MW) line contamination.

C III] $\lambda\lambda 1907,9$, often the strongest UV nebular emission line, is observed with $S/N > 3$ in 28 CLASSY galaxies (see

Figure 2). Among these, we can see this doublet deblended in 26 objects (excluding J1044+0353 and J1418+2102; see Section 3.2.1). This doublet is a density diagnostic, as we will discuss in Sections 5.2 and 6.2.

N IV] $\lambda\lambda 1483,87$ is observed with $S/N > 3$ in only six CLASSY galaxies (both doublet lines are observed only in J1044+0353, J1253-0312 and J1545+0858). This doublet has rarely been seen in emission in star-forming galaxies (Fosbury et al. 2003; Raiter et al. 2010; Vanzella et al. 2010; Stark et al. 2014). These lines are probably due to young stellar populations, and, if the source is not hosting an active galactic nucleus (AGN), they could be a signature of massive and hot stars with an associated nebular emission (Vanzella et al. 2010). This doublet is also a density diagnostic (Keenan et al. 1995), and it traces higher-ionization regions with respect to the C III] and Si III] doublets (see Sections 5.2 and 6.2).

He II $\lambda 1640$ is detected with $S/N > 3$ in 19 CLASSY galaxies and generally shows a narrow profile (median velocity dispersion of $\sigma \sim 55 \text{ km s}^{-1}$), indicating its nebular nature. However, in the spectra of J0942+3547, J1129+2034, J1200+1343, J1253-0312, and J1314+3452 the line profile looks broader (with σ up to 200 km s^{-1}), which suggests the presence of a stellar component residual despite the removal of the C&B best-fit stellar continuum (see, e.g., Nanayakkara et al. 2019; Senchyna et al. 2021).

O III] $\lambda\lambda 1661,6$, one of the strongest UV emission lines, has $S/N > 3$ in 22 CLASSY galaxies. In J0127-0619 and J1225+6109, where one of the two lines of the O III] doublet is contaminated by a MW absorption line, we estimated the flux from the other line, using a line ratio measured from PyNeb of 0.4 (valid at $n_e = 100 \text{ cm}^{-3}$ and $T_e = 10^4 \text{ K}$). These are auroral lines, similar to the optical [O III] $\lambda 4363$, and thus can be used as a temperature diagnostics in comparison with the optical nebular [O III] $\lambda\lambda 4959,5007$, as we will discuss in Section 5.3 and Section 6.3.

[N III] $\lambda\lambda 174754$ is a multiplet (i.e., a blend of emission at 1746.8, 1748.6, 1749.7, 1750.4, and 1752.2 Å; Keenan et al. 1994). These lines are suggested to have a nebular origin and may be used in the so-called UV Baldwin–Phillips–Terlevich diagrams (Feltre et al. 2016) to discriminate between SF and AGN activity. However, the multiplet is usually revealed in spectra of WN-type stars (e.g., Crowther & Smith 1997). Interestingly, only one galaxy of the CLASSY sample, J0127-0619 (i.e., Mrk 996), shows this multiplet in clear emission with $S/N \sim 9$. WR features (mainly late-type WN stars) in this galaxy were discovered for the first time by Thuan et al. (1996), while their distribution as well as the ISM abundances and kinematics were investigated by James et al. (2009). This could indicate a non-ISM origin of this emission (see also M22). A hint of emission with $S/N \sim 3$ is observed also in J1253-0312.

Si III] $\lambda\lambda 1893,92$ is observed with $S/N > 3$ in six CLASSY galaxies. These lines are generally very faint, but also in many targets one of the two or both fall out of the COS observed wavelength range (both doublet lines are observed only in J1044+0353, J1253-0312, and J1448-0110). Similarly to C III], this doublet is a density diagnostic.

Along with these UV emission lines we also fitted the other lines shown in Figure 1, namely: Si II] $\lambda 1265$, Si IV] $\lambda 1394$, O IV] $\lambda 1401$, Si IV] $\lambda 1403$, O IV] Si IV, S IV] $\lambda 1406$, O IV] $\lambda 1407$, S IV] $\lambda 1410$ M S IV] $\lambda 1417$, S IV] $\lambda 1424$, and Si II* $\lambda 1534$. Many of these lines can be visible in emission in galaxies that also show C IV in pure emission, as shown in Figure 1. Due to their lack

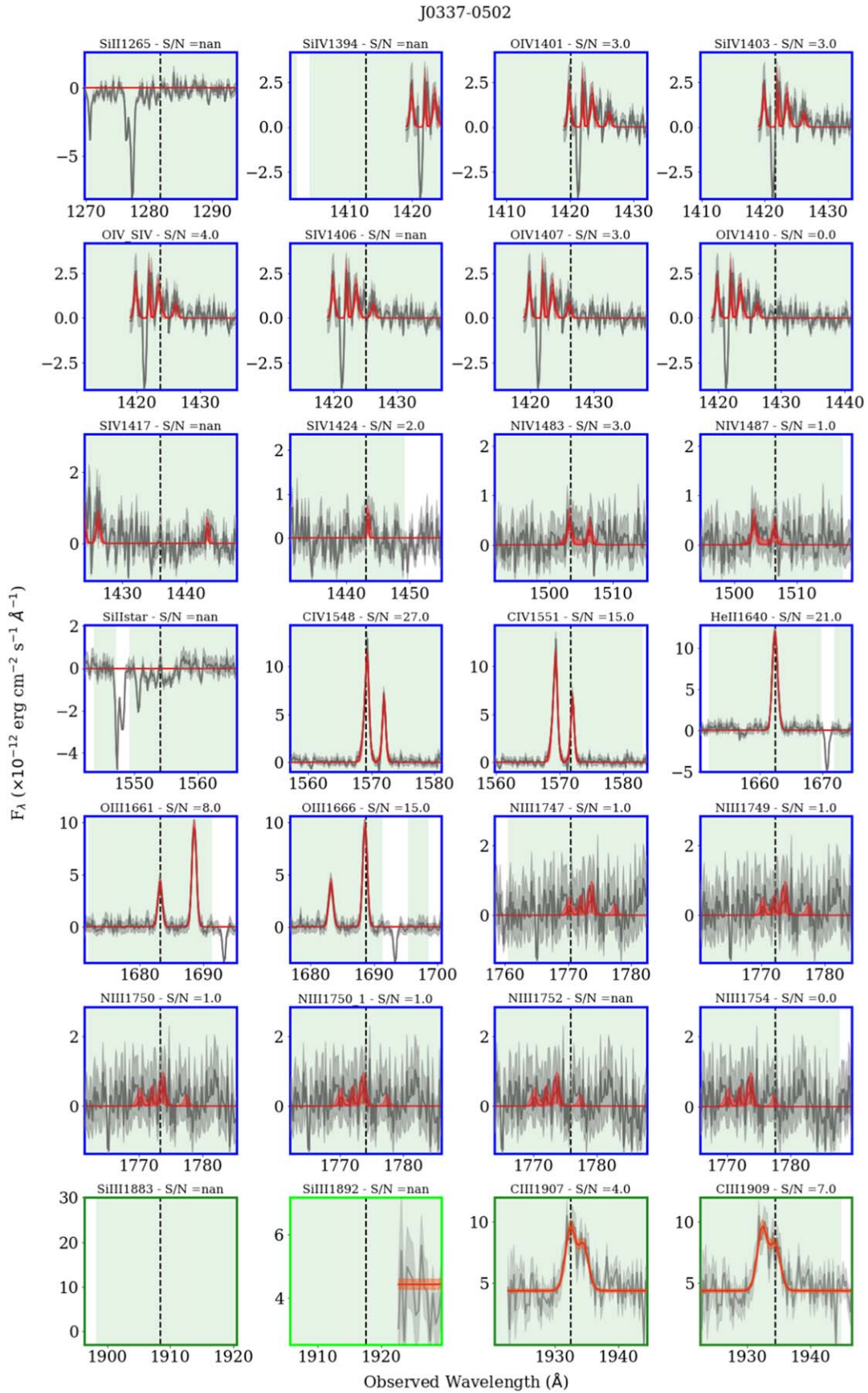


Figure 1. UV emission lines fitted by our fitting routine for galaxy J0337-0502 (i.e., SBS0335-052 E): the spectrum and the fit are reported in black and red, while the spectrum and fit uncertainties are shown in shaded gray and red, respectively. The id and S/N of each zoomed line is indicated on top of each panel, whose margins are colored according to the binning applied to the spectrum before the fitting (HR rebinned of 15 in blue, MR rebinned of 6 in dark green, MR rebinned of 12 in light green). The dashed black vertical lines indicate the observed wavelength of each line according to the redshift of the galaxy z_{fit} , reported in Table 1.

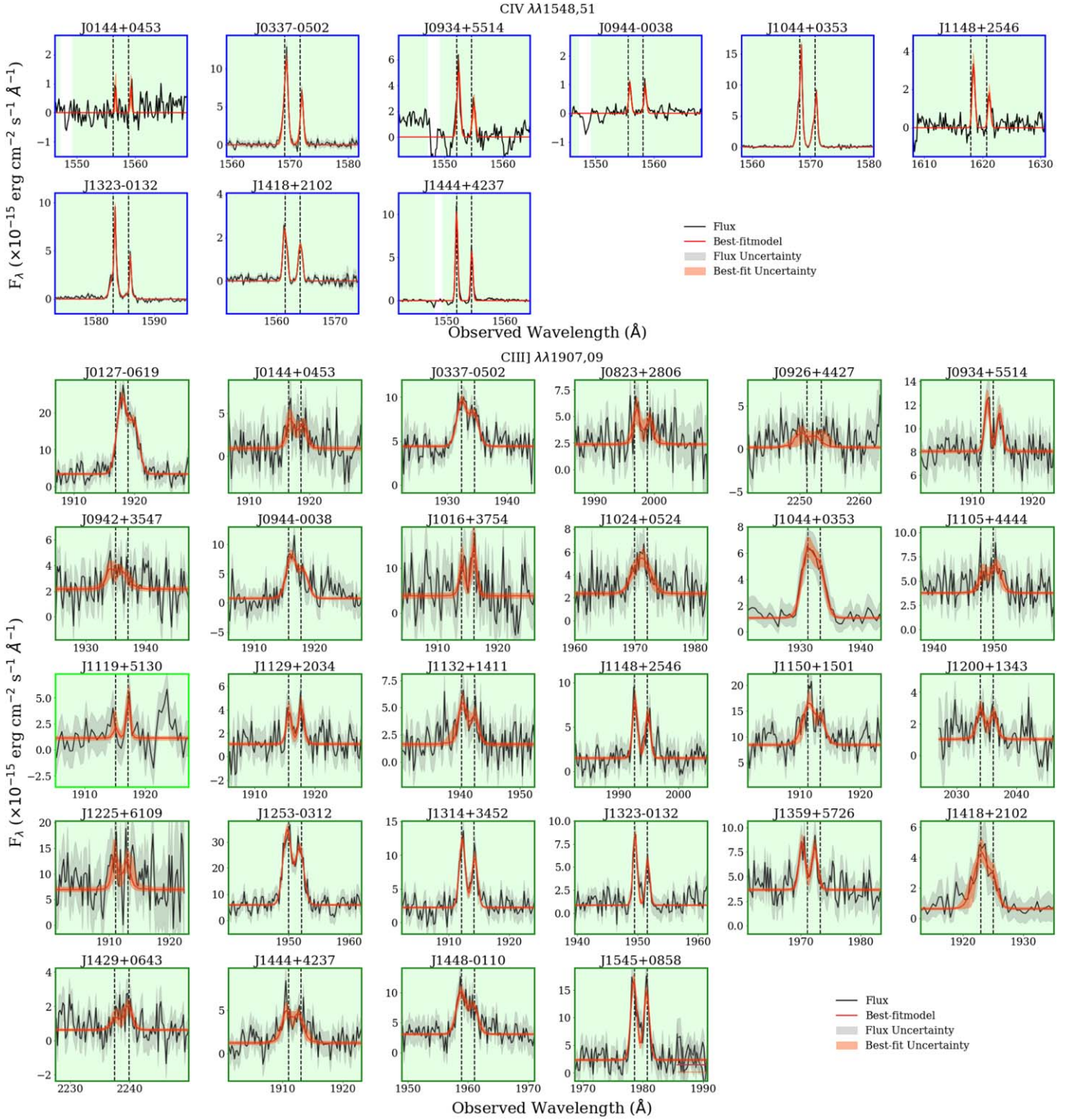


Figure 2. Fit of the C IV $\lambda\lambda 1548,51$ and C III] $\lambda\lambda 1907,9$ emission-line doublet with $S/N > 3$, visible in 9 and 28 galaxies, respectively. The observed flux and the best-fit model are shown in black and red, respectively, while their uncertainties are given by the gray and red shades. The black dashed vertical lines indicate the line positions, taking z_{fit} into account. The margins are colored according to the binning applied to the spectrum before the fitting (HR rebinned of 15 in blue, MR rebinned of 6 in dark green, MR rebinned of 12 in light green).

of detection throughout the sample with large enough S/N , we do not consider these lines any further.

4. Deriving the Physical Properties of the ISM

H II regions are stratified, with higher-ionization species, such as [Ar IV] or [O III], closer to the ionization source and

lower-ionization species, such as [S II] or [O II], in the outer parts. Typically H II regions are modeled by three zones of different ionization: the low-, intermediate-, and high-ionization zones. As pointed out in Berg et al. (2021, 2022), high- z systems and their local analogs are characterized by the presence of high-energy UV and optical emission lines due to their low metallicity and thus extreme radiation fields, revealing the

presence of an additional “very-high-ionization” zone. It is important to stress that radiation fields and metallicity are tightly linked such that stellar populations of lower metallicity have harder radiation fields. This led Berg et al. (2021) to extend the classical three-zone model to a four-zone model, adding the He^{+2} species necessary to produce the observed He II emission via recombination (ionization potential $E > 54.42$ eV).

Overall, an accurate determination of H II region properties requires reliable tracers for each zone. This is because different ions are tracing different conditions of nebulae in terms of density, temperature, and ionization, as they are not co-spatial (e.g., Nicholls et al. 2020). The COS aperture on CLASSY targets is covering multiple H II regions or even the entire galaxy for the most compact objects. Hence, we can employ the use of multiple diagnostics both in the optical and in the UV to trace the conditions in the different ionization regions and compare their properties, investigating the ISM structure of our targets with the utmost detail. Here we stress that a great advantage of the CLASSY survey is the simultaneous coverage of many optical and UV diagnostic lines. In particular, UV emission lines are coming from higher-ionization zones, which gives us access to a wider range of ionization zone tracers than typically available from the optical alone.

Then, we employed iteratively the PyNeb task *getCrossTemDen*, which combines a density and a temperature diagnostic, and ultimately converges to a final value of n_e and T_e . First, we calculated the intrinsic Balmer line ratios using PyNeb, assuming a Case-B Hydrogen recombination with a starting temperature of $T_e = 1 \times 10^4$ K and $n_e = 10^2 \text{ cm}^{-3}$, considered appropriate for typical star-forming regions (Osterbrock 1989; Osterbrock & Ferland 2006). Then, we iteratively calculated the density and temperature, using the reddening value to correct the line ratio used as a temperature tracer, and updating at each cycle the $\text{H}\alpha$ and $\text{H}\beta$ emissivities (and thus $E(B - V)$), n_e and T_e , only if the new value obtained was finite. Our iterative approach stops when the difference in temperature between two cycles becomes lower than 20 K. To estimate the fiducial values and errors on n_e and T_e , we run the *getCrossTemDen* task 500 times for each different combination of n_e and T_e diagnostics, taking the median of values and the standard deviation for the uncertainties. Once the densities and temperatures are known in each zone of the nebula, it is then possible to calculate the corresponding ionic abundances, with a similar iterative procedure using the *getIonAbundance* PyNeb task, and the same method to estimate the uncertainties.

Tables 2 and 3 show the optical and UV diagnostics investigated for the different ionization zones in this work. Unfortunately in this work we lack the $[\text{Ne III}] \lambda 3342 / \lambda 3868$ ratio that Berg et al. (2021) used to estimate the temperature of the very-high-ionization zone. We note, however, that this ratio provided results consistent to the values obtained for the high-ionization zone (Berg et al. 2021). Our set of UV lines is characteristic of the intermediate- and high-ionization zones. The comparison between the different properties calculated with optical and UV diagnostics are shown and discussed in Sections 5 and 6. In the following sections we provide the details about each calculated quantity.

4.1. Dust Attenuation

Before comparing the ratios of the emission lines separated in wavelength throughout the UV–optical wavelength regime,

the emission lines were corrected for the intrinsic galaxy dust attenuation in terms of $E(B - V)$. $E(B - V)$ was determined comparing the observed relative intensities of the strongest Balmer lines available in our optical spectra (i.e., $\text{H}\alpha/\text{H}\beta$, $\text{H}\beta/\text{H}\gamma$, $\text{H}\beta/\text{H}\delta$) with their intrinsic values. These intrinsic values depend on the density and temperature of the gas, which we estimate with the corresponding diagnostics for each ionization zone, as explained in Sections 4.2 and 4.3. The final reddening estimate is an error-weighted average of the $\text{H}\alpha/\text{H}\beta$, $\text{H}\gamma/\text{H}\beta$, and $\text{H}\delta/\text{H}\beta$ reddening values.

To correct the optical emission lines, we applied the Cardelli et al. (1989) reddening law with $R_v = 3.1$, which is appropriate for the CLASSY emission-line fluxes (Berg et al. 2022). Indeed, Wild et al. (2011b) found that the nebular attenuation curve has a slope similar to the MW attenuation curve, rather than that of the SMC (Gordon & Clayton 1998; Gordon et al. 2003) or the one from Calzetti et al. (2000). The UV emission lines, instead, were corrected assuming a Reddy et al. (2016) attenuation curve with $R_v = 2.191$, which represents the first spectroscopic measurement of the shape of the far-UV dust attenuation curve for galaxies at high redshift ($z \sim 3$), i.e., systems that are analogous to our CLASSY sample.

Dust attenuation can be also estimated from comparing the observed slope of the UV spectra in the range 1400–1800 Å (the “ β slope;” see, e.g., Leitherer et al. 1999; Calzetti et al. 1994) with the intrinsic slope of the models used in the best fit of the stellar populations (Calzetti et al. 2000; Reddy et al. 2016). This quantity ($E(B - V)_{\text{UV}}$ hereafter) is given as an output of the UV stellar-continuum fitting described in Section 3.1.1. $E(B - V)_{\text{UV}}$ represents the stellar attenuation and its relation with the gas $E(B - V)$ derived from the Balmer decrement is not trivial, as it is discussed in Section 6.1.

4.2. Density

The electron density n_e can be derived from the intensity ratios of lines emitted by a single ion from two levels with nearly the same energy but different radiative-transition probabilities or different collisional de-excitation rates (Osterbrock 1989). As a guide to the reader, in Figure 3 we highlight the different combinations of diagnostics considered throughout this study and their characteristics, as introduced in Tables 2 and 3. Specifically, in the eight main panels of Figure 3, we report the measurements of each line ratio used as a tracer of n_e for the CLASSY galaxies and its corresponding density calculated with PyNeb. The dots are color coded according to the ion species and are the same used in the top two panels, where the ionization potential and the traced density range of each ion and line ratio, are reported. The different symbols indicate which line ratio we assumed to estimate the temperature (described in Figure 4 and Section 4.3), as reported in the legend. The black curves show the variation of each line ratio as a function of the temperature, considering $T_e = 5 \times 10^3$ K, 1×10^4 K and 2.5×10^4 K.

Overall, looking at Figure 3, for the low-ionization zone, the most typical density diagnostics are $[\text{S II}] \lambda 6717 / \lambda 6731$ and $[\text{O II}] \lambda 3729 / \lambda 3727$, sensitive in the range ~ 40 – 5000 cm^{-3} . Moving toward higher-ionization potentials, other density tracers are $[\text{Cl III}] \lambda 5518 / \lambda 5538$, sensitive in the range $\sim 10^2$ – $2 \times 10^4 \text{ cm}^{-3}$, or $[\text{Si III}] \lambda 1883 / \text{Si III} \lambda 1892$ and $[\text{C III}] \lambda 1907 / \text{C III} \lambda 1909$ in the UV, tracing values in the range $\sim 10^3$ – $2 \times 10^5 \text{ cm}^{-3}$. Moreover, Méndez-Delgado et al. (2021) proposed the use of $[\text{Fe III}] \lambda 4701 / \lambda 4659$, sensitive in the

Table 2
Optical ISM Diagnostics in the Different Ionization Zones According to the Literature and Available in This Work

Property	Ionization Zone			
	Low	Intermediate	High	Very High
$E(B - V)$	$H\alpha/H\beta, H\beta/H\gamma, H\beta/H\delta$	$H\alpha/H\beta, H\beta/H\gamma, H\beta/H\delta$	$H\alpha/H\beta, H\beta/H\gamma, H\beta/H\delta$	$H\alpha/H\beta, H\beta/H\gamma, H\beta/H\delta$
n_e	[S II] $\lambda 6717/\lambda 6731$ [O II] $\lambda 3729/\lambda 3727$	[Cl III] $\lambda 5518/\lambda 5538$ [Fe III] $\lambda 4701/\lambda 4659$	[Ar IV] $\lambda 4714/\lambda 4741$	[Ar IV] $\lambda 4714/\lambda 4741$
T_e	[N II] $\lambda 5755/\lambda 6584$ [S II] $\lambda \lambda 4069, 72/\lambda \lambda 6717, 31$ [O II] $\lambda \lambda 3727, 29/\lambda \lambda 7320, 30$	[S III] $\lambda 6312/\lambda 9069$	[O III] $\lambda 4363/\lambda 5007$	[O III] $\lambda 4363/\lambda 5007$
$\log U$	[S III] $\lambda \lambda 9069, 9532$ / [S II] $\lambda \lambda 6717, 31$	[O III] $\lambda 5007$ / [O II] $\lambda \lambda 3727, 9$	[Ar IV] $\lambda \lambda 4714, 41$ / [Ar III] $\lambda 7135$	

Note. ISM diagnostics available in the optical for each ionization zone in a four-zone model (see Berg et al. 2021). Specifically, we list diagnostic line ratios for the dust attenuation ($E(B - V)$), electron density (n_e), electron temperature (T_e), and ionization parameter ($\log(U)$).

Table 3
ISM UV Diagnostics in the Different Ionization Zones According to the Literature and Available in This Work

Property	Ionization Zone			
	Low	Intermediate	High	Very High
$E(B - V)$	β -slope	β -slope	β -slope	β -slope
n_e	...	C III] $\lambda 1907/\lambda 1909$ Si III] $\lambda 1883/\lambda 1892$	N IV] $\lambda 1483/\lambda 1487$	
T_e	O III] $\lambda 1666/\lambda 5007$	O III] $\lambda 1666/\lambda 5007$
$\log U$		C IV] $\lambda \lambda 1548, 51$ / C III] $\lambda \lambda 1907, 9$ EW(C IV] $\lambda \lambda 1548, 51$)		

Note. Same as Table 2.

range $10^3 - 10^6 \text{ cm}^{-3}$. At the highest-ionization levels ($E > 40 \text{ eV}$), possible diagnostics are [Ar IV] $\lambda 4714/\lambda 4741$ in the optical and N IV] $\lambda 1483/\lambda 1487$ in the UV, sensitive up to $n_e \sim 1 \times 10^5 \text{ cm}^{-3}$ and $n_e \sim 1 \times 10^6 \text{ cm}^{-3}$, respectively.

In general, the predictions by PyNeb accurately represent the line ratios observed within the uncertainties, which can unfortunately be very large for some transitions. In these cases, our measurements can be considered upper limits of the density. Moreover, from Figure 3, it is clear that the density diagnostics have generally a very low dependence on T_e . The highest dependence on temperature is found for the N IV] $\lambda 1483/\lambda 1487$ line ratio, whose derived densities can be different up to ~ 1 dex, with the highest values derived for the lowest temperatures and vice versa.

The main aspect highlighted by Figure 3 is that the density range traced by the different diagnostics can vary considerably. This depends on the critical density, which is defined as the density at which collisional transitions are equally probable with radiative transitions (Osterbrock 1989; Osterbrock & Ferland 2006). Hence, transitions with higher critical densities can be used as diagnostics in denser environments. Interestingly, we noticed that higher critical densities do not automatically correspond to higher ionization (see upper panels of Figure 3), which means that the density structure could be not directly related to the ionization structure. For instance, Si III] and C III] transitions are characterized by a lower ionization

potential than [Ar IV] or N IV], but overall they can probe higher densities than [Ar IV] and similar values to N IV]. We will further comment about this in Sections 5.2 and 6.2. Also, [Fe III] has an ionization potential comparable to [S II] or [O II], but it is probing electron densities between 10^3 and 10^6 cm^{-3} .

Finally, the shaded red regions in Figure 3 show the predictions from the Cloudy 17.00 (Ferland et al. 2013) models from Berg et al. (2019b, 2021), which we used to estimate the ionization parameter, as we discuss in Section 4.4. The Cloudy models we took into account are made using Binary Population and Spectral Synthesis (BPASSv2.14; Eldridge & Stanway 2016; Stanway et al. 2016) burst models for the input ionizing radiation field. The parameter space covered is appropriate for our sample, including an age range of 1–10 Myr for young bursts and a range in ionization parameter of $4.0 < \log(U) < 0$, matching stellar and nebular metallicities ($Z_* = Z_{\text{neb}} = 0.001, 0.002, 0.004, 0.008$, corresponding to 0.05, 0.10, 0.20, 0.40 Z_\odot). In particular, Berg et al. (2019b) used the GASS10 solar abundance ratios (including dust) to initialize the relative gas-phase abundances, then scaling them to match the observed values for nearby metal-poor dwarf galaxies. Specifically, we calculated the median value of Cloudy predictions in the range of densities and temperatures taken into account, and the boundaries of the shaded red regions represent the $\pm 3\sigma$ of the distribution. These regions appear narrow because of the very low dependence of the density on the temperature (see Berg et al. 2018, 2019b, 2021 for all the details). Overall, from Figure 3 we find good agreement between Cloudy and PyNeb, despite minor differences in the default atomic data used by each code. The main difference that we underline is that Cloudy models for [Ar IV] are shifted toward higher densities. This discrepancy implies that Cloudy [Ar IV] densities could be $\lesssim 1$ dex higher than those measured with PyNeb. This discrepancy could be due to the different atomic data used by Cloudy (see Juan de Dios & Rodríguez 2017, 2021 and references within for more details). Finally, we note that our Cloudy models do not include [Fe III] lines.

4.3. Temperature

The temperature T_e can be determined via the intensity ratios of particular emission-line doublets, emitted by a single ion from two levels with considerably different excitation energies (Osterbrock 1989). To guide the reader, we show the available temperature diagnostics used within this study in the six panels

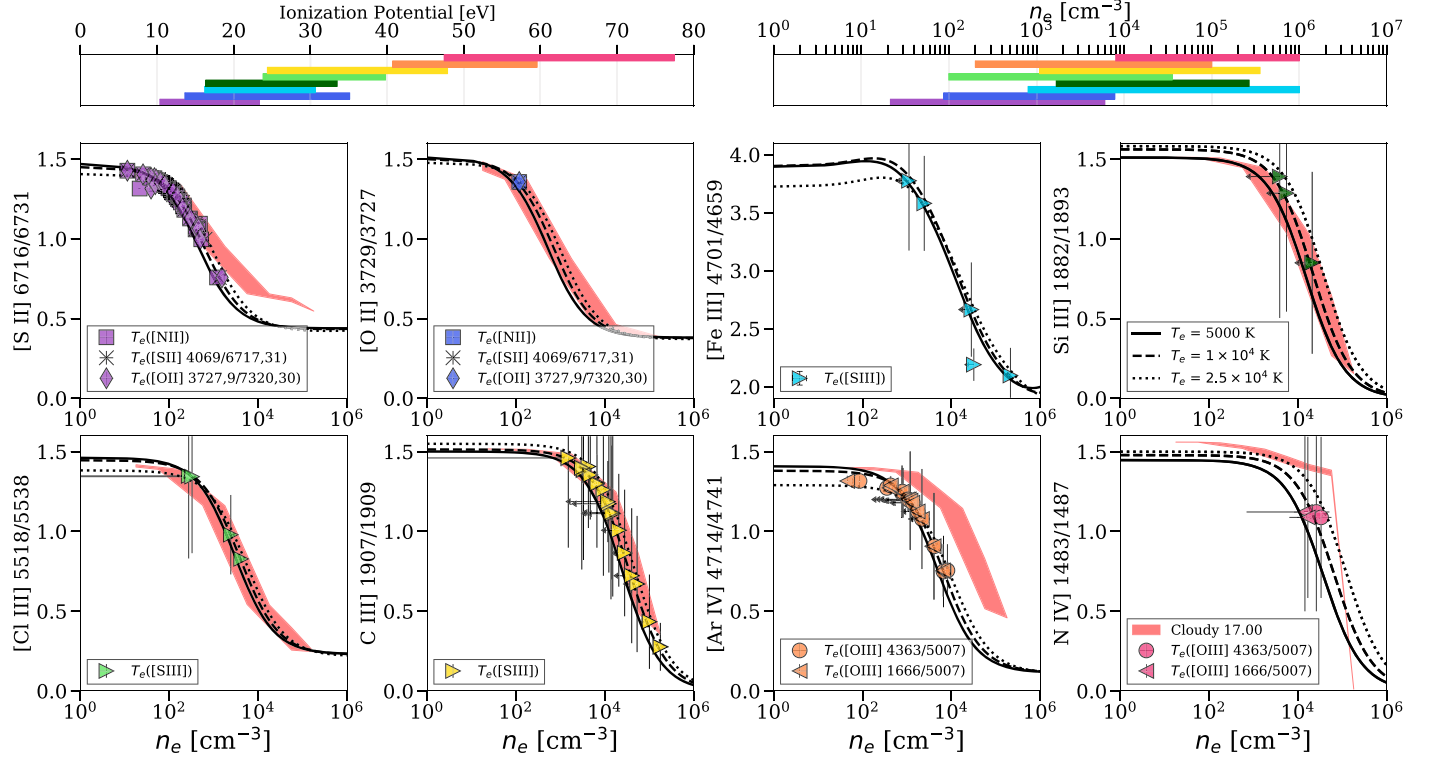


Figure 3. The eight square panels show the set of diagnostics to estimate the gas density n_e in the different ionization zones (see also Tables 2 and 3). The minor top left and right panels show the ionization potential and the range of traced densities of the diagnostics taken into account, calculated with `PYNeb`, using the same color coding. Specifically, in order of ionization potential, we have: [S II] $\lambda 6717/\lambda 6731$ (purple), [O II] $\lambda 3729/\lambda 3727$ (blue), [Fe III] $\lambda 4701/\lambda 4659$ (turquoise), [Si III] $\lambda 1883/\text{Si III } \lambda 1892$ (dark green), [Cl III] $\lambda 5518/\lambda 5538$ (green), [C III] $\lambda 1907/\text{C III } \lambda 1909$ (gold), [Ar IV] $\lambda 4714/\lambda 4741$ (orange), and [N IV] $\lambda 1483/\lambda 1487$ (red). The different symbols show the CLASSY calculated values with `PYNeb` using the available temperature diagnostics described in Figure 4. The solid, dashed and dotted black curves represent the `PYNeb` predictions at $T_e = 5 \times 10^3$ K, 1×10^4 K, and 2.5×10^4 K, as reported in the legend, while the shaded red regions (very narrow due to the low dependence of the density on the temperature) show the predictions from our Cloudy models of Berg et al. (2019b, 2021).

of Figure 4, as introduced in Tables 2 and 3. In Figure 4, we also report the measurements of each line ratio for the CLASSY galaxies and its corresponding temperature, using symbols and colors consistent with Figure 3, to indicate which density diagnostic we used while calculating the temperature using the `getCrossTemDen` task, as reported in the legend.

Overall, the most used optical T_e tracers are given by [N II] $\lambda 5755/\lambda 6584$, [S III] $\lambda 6312/\lambda 9069$, and [O III] $\lambda 4363/\lambda 5007$ for the low-, intermediate-, and high-ionization zones, respectively. Indeed, [N II] emission is stronger in the outer parts of H II regions, where the ionization is lower and O mostly exists as O^+ (Osterbrock 1989). With respect to the low-ionization zone in particular, other available temperature indicators are the [S II] $\lambda \lambda 4069/\lambda \lambda 6717,31$ and [O II] $\lambda \lambda 3727,29/\lambda \lambda 7320,30$ line ratios. Their main drawback is the wide separation in wavelength, that introduces larger relative uncertainties via the dust attenuation correction. Also, [S II] $\lambda 4069$ is usually very faint, while [O II] $\lambda \lambda 7320,30$ lines can be affected by telluric absorption depending on the redshift of the galaxy.

Unfortunately, [N II] $\lambda 5755/\lambda 6584$ and [S III] $\lambda 6312/\lambda 9069$ lines are not available for all the targets, given the very faint nature of the [N II] $\lambda 5755$ and [S III] $\lambda 6312$ auroral lines, and the fact that [S III] $\lambda 9069$ can fall out of the observed wavelength range, depending on the redshift of the source. In these cases, to estimate the temperature of the low- and intermediate-ionization regions, in our iterative procedure we used the Garnett (1992) relations that link $T_e([\text{N II}])$ and $T_e([\text{S III}])$ to

$T_e([\text{O III}])$:

$$T_e([\text{N II}]) / [\text{K}] = 0.70 \times T_e([\text{O III}]) + 3000, \quad (1)$$

$$T_e([\text{S III}]) / [\text{K}] = 0.83 \times T_e([\text{O III}]) + 1700. \quad (2)$$

These derived values are not reported in Figure 4 for the sake of clarity, but do show good agreement with the `PYNeb` curves. For high-redshift targets, the O III] $\lambda 1666/\lambda 5007$ has been explored as temperature diagnostics, as this ratio can be helpful for those cases where the optical auroral line is not available (weak, undetected lines, or outside of the observed wavelength range; Villar-Martín et al. 2004; James et al. 2014; Steidel et al. 2014; Berg et al. 2016; Vanzella et al. 2016; Kojima et al. 2017; Pérez-Montero & Amorín 2017; Patrício et al. 2018; Sanders et al. 2020).

Comparing the fifth and sixth panels of Figure 4, we notice that in general the O III] $\lambda 1666/\lambda 5007$ dependence on temperature is steeper than [O III] $\lambda 4363/\lambda 5007$, suggesting that in principle O III] $\lambda 1666/\lambda 5007$ could represent a better T_e diagnostic (see also Kojima et al. 2017; Nicholls et al. 2020). However, in practice it is worth noting that several issues arise in deriving ratios from optical and UV emission lines. First, there can be flux matching issues and mismatched aperture effects, if observations are taken with different instruments, as we discuss in detail in Appendix A. A second drawback to take into account is the large uncertainties resulting from reddening estimates derived over such a large wavelength window. Finally, there can be an intrinsic effect due to the density,

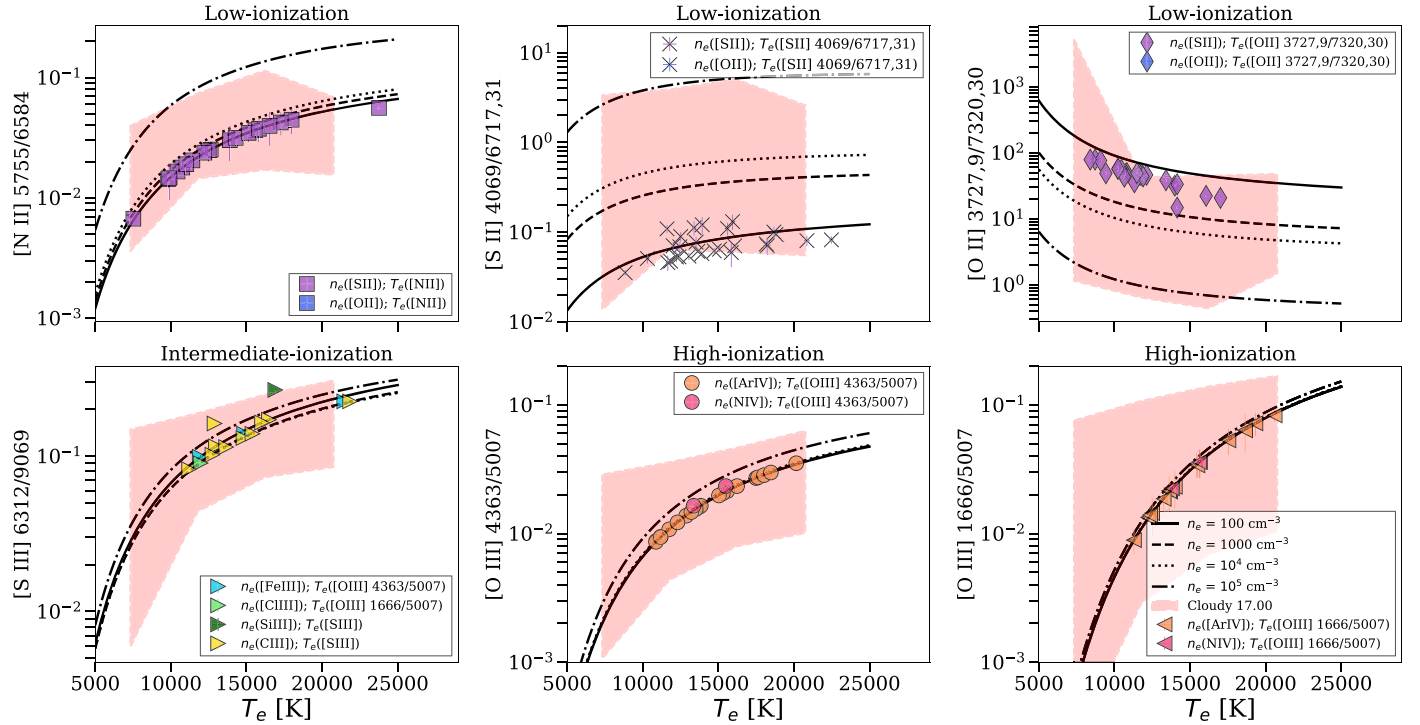


Figure 4. Set of diagnostics to estimate the gas temperature in the CLASSY galaxies in the different ionization zones: [N II] $\lambda 5755$ /[N II] $\lambda 6584$, [S II] $\lambda \lambda 4069$ /[S II] $\lambda \lambda 6717,31$, and [O II] $\lambda \lambda 3727,29$ /[O II] $\lambda \lambda 7320,30$ for the low-ionization zone, [S III] $\lambda 6312$ /[S III] $\lambda 9069$, [O III] $\lambda 4363$ /[O III] $\lambda 5007$, and O III] $\lambda 1666$ /[O III] $\lambda 5007$. The different filled symbols show the CLASSY calculated values with `PyNeb`, as reported in the legend. The black curves represent `PyNeb` predictions at densities $n_e = 100 \text{ cm}^{-3}$, 5000 cm^{-3} , 10^4 cm^{-3} , and 10^5 cm^{-3} , while the shaded red regions show the predictions from our `Cloudy` models.

temperature, and ionization structure of star-forming regions. Indeed, if the ISM is patchy, the UV light is visible only through the less dense and/or less reddened regions along the line of sight, while the optical may be arising also from denser and/or more reddened regions. To further discuss this, in Sections 5.3 and 6.3, we show the comparison of temperatures derived with O III] $\lambda 1666$ / $\lambda 5007$ and [O III] $\lambda 4363$ / $\lambda 5007$, and the resulting difference in deriving $12+\log(\text{O}/\text{H})$.

Finally, Figure 4 highlights a very low dependence of the intermediate- and high-ionization temperature diagnostics on n_e . Concerning the low-ionization temperature diagnostics, the dependence on the density is higher, but the comparison with the observed line ratios used as diagnostics indicate that only $n_e < 10^4 \text{ cm}^{-3}$ are feasible. This is in line with the fact that these line ratios are tracing the external and more diffuse regions of nebulae.

4.4. Ionization Level

Another important parameter of the ISM is the ionization parameter, $\log(U)$, defined as the ratio of the number of ionizing photons to the density of hydrogen atoms. Empirically, this property is best determined by ratios of emission lines of the same element with a different ionization stage, such as the $\text{O3O2} = [\text{O III}] \lambda 5007 / [\text{O II}] \lambda \lambda 3727,29$ and $\text{S3S2} = [\text{S III}] \lambda \lambda 9069,9532 / [\text{S II}] \lambda \lambda 6717,31$ line ratios (e.g., Kewley et al. 2019). Usually, O3O2 is the most widely used proxy in the optical range because these oxygen lines lie in a wavelength range accessible to many different instruments and are among the strongest line in the optical range. Also, they nicely span the entire energy range of an H II region (Berg et al. 2021). However, O3O2 is strongly dependent on metallicity (Kewley & Dopita 2002; Kewley et al. 2019). S3S2 is

less commonly used because the near-infrared (NIR) [S III] $\lambda \lambda 9069,9532$ lines are weaker than their oxygen counterparts and lie at wavelengths that are less frequently covered together with [S II] lines. Moreover, the NIR wavelength range suffers more from telluric absorption and sky line contamination. Nevertheless, given the redder wavelengths of the sulfur emission lines, and consequently their lower excitation energies with respect to oxygen, S3S2 is less affected by the metallicity and also insensitive to the ISM pressure (Dopita & Evans 1986; Kewley & Dopita 2002; Kewley et al. 2019; Mingozzi et al. 2020). The lower excitation energies of [S II] and [S III] also imply that this ratio is tracing the ionization parameter of the low-ionization regions of nebulae (see, e.g., Figure 4 in Berg et al. 2021). Finally, Berg et al. (2021) introduced the $\text{Ar4Ar3} = [\text{Ar IV}] \lambda \lambda 4714,71 / [\text{Ar III}] \lambda 7138$ ratio as an ionization parameter tracer of the very-high-ionization region.

In our analysis, in order to calculate $\log(U)$, we used the calibration of Berg et al. (2018) for O3O2 (see their Table 3) and the one of Berg et al. (2021) for S3S2 and Ar4Ar3 (see their Table 4). These calibrations relate these line ratios and $\log(U)$ as a function of the gas metallicity and are obtained using the set of `Cloudy` models described in Sections 4.2 and 4.3, where we showed their agreement with both our observed line ratios and the `PyNeb` predictions. To calculate the corresponding $\log(U)$ of each CLASSY galaxy, we assumed the gas-phase metallicity reported in Table 1.

Given that [S III] $\lambda \lambda 9069, 9532$ is outside the observed wavelength range for many CLASSY galaxies, and the [Ar IV] $\lambda \lambda 4714,4741$ and [Ar III] $\lambda 7138$ lines can be faint and thus below the required S/N threshold of 3, we can measure the S3S2 and Ar4Ar3 line ratios only in 20 and 28 CLASSY galaxies, respectively. On the other hand, we can calculate the O3O2 line ratios for all the galaxies of our sample, apart from

J1444+4237. For the 18 CLASSY galaxies with $[\text{O II}]\lambda\lambda 3727,9$ outside the observed wavelength range, we estimated O3O2 using the emissivities of $[\text{O II}]\lambda\lambda 3727,9$ and $[\text{O II}]\lambda\lambda 7320,30$ obtained with PYNeb , where calculations were performed using n_e and T_e associated to the low-ionization emitting zone. It is thus possible to recover $[\text{O II}]\lambda\lambda 3727,9$ by multiplying the calculated empirical ratio with the observed $[\text{O II}]\lambda\lambda 7320,30$ line fluxes (see also Paper V). In Section 5.4 we describe our results, while in Section 6.4 we discuss how the $\log(U)$ optical tracers relate to potential UV analogs.

5. Results: Comparing UV and Optical Physical Properties of the ISM

5.1. Dust Attenuation Diagnostics

We calculated $E(B - V)$ for the CLASSY galaxies as described in Section 4.1, with the iterative method explained in Section 4, finding values in the range $E(B - V) \sim 0 - 0.5$ mag. To explore the systematic uncertainties on $E(B - V)$ due to the effect of density and temperature variations on the Balmer decrement, we obtained a value for each combination of T_e and n_e estimates for each ionization zone (described in Figures 3 and 4). The top panels of Figure 5 display the $E(B - V)$ values obtained for the low- (pink squares), intermediate- (red diamonds), and high-ionization region (blue circles) densities and temperatures as a function of $12 + \log(\text{O}/\text{H})$ and stellar mass, on the left and right, respectively. We also show $E(B - V)_0$, which we define assuming $n_e = 10^2 \text{ cm}^{-3}$ and $T_e = 1 \times 10^4 \text{ K}$ (empty black pentagons), usually considered appropriate conditions for star-forming regions (Osterbrock 1989; Osterbrock & Ferland 2006). The dashed lines colored accordingly indicate the median values. The Pearson correlation factors are $R \sim 0.50$ for $12 + \log(\text{O}/\text{H})$ and $R \sim 0.63$ for stellar mass, with a p value of $p \sim 1 \times 10^{-3}$ and $p \sim 5 \times 10^{-6}$, respectively.

The lower panels show the difference between $E(B - V)_0$ and the values calculated assuming the coherent density and temperature of the different ionization zones, expressed in [mag]:

$$\Delta(E(B - V)) = E(B - V)_0 - E(B - V),$$

where $E(B - V)_0$ is the value derived with $n_e = 10^2 \text{ cm}^{-3}$ and $T_e = 1 \times 10^4 \text{ K}$. The median values and the 68% intrinsic scatter of the distributions are shown by the dotted lines and shaded regions (mostly overlapped), color coded correspondingly.

Even though the difference in the colored dots with respect to $E(B - V)_0$ looks small, with an overall median value around ~ -0.01 mag and similar intrinsic scatter, there are a few objects with discrepancies down to ~ -0.04 mag, at $12 + \log(\text{O}/\text{H}) \lesssim 7.75$ or stellar masses $\log(M_*/M_\odot) \lesssim 6.5$. Specifically, $E(B - V)$ is generally larger than $E(B - V)_0$ (of ~ -0.01 mag on average, or ~ -0.05 dex), while at higher $12 + \log(\text{O}/\text{H})$ their difference tends to 0. Therefore, assuming $T_e = 1 \times 10^4 \text{ K}$ and $n_e = 10^2 \text{ cm}^{-3}$ can lead to underestimates in the dust attenuation, especially at low $12 + \log(\text{O}/\text{H})$, where T_e is higher (see Section 5.3). This is due to the slight dependence of the recombination lines on the temperature and density, which still causes the Balmer decrement to drop from ~ 2.86 to ~ 2.70 (Osterbrock 1989; Osterbrock & Ferland 2006). The fact that the low-, intermediate-, and high-ionization $E(B - V)$ values are consistent within their uncertainties indicates that a simpler approach, considering a single value of the

density and temperature that represents all zones, can be used to correct the emission lines without introducing a significant bias in the results. Hence, for our analysis we used the weighted average of these values (defined generically as $E(B - V)$ hereafter), to correct both the UV and optical emission lines as explained in Section 4.1.

5.2. Density Diagnostics

In the left and right upper panels of Figure 6 we show the optical and UV density diagnostics as a function of $12 + \log(\text{O}/\text{H})$. In both panels we also display the low-ionization density obtained through $[\text{S II}]\lambda\lambda 6717/\lambda\lambda 6731$ (purple squares) as a reference. For galaxy J0934+5514, we estimate the low-ionization density from $[\text{O II}]\lambda\lambda 3729/\lambda\lambda 3729$ (blue square), as KCWI data do not cover $[\text{S II}]\lambda\lambda 6717,31$ lines. For the optical, we show the intermediate-ionization density derived from $[\text{Cl III}]\lambda\lambda 5518/\lambda\lambda 5538$ (green left-pointing triangles) and $[\text{Fe III}]\lambda\lambda 4701/\lambda\lambda 4659$ (turquoise left-pointing and blue right-pointing triangles), and the high-ionization density from $[\text{Ar IV}]\lambda\lambda 4714/\lambda\lambda 4741$ (orange pentagons). For the UV, instead, we show the intermediate-ionization density derived from $[\text{Si III}]\lambda\lambda 1883/\text{Si III}]\lambda\lambda 1892$ (dark green up-pointing triangles) and $[\text{C III}]\lambda\lambda 1907/\text{C III}]\lambda\lambda 1909$ (gold down-pointing triangles), and the high-ionization density from $\text{N IV}]\lambda\lambda 1483/\lambda\lambda 1487$ (red hexagons) values. Overall, the values obtained span from $n_e \sim 30 \text{ cm}^{-3}$ to $n_e \sim 10^5 \text{ cm}^{-3}$. The dashed lines represent the median value of the density given by each diagnostic and are color coded accordingly.

In the bottom panels of Figure 6, we show the difference in dex between the low-ionization zone density and the other values ($\Delta(\log(n_e)_{[\text{S II}]})$), keeping the same color coding of the main panel. The dotted lines show the median values of the offsets in dex, which are ~ -0.8 , ~ -2.3 , and ~ -0.9 dex, for $[\text{Cl III}]$, $[\text{Fe III}]$, and $[\text{Ar IV}]$, and ~ -1.3 , ~ -2.0 , and ~ -2.1 dex for $[\text{Si III}]$, $[\text{C III}]$, and $\text{N IV}]$, respectively, sorting the optical and UV diagnostics as a function of the increasing ionization potential. The 68% intrinsic scatter of each distribution is shown by the shaded regions, color coded correspondingly. The partial overlaps indicate a similar behavior of the distributions.

We note that $[\text{Ar IV}]$ densities are slightly larger than $[\text{S II}]$ densities with values on average around $\sim 1000 \text{ cm}^{-3}$, while $[\text{S II}]$ densities are always lower than $\sim 1000 \text{ cm}^{-3}$. This is expected because $[\text{Ar IV}]$ densities have a higher critical density than $[\text{S II}]$, which instead traces the low-ionization and diffuse gas within nebulae (see Figure 3). Interestingly, we find that in the optical, the $[\text{Ar IV}]$ densities that trace the high-ionization regions are somewhat lower than expected when compared to their UV counterparts $\text{N IV}]$ and are instead consistent with $[\text{Cl III}]$ values, which trace the intermediate-ionization regions. Also, we note that when comparing the UV and optical diagnostics, both the $[\text{Ar IV}]$ and $[\text{Cl III}]$ densities are lower than those derived from $[\text{C III}]$ and $[\text{Si III}]$ in the UV, which are both tracers of intermediate-ionization regions. On the other hand, $[\text{Fe III}]$, which is characterized by an ionization potential lower than $[\text{Cl III}]$, traces similar densities to the UV diagnostics, but the values can only be considered upper limits due to the large error bars. Excluding $[\text{Fe III}]$, clearly the highest discrepancies with respect to $n_e([\text{S II}])$ are found for UV tracers, which predict average densities around $\sim 10^4 \text{ cm}^{-3}$.

We will further comment about this in Section 6.2. As expected, we find no correlation between $\log(n_e)$ (and also Δ

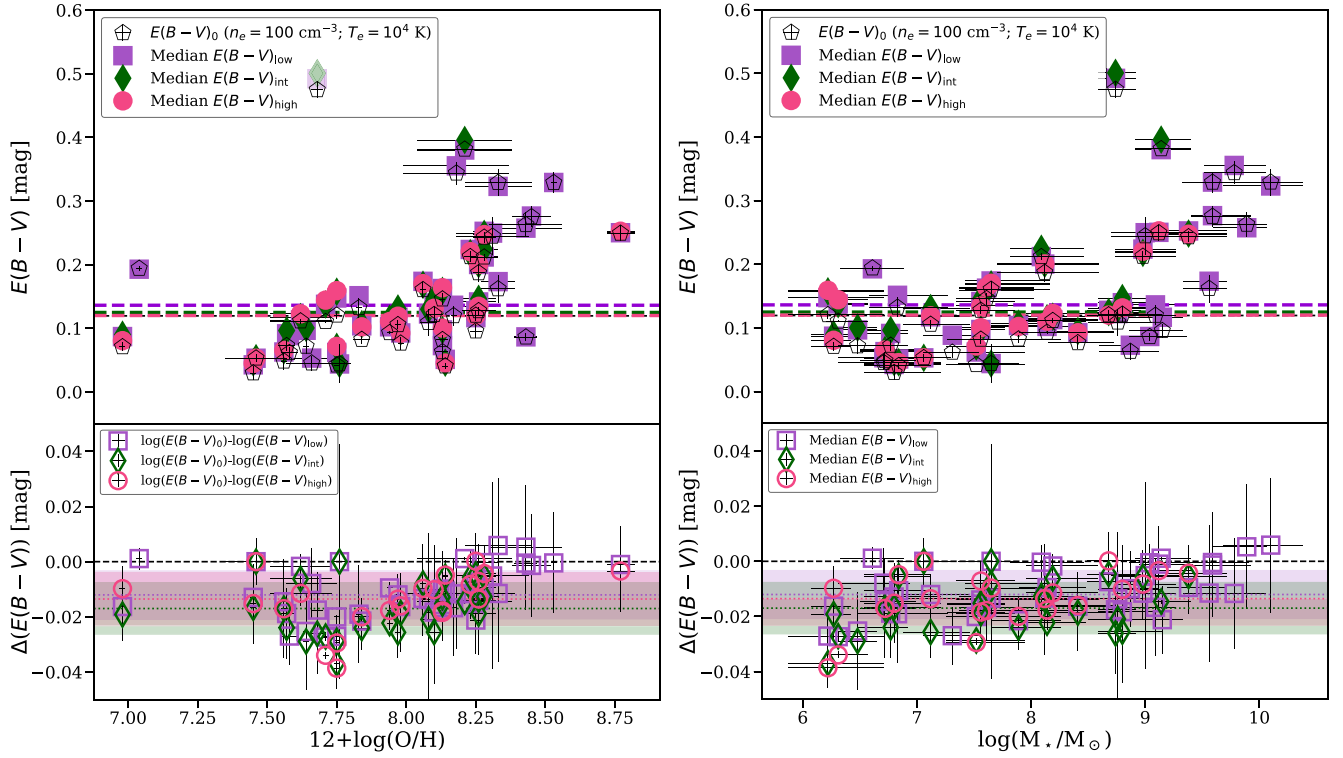


Figure 5. Top panels: comparison of the $E(B-V)$ estimated assuming $T_e = 1 \times 10^4$ K and $n_e = 10^2 \text{ cm}^{-3}$ ($E(B-V)_0$; empty black pentagon) with the value obtained from low- (purple squares), intermediate-, (green diamonds) and high-ionization regions (red circles), as a function of $12+\log(\text{O}/\text{H})$ and M_* . The uncertainties on the displayed quantities are shown in both axes. Bottom panels: difference between the $E(B-V)_0$ and $E(B-V)$ measurements of each ionization zone, keeping the same symbols and colors as in the top panel. The colored dashed and dotted lines indicate the median values of the shown distributions. The shaded regions (partially overlapped) in the bottom panel represent the 68% intrinsic scatter of each distribution, color coded accordingly. At $12+\log(\text{O}/\text{H}) \lesssim 7.75$ or stellar mass $\log(M_*/M_\odot) \lesssim 6.5$, $E(B-V)$ is down to ~ -0.04 mag lower than $E(B-V)_0$.

$(\log(n_e)_{[\text{SII}]})$ and $12+\log(\text{O}/\text{H})$, as well as the other galaxy properties, such as the stellar mass, stellar metallicity, stellar age, or SFR.

5.3. Temperature Diagnostics

The left and right upper panels of Figure 7 show the comparison between the low- and intermediate-ionization region temperatures inferred through the Garnett (1992) relations (Equations (1) and (2), respectively) as a function of the high-ionization zone temperature $T_e([\text{O III}] \lambda 4363/5007)$, to see to what extent they give consistent results. Specifically, in the left panel of Figure 7 we report the three different low-ionization T_e estimates made with $[\text{N II}] \lambda 5755/\lambda 6584$ (purple squares), $[\text{S II}] \lambda 4069/\lambda \lambda 6717,31$ (pink dots), and $[\text{O II}] \lambda \lambda 3727,29/\lambda \lambda 7320,30$ (blue diamonds), using the $[\text{S II}] \lambda \lambda 6717,31$ doublet as a density tracer (and the $[\text{O II}] \lambda \lambda 3727,29$ doublet for J0934+5514). On the right panels there are no estimates of $T([\text{S III}]([\text{Cl III}],[\text{S III}]])$, because we could not find finite values with PyNeb , and only one galaxy for which we measured $T([\text{S III}]([\text{Si III}],[\text{S III}]])$. In general, the low-ionization temperatures obtained are in the range $T_e \sim 8000 - 24000$ K. The bottom panels of Figure 7 report the differences in dex between the values obtained with the relations from Garnett (1992) and the T_e inferred through the different temperature diagnostics. We note that the median values (dotted lines) in these subpanels are close to zero (the median values are ~ -0.1 dex), but systematically below, with a better agreement with Equation (1) for $T_e([\text{S II}] \lambda 4069/\lambda \lambda 6717,31)$ and $T_e([\text{O II}] \lambda \lambda 3727,29/\lambda \lambda 7320,30)$ with respect to $T_e([\text{N II}] \lambda 5755/\lambda 6584)$. Also the 68%

intrinsic scatter of the distributions, shown by the shaded regions color coded correspondingly, show a similar behavior (i.e., mostly overlapped). However, we note that Equation (1) tends to underestimate the temperature up to ~ 0.2 dex.

Figure 7 shows that the intermediate-ionization T_e derived with $[\text{S III}] \lambda 6312/\lambda 9069$ are better in agreement with Garnett (1992)'s relation with respect to the low-ionization T_e discussed in the previous paragraph. To summarize, several authors found significant differences with Garnett (1992)'s relations using large samples of star-forming galaxies (e.g., Kennicutt et al. 2003; Binette et al. 2012; Berg et al. 2015). A possible interpretation of the larger discrepancy that we find for Equation (1) than for Equation (2) could be explained by the large absorption cross section of low-energy ionizing photons (Osterbrock 1989), which are thus preferentially absorbed in the H II regions with respect to higher-energy ones, leading to a hardened spectrum (e.g., Hoopes & Walterbos 2003). An implication would be that the low-ionized regions of the H II regions could have higher temperatures than the high-ionized regions, as observed. However, galaxies characterized by very high excitation such as those covered by the CLASSY survey are expected to have minimal contributions from the low-ionization zone temperatures for the oxygen abundance (Berg et al. 2021). In this respect, we feel confident that for those galaxies in our sample for which we used the Garnett (1992) relation (i.e., 23 using Equation (1) and 13 using Equation (2)), the derived T_e values are reliable estimates.

Concerning the high-ionization temperature, the main panel of Figure 8 compares the values obtained iteratively with either

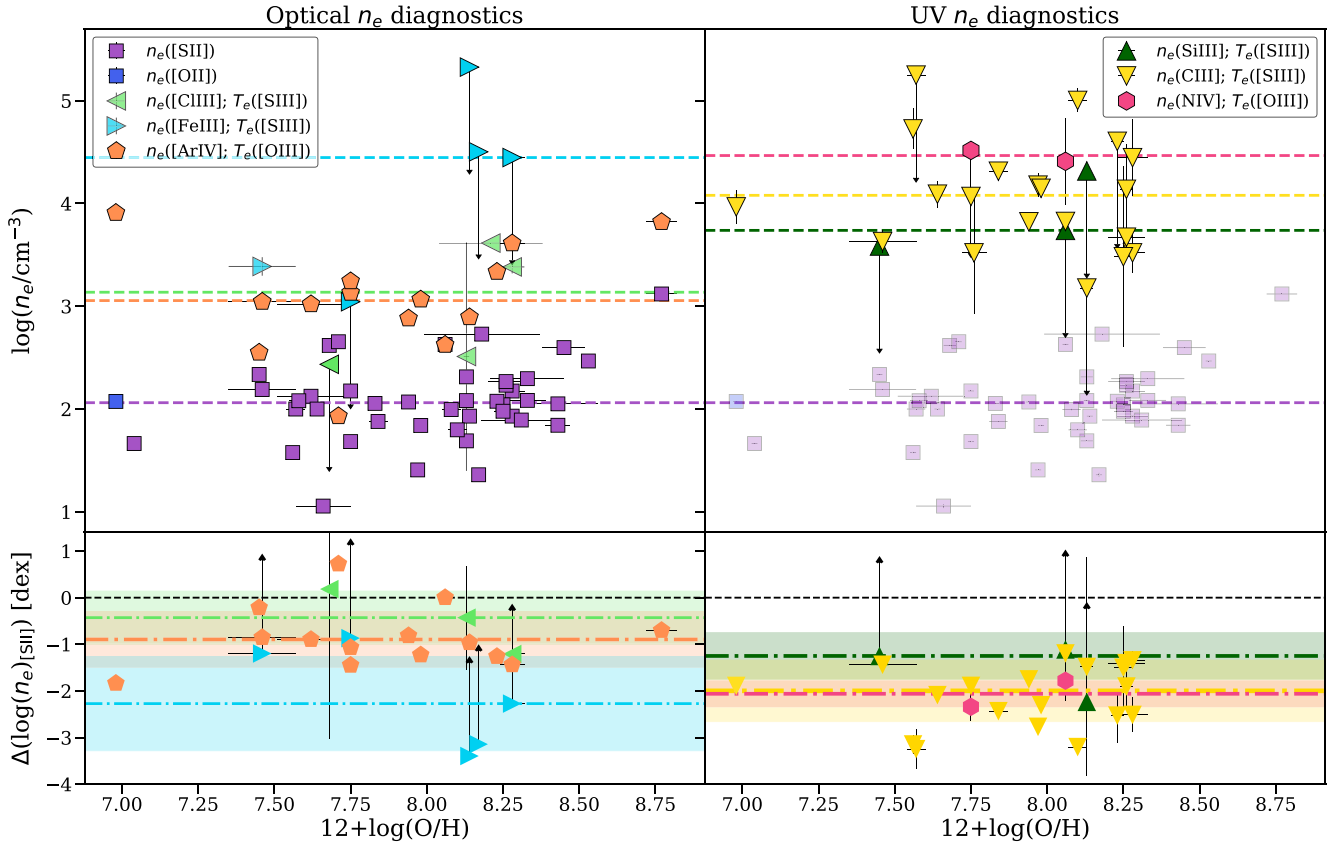


Figure 6. Top panels: comparison of n_e estimated from low- (n_e ([S II]) or n_e ([O II]) for J0934+5514; squares), intermediate- (n_e ([C III]), n_e ([Fe III]), n_e ([Si III]), n_e ([C III])); triangles), and high-ionization regions (n_e ([Ar IV]), n_e ([N IV])); pentagons, hexagons), as a function of $12+\log(\text{O}/\text{H})$. For clarity reasons the optical and UV diagnostics are shown on the left and right, respectively, while the optical n_e ([S II]) or n_e ([O II]) are shown in both panels. The dots are color coded consistently with Figure 3, as indicated in the legend. The uncertainties on the displayed quantities are shown in both axes. Bottom panels: difference in dex between the low-ionization density (purple squares) and the other n_e measurements, keeping the same symbols as in the top panel. The colored dashed and dotted lines indicate the median values. The shaded regions (partially overlapped) in the bottom panel represent the 68% intrinsic scatter of each distribution, color coded accordingly. Excluding n_e ([Fe III]) for which we have mainly upper limits, clearly the highest discrepancies with respect to n_e ([S II]) are found for UV tracers, which predict average densities $\sim 1 - 2$ dex higher.

[O III] $\lambda 4363/\lambda 5007$ or the hybrid UV–optical ratio O III] $\lambda 1666/\lambda 5007$ and the [S II], [Ar IV], and N IV] density diagnostics, as reported in the legend. We note differences lower than $\lesssim 1000$ K using either [S II], [Ar IV], or N IV], confirming again the low dependence of the temperature on the density diagnostics, even when the difference in $\log(n_e)$ can be as large as ~ 2 dex. In general, the values are roughly in agreement with the dashed black line that indicates the 1:1 relation. To better evaluate this, the bottom panel shows the difference between T_e ([O III] $\lambda 4363/\lambda 5007$) and T_e (O III] $\lambda 1666/\lambda 5007$) in dex ($\Delta \log(T_e)_{\text{opt-hybrid}}$), keeping the same symbols and colors of the main panel. $\Delta \log(T_e)_{\text{opt-hybrid}}$ is in median ~ -0.025 dex (~ 1000 K), with the highest temperatures measured with [O III] $\lambda 1666/\lambda 5007$. This trend is consistent with other works in the literature that made the same comparison in smaller samples (e.g., Berg et al. 2016). We comment more on the offset $\Delta \log(T_e)_{\text{opt-hybrid}}$ and its impact on the estimate of $12+\log(\text{O}/\text{H})$ in Section 6.3.

5.4. Ionization Parameter Diagnostics

The upper panel of Figure 9 shows the comparison of $\log(U)$ estimated from low- (purple squares), intermediate- (green diamonds), and high-ionization regions (orange circles) as a function of $12+\log(\text{O}/\text{H})$, using the S3S2, O3O2, and Ar4Ar3 line ratios, respectively, as explained in Section 4.4. Figure 9

demonstrates that in our sample there is not an evident anticorrelation between $\log(U)$ (O3O2) and metallicity ($r \sim -0.3$, $p \sim 0.05$), which is instead predicted by the theoretical relation presented in Dopita & Evans (1986) and Dopita et al. (2006). This would be expected as a consequence of the enhanced opacity of stellar winds and higher level of scattering at increasing metallicity. The former factor would lead to a decrease in the ionizing photons in the surrounding H II region, while the latter to a greater conversion efficiency from luminous energy flux to mechanical energy flux, hence decreasing $\log(U)$. On the other hand, we notice a slight anticorrelation with $\log(M_*)$ ($r \sim -0.5$, $p \sim 1 \times 10^{-4}$), as suggested in some previous works on local star-forming galaxies (e.g., Dopita et al. 2006; Brinchmann et al. 2008). We also find no correlation with the SFR, which instead has been revealed from some works based on spatially resolved optical spectra (e.g., Dopita et al. 2014; Kaplan et al. 2016). Finally, in agreement with Kewley et al. (2015), Bian et al. (2016), Kaasinen et al. (2018), and Mingozzi et al. (2020), we find a strong correlation between $\log(U)$ (O3O2) and $\log(\text{sSFR})$ ($r \sim 0.7$, $p \sim 1 \times 10^{-8}$). We comment further about this in Section 6.4. We stress that similar results hold for $\log(U)$ (S3S2) and $\log(U)$ (Ar4Ar3).

Interestingly, from Figure 9 we note that using these three different diagnostics we obtain a scatter of values of $\log(U)$, in the range $-3.5 - 0.$, with the lowest values derived from S3S2 and the highest ones with Ar4Ar3. The lower panel of Figure 9

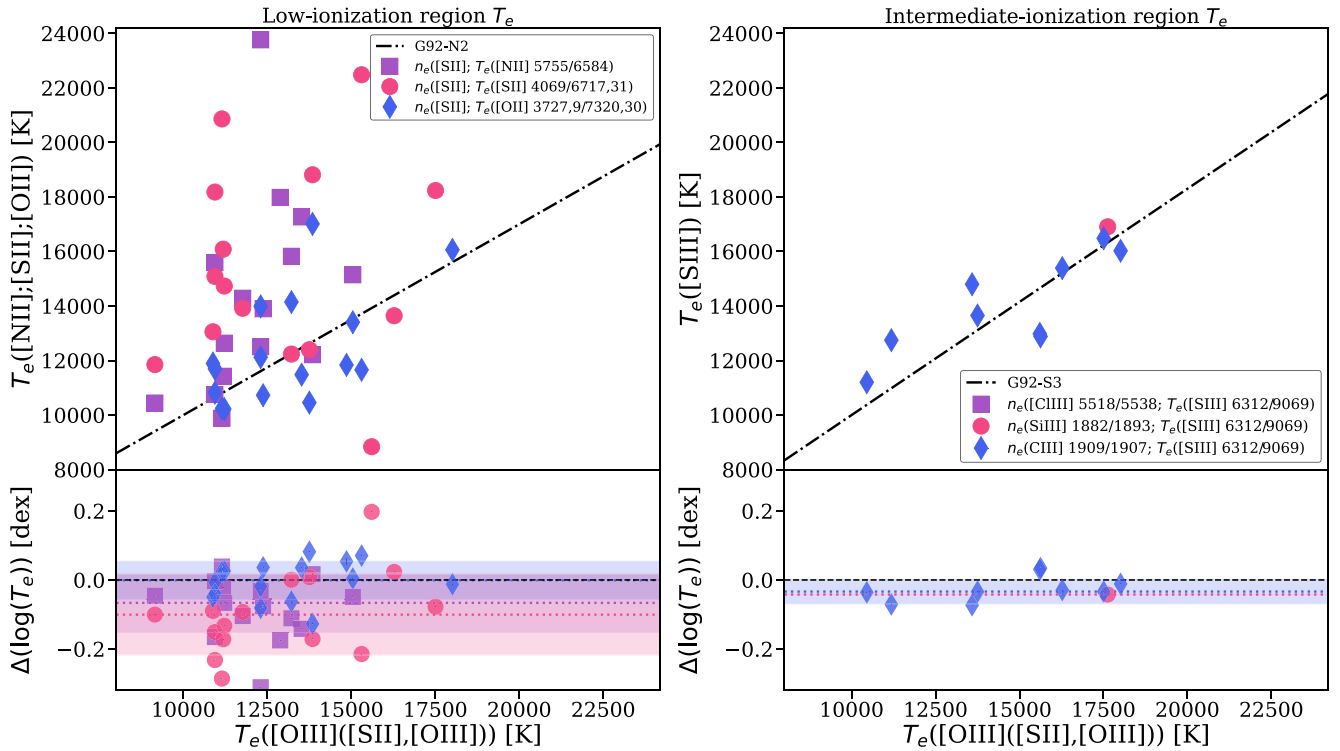


Figure 7. Upper panels: comparison of the T_e estimates of the low-ionization (on the left) and intermediate-ionization (on the right) with the temperature diagnostics [N II] $\lambda 5755/\lambda 6584$, [S II] $\lambda \lambda 4069/\lambda \lambda 6717,31$, [O II] $\lambda \lambda 3727,29/\lambda \lambda 7320,30$, and [S III] $\lambda 6312/\lambda 9071$, as a function of the high-ionization temperature $T_e([O III]([S II],[O III]))$, taking the available density tracers into account. The uncertainties on the displayed quantities are shown in both axes. The dotted-dashed lines in the left and right panels indicate Equation (1) and Equation (2), respectively. On the right panels there are no estimates of $T_e([S III]([C III],[S III]))$, because we could not find finite values with `PyNeb`, and only one measurement for $T_e([S III]([S III],[S III]))$. Lower panels: difference in dex between the prediction of Equation (1) and Equation (2), and the calculated values. The shaded regions (overlapped) in the bottom panel represent the 68% intrinsic scatter of each distribution, color coded accordingly. Overall, the median values of the computed differences are ~ -0.1 dex and ~ -0.05 dex (dotted lines in the minor panels) for the low-ionization and intermediate-ionization T_e , respectively.

illustrates better this scatter, showing the differences $\Delta(\log U)_{O3O2-S3S2}$ and $\Delta(\log U)_{O3O2-Ar4Ar3}$ in purple and orange, respectively (we refer to this quantity as $\Delta(\log U)_{O3O2}$ hereafter), revealing significant discrepancies in the range ± 1 dex. The median values and the 68% intrinsic scatter of the distributions are shown by the dotted lines and shaded regions, color coded correspondingly. Specifically, in our sample $\log(U)_{O3O2}$ is in median ~ 0.4 dex higher than $\log(U)_{S3S2}$ and ~ -0.6 dex lower than $\log(U)_{Ar4Ar3}$. This is in line with the presence of a clear ionization structure in the nebular environments of our targets, as described in Section 4 and in Berg et al. (2021) for CLASSY galaxies J1044+0353 and J1418+2102.

Among the available UV emission lines, only the C IV/C III] line ratio involves emission originating from different ionization states of the same element, and thus could constrain the ionization parameter. We will further discuss this in Section 6.4.

6. The UV Toolkit

In this section we compare the optical and UV diagnostic results detailed in Section 5 and discuss correlations between the gas-phase properties and UV emission lines. Using these relationships, we provide a set of diagnostic equations that can be used to estimate the gas-phase $E(B - V)$, electron density, electron temperature, metallicity, and ionization parameter. Each of these equations relies only on emission lines observed at the rest-frame UV wavelengths and thus represents a *UV*

Toolkit for deriving the chemical and physical conditions of star-forming galaxies.

6.1. UV Diagnostics for $E(B - V)$

Here, we aim to explore the behavior of the gas $E(B - V)$ (obtained with the Balmer decrement and the Cardelli et al. 1989 attenuation law, as described in Section 4.1), and the stellar $E(B - V)_{UV}$ (obtained from the β slope of stellar-continuum fitting and the Reddy et al. 2016 attenuation law, as described in Section 3.1.1). The upper panels of Figure 10 show the comparison between the stellar $E(B - V)_{UV}$ and the gas $E(B - V)$, color coded as a function of the SFR and specific SFR (sSFR), calculated considering the stellar mass and SFR within the COS aperture (see Table 6 in Paper I). The black dashed line shows the 1:1 relation, while the black dotted line shows the empirical relation between the stellar and gas $E(B - V)$ according to Calzetti (1997; C97 hereafter): $E(B - V)_{UV} = (0.44 \pm 0.03) \times E(B - V)$ (or $E(B - V) = (2.27 \pm 0.15) \times E(B - V)_{UV}$).

From Figure 10, we note that there is just a mild correlation between $E(B - V)_{UV}$ and $E(B - V)$ (Pearson factor of ~ 0.43). We notice that the majority of the CLASSY galaxies lies along the 1:1 relation or are within that and the C97 line. The most significant correlation that we observe is between the gas $E(B - V)$ and the difference (in mag) $\Delta(E(B - V)) = E(B - V) - E(B - V)_{UV}$, characterized by a Pearson factor of $\sim +0.78$, as shown in the bottom panel of Figure 10. The linear best fit of the correlation between $\Delta(E(B - V))$ and

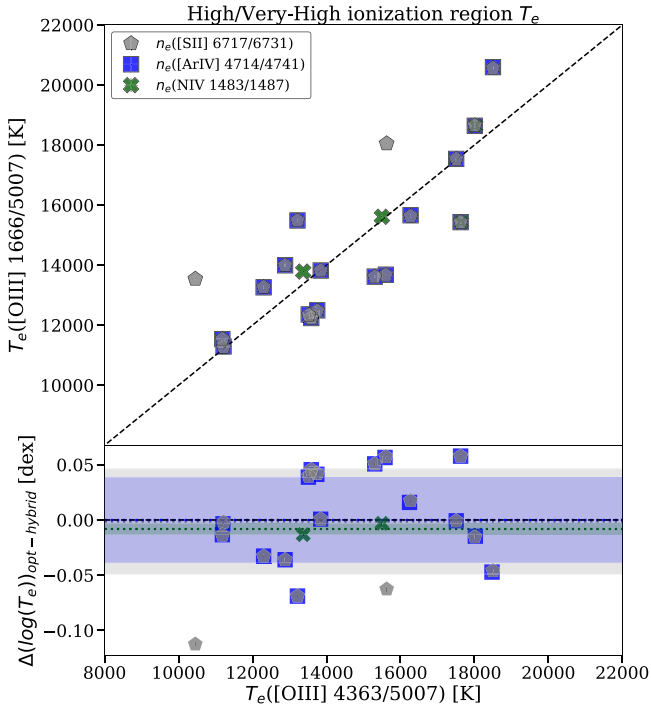


Figure 8. Top panels: comparison of the high-ionization regions $T_e([\text{O III}] \lambda 1666/[\text{O III}] \lambda 5007)$ estimated from the hybrid UV–optical ratio, using $n_e([\text{Ar IV}] \lambda 4714/4741)$ (blue squares on the left) or $n_e([\text{N IV}] \lambda 1483/1487)$ (green crosses on the right), as a function of $T_e([\text{O III}] \lambda 4363/[\text{O III}] \lambda 5007)$. The uncertainties on the displayed quantities are shown in both axes. In general, the values are roughly in agreement with the dashed black line, which represents the 1:1 relation. Bottom panels: difference in dex between $T_e([\text{O III}] \lambda 4363/[\text{O III}] \lambda 5007)$ and $T_e([\text{O III}] \lambda 1666/[\text{O III}] \lambda 5007)$, keeping same symbols and colors as in the top panel. The colored dashed and dotted horizontal lines in the main and minor panels, respectively, show the median values of the displayed quantities.

$E(B - V)$ is indicated by the solid red lines and reported on the upper right of the bottom panels and translates into:

$$\begin{aligned}
 E(B - V)_{\text{UV}} &= (0.33 \pm 0.08) \times E(B - V) \\
 &\quad + (0.03 \pm 0.01) \\
 E(B - V) &= (3.00 \pm 0.70) \times E(B - V)_{\text{UV}} \\
 &\quad - (0.09 \pm 0.04), \quad (3)
 \end{aligned}$$

with a scatter of 0.05, while the dashed and dotted lines represent the 1σ and 2.6σ around the best fit. To infer the best fit (here and in the following sections) we used the *LisFit* package developed by Cappellari et al. (2013), which allows us to perform a robust linear fit taking the uncertainties on both axes and the intrinsic scatter into account. This method also clips outliers, using the robust least trimmed squares (LTS) technique by Rousseeuw & Van Driessen (2006). As explained in Section 3.2.2 of Cappellari et al. (2013), their algorithm adopts an initial guess and performs a first least-squares fit. Then it computes the standard deviation of the residuals, selecting all data points deviating no more than 2.6σ from the fitted relation, performing a final fit for the selected points. The errors on the coefficients are computed from the covariance matrix.

Interestingly, Figure 10 shows that $E(B - V)$ and $E(B - V)_{\text{UV}}$ have similar values at low $\log(\text{SFR})$ and high low $\log(\text{sSFR})$ (and low gas-phase metallicity, as $12 + \log(\text{O}/\text{H})$ correlates with $E(B - V)$; see Figure 5), and are in fact close to

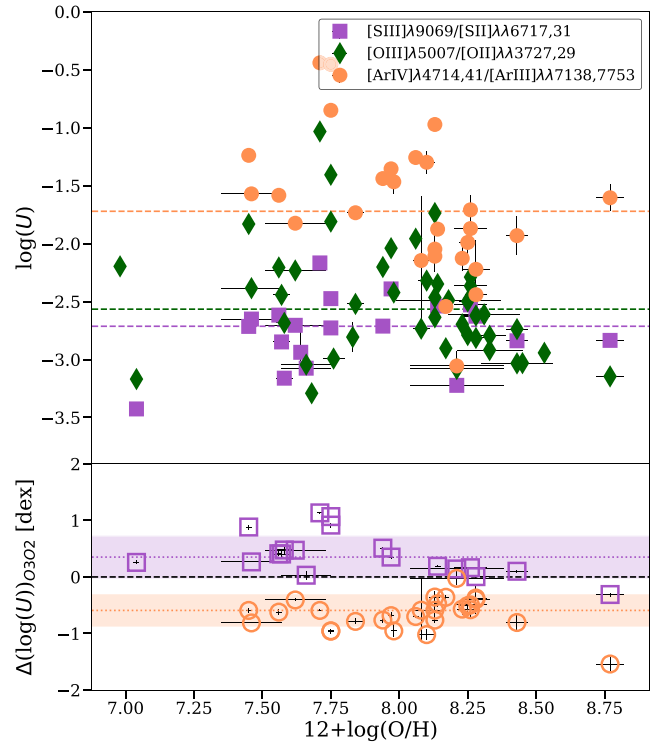


Figure 9. Top panel: comparison of the $\log(U)$ estimated from low- $\text{S}2\text{S}3$; purple squares), intermediate- $\text{O}3\text{O}2$; green diamonds), and high-ionization regions ($\text{Ar}4\text{Ar}3$; orange circles) as a function of $12 + \log(\text{O}/\text{H})$. The uncertainties on the displayed quantities are shown in both axes. Bottom panel: differences $\Delta(\log U)_{\text{O}3\text{O}2 - \text{S}2\text{S}2}$, in purple, and $\Delta(\log U)_{\text{O}3\text{O}2 - \text{Ar}4\text{Ar}3}$, in orange (we refer to this quantity as $\Delta(\log U)_{\text{O}3\text{O}2}$), revealing significant discrepancies in the range ± 1 dex. The colored dashed (in the main panel) and dotted (in the bottom panel) lines indicate the median values. The shaded regions in the bottom panel represent the 68% intrinsic scatter of each distribution, color coded accordingly. This scatter of $\log(U)$ values is in line with the presence of a clear ionization structure in the nebular environments of our targets.

the 1:1 relation (dashed black line) until ~ 0.2 mag. At increasing $\log(\text{SFR})$ and decreasing $\log(\text{sSFR})$, the stellar $E(B - V)_{\text{UV}}$ remains slightly constant with values always below ~ 0.2 mag, while the gas $E(B - V)$ increases, reaching ~ 0.5 mag. This confirms the presence of an excess of dust attenuation in the gas with respect to the stars at high $\log(\text{SFR})$ and low $\log(\text{sSFR})$, in line with the empirical relation found by C97. This relation implies that stars are on average a factor 2 less reddened than the ionized gas, which is related to the fact that the covering factor of the dust is larger for the gas than for the stars (C97). This topic is quite debated, with works suggesting a similar nebular and stellar reddening (e.g., Erb et al. 2006; Reddy et al. 2010; Pannella et al. 2015; Shivaei et al. 2015; Puglisi et al. 2016) and others finding a higher nebular reddening (e.g., Calzetti 1997; Calzetti et al. 2000; Wild et al. 2011b; Kashino et al. 2013; Price et al. 2014; Reddy et al. 2015; Qin et al. 2019; Theios et al. 2019; Shivaei et al. 2020), as nicely summarized in Table 1 in Shivaei et al. (2020).

As explained in C97, the nebular emission requires the presence of the ionizing stars, which remain relatively close to their (dusty) place of birth during their short lifetime, while the UV stellar continuum is contributed also by nonionizing stars, which have the time to move to regions of lower dust density. Hence, ionizing and nonionizing stars are not expected to be co-spatial, implying that a correlation is not expected between the stellar continuum and nebular emission, and thus between

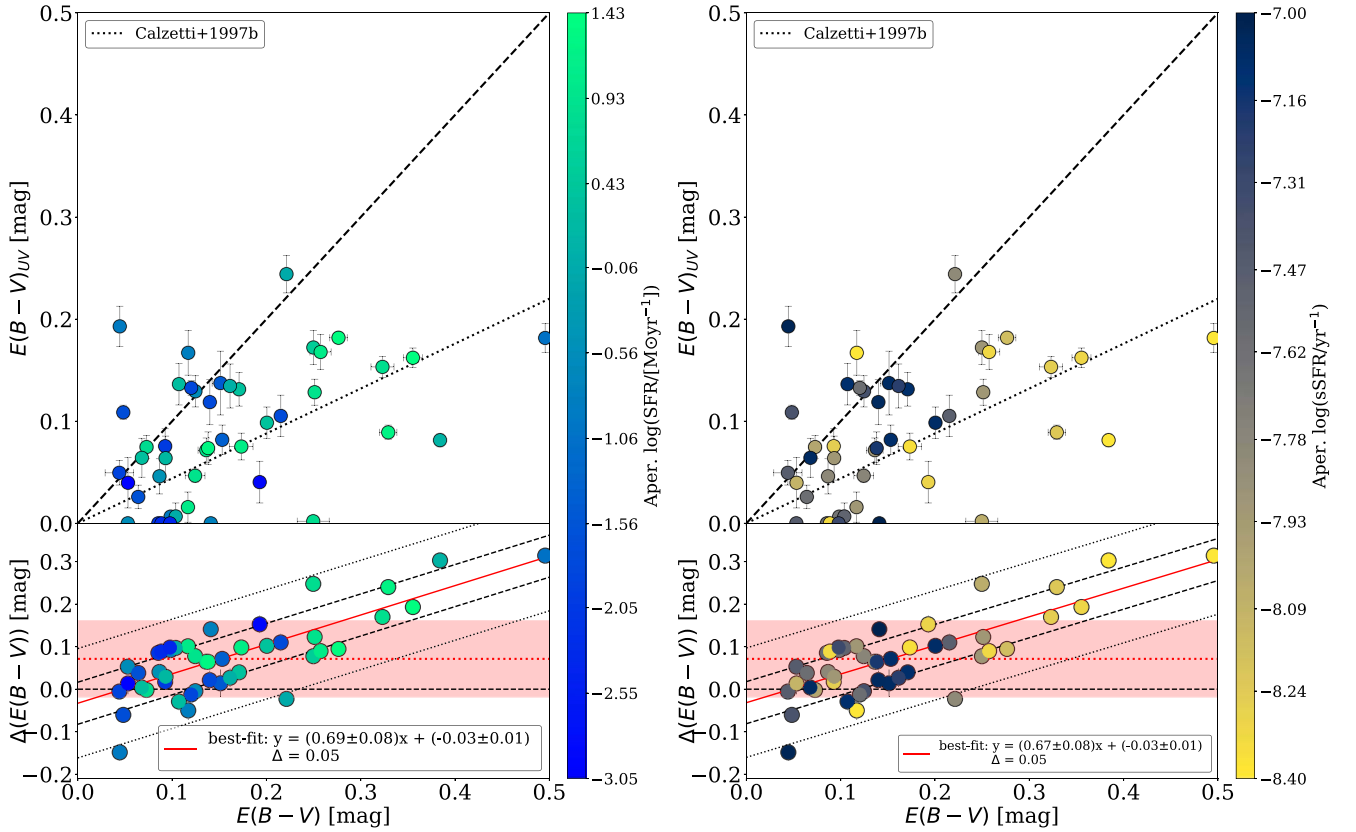


Figure 10. Upper panels: comparison between the stellar $E(B - V)_{UV}$ with respect to the gas $E(B - V)$, color coded as a function of $\log(\text{SFR})$ (on the left) and $\log(\text{sSFR})$ (on the right) within the COS aperture. The dashed black line represents the 1:1 relation, while the dotted line is the C97 empirical relation between the stellar and gas $E(B - V)$ (i.e., $E(B - V)_{UV} = (0.44 \pm 0.03) \times E(B - V)$). The uncertainties on the displayed quantities are shown in both axes. Lower panels: $\Delta(E(B - V))$ defined as $E(B - V) - E(B - V)_{UV}$. $\Delta(E(B - V))$ increases linearly with $E(B - V)$, and the linear best fit is indicated by the red solid lines, reported on the upper right, while the dashed and dotted lines represent the 1σ and 2.6σ around the best fit. The red horizontal dotted line represents the median $\Delta(E(B - V))$ while the shaded red region shows the 68% intrinsic scatter of the distribution. $\Delta(E(B - V))$ increases at increasing $\log(\text{SFR})$ and decreasing $\log(\text{sSFR})$. Overall, $E(B - V) \sim E(B - V)_{UV}$ at $\log(\text{SFR}/[M_{\odot} \text{yr}^{-1}]) \lesssim -1.5$ and $\log(\text{sSFR}/\text{yr}^{-1}) \gtrsim -8$, whereas at higher SFRs and lower sSFRs the stellar vs. gas $E(B - V)$ relation follows the C97 relation.

their reddening, in contrast with the empirical result found by C97. A possible interpretation to explain this differential attenuation is a two-component dust model, with diffuse dust attenuating light from all stars, and the birth cloud dust component only attenuating light originating from the star-forming regions (Wild et al. 2011a). In line with this interpretation, Wild et al. (2011a) found a dependence of this extra-attenuation on the sSFR. As nicely illustrated and explained in Figure 5 of Price et al. (2014), at high sSFRs the continuum light is dominated by young, massive stars located in the birth clouds, so both the continuum and emission lines are attenuated by both dust components, and the stellar and nebular $E(B - V)$ are similar; at decreasing sSFR, the discrepancy between the stellar and nebular $E(B - V)$ increases, as less massive stars, generally residing outside the birth clouds, have a higher contribution to the continuum emission, while the emission lines are still attenuated by both dust components. This is in line with what we find in Figure 10. An important thing to underline is that both Wild et al. (2011a) and Price et al. (2014) consider galaxies with $\log(\text{sSFR}/\text{yr}^{-1})$ in the range $\sim [-10, -8.5]$, while CLASSY galaxies are systematically shifted at higher $\log(\text{sSFR}/\text{yr}^{-1})$ in the range $\sim [-8.4, -7]$ (see Paper I). Indeed, CLASSY galaxies were selected to be compact and UV bright, and thus have significantly enhanced sSFRs with respect to their star-forming main-sequence counterparts at $z \sim 0$, and are more comparable to the $z \sim 2$ galaxy population of Paper I.

This could explain why we find no correlation of the sSFR with $E(B - V)_{UV}$ and just a mild anticorrelation with the gas $E(B - V)$ (Pearson factor of ~ -0.36) and with their difference (Pearson factor of ~ -0.40). Overall, we conclude that $E(B - V) \sim E(B - V)_{UV}$ at $\log(\text{SFR}/[M_{\odot} \text{yr}^{-1}]) \lesssim -1.5$ and $\log(\text{sSFR}/\text{yr}^{-1}) \gtrsim -8$, whereas at higher SFRs and lower sSFRs the stellar versus gas $E(B - V)$ relation follows that of C97. This relationship has the potential for us to derive the gas $E(B - V)$ in galaxies for which rest-frame UV spectra are available but the optical wavelengths are not accessible, as it will happen for the reionization galaxies that JWST will reveal.

6.2. UV Diagnostics for Electron Density

As shown in Section 5.2, the electron density estimated from $[\text{C III}] \lambda 1907 / [\text{C III}] \lambda 1909$ is overall ~ 2 dex higher than the one obtained from $[\text{S II}] \lambda 6717 / [\text{S II}] \lambda 6731$, despite the large errors on the C III] densities. Unfortunately, many previous works have been limited in determining the C III] densities by the low resolution of the spectra (e.g., Ravindranath et al. 2020). However, this discrepancy has also been found in a handful of cases at $z \sim 1 - 3$ where both the rest-frame optical and UV density diagnostics were available (Hainline et al. 2009; Quider et al. 2009; Christensen et al. 2012; Bayliss et al. 2014; James et al. 2014; Maseda et al. 2017; James et al. 2018; Berg et al. 2018; Acharyya et al. 2019; Schmidt et al. 2021) and

in few local galaxies as well (e.g., Berg et al. 2016). We also find a consistent offset between $n_e([\text{S II}])$ and the density values from $[\text{Si III}] \lambda 1883 / [\text{Si III}] \lambda 1892$ for the three galaxies for which it is available (i.e., J1044+0353, J1253-0312 and J1448-0110) and an even larger offset for the two galaxies with N IV densities (i.e., J1253-0312 and J1545+0858).

A possible reason for this UV–optical n_e discrepancy, as explained in Section 4, is that the optical [S II] is tracing the *low-ionization* regions while the UV doublets originate in *intermediate-ionization* and *high-ionization* regions, closer to the ionizing source (Maseda et al. 2017; Berg et al. 2018; James et al. 2018). Indeed, the ionization potential of these UV diagnostics (25–75 eV) and the range of densities for which they are n_e -sensitive (up to 10^5 cm^{-3}) reach higher values than [S II] doublet ($E \sim 10 - 20 \text{ eV}$ and $n_e < 10^4 \text{ cm}^{-3}$), as shown in the upper panels of Figure 3. In contrast to our findings, it should be noted that Patrício et al. (2016) measured consistent densities using the C III] and [O II] density diagnostics for a $z = 3.5$ star-forming galaxy, finding $n_e \sim 100 \text{ cm}^{-3}$, typical of local H II regions (Osterbrock 1989; Osterbrock & Ferland 2006). However, they did find higher values of n_e using the UV N IV] and Si III] diagnostics, suggesting that there must be other ISM properties that are playing a role.

As introduced in Section 4, a more self-consistent comparison between the UV and optical n_e diagnostics would be achieved by comparing the UV n_e diagnostics with the [C III] and [Ar IV] optical line ratios, which originate in the *intermediate-* and *high-ionization* regions, respectively. As shown in Figure 3, [C III] traces a slightly lower range of densities (with n_e up to $\sim 5 \times 10^4$), while [Ar IV] has a similar range to C III]. If the density structure were following the ionization structure, going from the diffuse to the densest gas, looking at the ionization potential of each density diagnostic tracer, the order would be: $n_e([\text{S II}]) < n_e([\text{O II}]) < n_e([\text{Fe III}]) < n_e([\text{Si III}]) < n_e([\text{C III}]) < n_e([\text{Ar IV}]) < n_e([\text{N IV}])$. This would be true assuming that nebulae are formed of uniform shells or rings, with density decreasing inside-out according to $1/r^2$ (Stanghellini & Kaler 1989). However, this density structure is not clearly confirmed by observations, with many works showing contradicting results. For instance, Maseda et al. (2017) found a consistent median density of $\log(n_e) \sim 3.2$ derived from C III] for a sample of 17 $z > 1.5$ C III]-emitting galaxies and densities obtained from [Ar IV] in a control sample of SDSS $z \sim 0$ objects. On the contrary, as detailed in Section 5.2, we found that in the optical, the [Ar IV] densities are consistent with [C III] values, with a median value $n_e \sim 10^3 \text{ cm}^{-3}$, whereas both are lower than the UV diagnostics by ~ 1 dex, despite the fact that [Ar IV] should trace a higher-ionization zone. UV densities are found to be consistent with [Fe III] densities (and [Fe III] has a lower ionization potential than [C III]), but these are just upper limits given the large error bars of the measured [Fe III] line ratios. Indeed, the relation between the ionization and density structure is not trivial, as the internal structure of H II regions is shaped both by winds and radiation pressure even when they are not dynamically important (see, e.g., Figure 2 of Geen et al. 2020). Also, the apertures of our UV and optical observations are not allowing us to observe singular H II regions, and because of the differential dust attenuation with the wavelength, the UV and optical tracers may not be tracing the same regions along the line of sight, with optical tracers coming also from regions completely extinguished in the UV.

A possible scenario that explains why $n_e([\text{Ar IV}])$ densities are not higher than $n_e([\text{C III}])$ would be an ionization front due to the central source that produces a rarefaction at the inner boundary of the nebula, and thus high-ionization zone density tracers such as [Ar IV] would be produced in a central hole (Giuliani 1981; Stanghellini & Kaler 1989). However, if this were the case, we should see a significant difference in the kinematics of [Ar IV] lines with respect to lower-ionization region density tracers (which we do not; M22). Hence, we cannot find evidence of a hydrodynamic effect at the basis of the density structure from our data. In this context, very-high-spectral-resolution optical data, especially integral-field spectroscopy data that allow us to map the density structure within a galaxy, could help understand this offset. An alternative explanation for the $n_e([\text{Ar IV}])$ – $n_e([\text{C III}])$ discrepancy could be related to the atomic parameters taken into account (Morisset et al. 2020; Juan de Dios & Rodríguez 2021). Indeed, PyNeb and Cloudy adopt different atomic data for the ions considered in this work, and in Figure 3, we showed that in general Cloudy predictions for densities were in agreement with PyNeb, apart from [Ar IV], for which Cloudy would predict densities up to ~ 1 dex higher. This corresponds to the discrepancy with the UV tracers that we find in this work.

To further investigate the relation between optical and UV densities, Figure 11 shows $n_e([\text{S II}])$ as a function of $n_e([\text{Si III}])$ (up-pointing triangles), $n_e([\text{C III}])$ (down-pointing triangles), and $n_e([\text{N IV}])$ (hexagons), color coded as a function of the EW(C III]). The dashed black line shows the 1:1 relation, while the dotted–dashed black line represents the 1:1 relation shifted by 2 dex, which we added to highlight the level of the offset. We tested several quantities, but a weak correlation was only observed between $\log(n_e([\text{S II}]) \lambda \lambda 6717, 31)$ and EW(C III]) (Pearson: $r \sim 0.40$, $p \sim 0.02$), which can be appreciated by the color coding of Figure 11. A slight increase in EW(C III]) with the density would be expected according to Jaskot & Ravindranath (2016) models. Indeed, the higher density nebula are characterized by a higher incident ionizing flux, because of the definition of the ionization parameter (see Equation (1) in Jaskot & Ravindranath 2016). Therefore, a higher density implies higher temperatures, as well as higher collision rates, which, in combination with the abundance of C^{2+} ions, ultimately determine the C III] emission strength (Jaskot & Ravindranath 2016). However, the strength of C III] emission is also affected by the gas-phase metallicity, the ionization parameter, or the stellar age, with increasing equivalent widths predicted to reach values $\gtrsim 10\text{--}15 \text{ \AA}$ at ages $< 3 \text{ Myr}$ and $\log(U) > -2$ (Jaskot & Ravindranath 2016; Nakajima et al. 2018; Ravindranath et al. 2020). In CLASSY galaxies, we find an anticorrelation between $\log(\text{EW}(\text{C III}]))$ and $12 + \log(\text{O}/\text{H})$ (Pearson: $r = -0.43$, $p = 0.03$), a slight correlation with $\log(U)$ (Pearson: $r = 0.3$, $p = 0.4$), and an anticorrelation with the stellar age (Pearson: $r = -0.4$, $p = 0.04$), confirming that the C III] strength of the emission is determined by many factors that are not yet fully understood (Ravindranath et al. 2020). We will comment more on the complex relation between C III], the metallicity, and the ionization parameter in Section 6.4.

Overall, the CLASSY galaxies show that $n_e([\text{C III}])$ is on average ~ 2 dex higher than $n_e([\text{S II}])$, and this offset can be used to determine the low-ionization zone electron density in similar galaxies if only the intermediate-ionization zone electron density is available from rest-frame UV spectra covering the C III] lines.

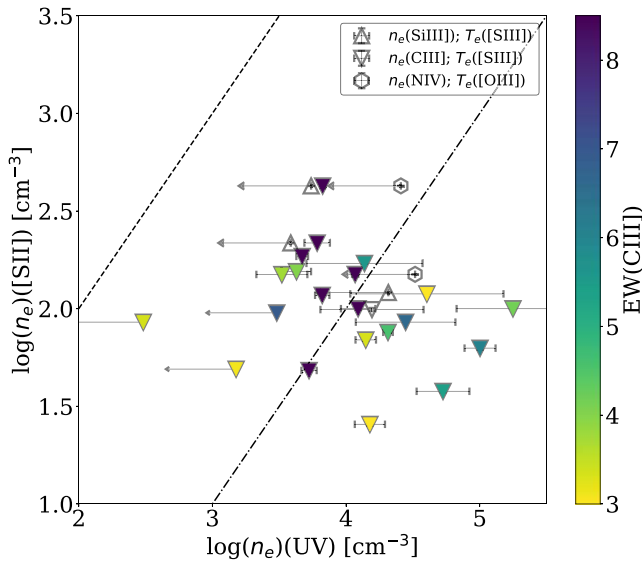


Figure 11. The $n_e([S II])$ in logarithm as a function of $n_e([Si III])$ (up-pointing triangles) and $n_e([N IV])$ (hexagons), as well as $n_e([C III])$ (down-pointing triangles), color coded as a function of $EW(C III)$. The uncertainties on the displayed quantities are shown in both axes. The black dotted–dashed line shows the 1:1 relation, while the dotted–dashed black line represents the same relation shifted by 2 dex, which we added to highlight the level of the offset.

6.3. UV Diagnostics for Electron Temperature

Here we have the important (and rare) opportunity to investigate if the hybrid UV–optical ratio $O III] \lambda 1666/\lambda 5007$ ($T_{e,hybrid}$) is a reliable tracer of T_e with respect to the most generally used optical ratio, $[O III] \lambda 4363/\lambda 5007$ ($T_{e,opt}$). In Section 5.3 we commented that the median difference in temperature between $T_{e,opt}$ and $T_{e,hybrid}$ is on average $\Delta \log(T_e)_{opt-hybrid} \sim -1000$ K, with higher values found for $T_{e,hybrid}$. This difference could be due to several factors. Indeed, it is not trivial to compare $O III] \lambda 1666$ and $[O III] \lambda 5007$, given that different instruments are used, with different apertures and calibration accuracies (see also Appendix A), as well as the large difference in wavelength, which can lead to higher uncertainties in the dust attenuation correction. Moreover, as commented in Section 4.3, in a patchy ISM, the UV light could be visible only through the less dense and/or less reddened regions along the line of sight, while the optical may trace also from denser and/or more reddened regions, leading to an intrinsic difference between the line ratios, and thus in the derived temperatures.

Another way to explain the discrepancy could be related to an effect of the gas pressure, as proposed by Nicholls et al. (2020). In their work, Nicholls et al. (2020) list this effect under the intrinsic caveats and limitations of the direct method to derive temperatures. Indeed, they commented that $[O III] \lambda 5007$ is quenched more rapidly than $[O III] \lambda 4363$ as the gas pressure increases, meaning that $[O III] \lambda 4363/\lambda 5007$ increases at increasing pressure, emulating a higher temperature as it happens in AGN (e.g., Nagao et al. 2001). This occurs because of $[O III] \lambda 4363$ has a significantly higher critical density than $[O III] \lambda 5007$ ($n_{crit} \sim 3.3 \times 10^7 \text{ cm}^{-3}$ versus $n_{crit} \sim 7.0 \times 10^5 \text{ cm}^{-3}$; Osterbrock 1989; Osterbrock & Ferland 2006). They specify that this effect can especially be a problem in unresolved high-luminosity H II regions. $O III] \lambda 1666$ has an even higher critical density ($n_{crit} \sim 4 \times 10^{10} \text{ cm}^{-3}$; Wei 1988) than $[O III] \lambda 4363$. Therefore, Nicholls et al. (2020) conclude that

higher values of $T_e(O III] \lambda 1666/[O III] \lambda 5007)$ compared to $T_e([O III] \lambda 4363/\lambda 5007)$ may be due to pressure bias, under suitable conditions of pressure and temperature.

All the factors discussed in the previous paragraphs could contribute to the median offset of ~ -1000 K between $T_{e,opt}$ and $T_{e,hybrid}$ that we observe. However, the fundamental aspect to understand is to what extent this offset impacts the estimate of $12+\log(O/H)$. We explore this in the top panels of Figure 12, where we compare the $12+\log(O/H)$ values that Paper I calculated using $n_e([S II])$ and $[O III] \lambda 4363/\lambda 5007$ (black pentagons), with the values we calculate using either $n_e([Ar IV])$ and $[O III] \lambda 4363/\lambda 5007$ ($T_{e,opt}$; dark green diamonds) or $n_e([S II])$, $n_e([Ar IV])$ and $O III] \lambda 1666/\lambda 5007$ ($T_{e,hybrid}$; gray pentagons and blue squares), as a function of the stellar mass. We also tested the combinations $n_e([N IV])$ and $[O III] \lambda 4363/\lambda 5007$ (green hexagons), or $n_e([N IV])$ and $O III] \lambda 1666/\lambda 5007$ (turquoise crosses). For clarity reasons, we display the optical $12+\log(O/H)$ on the left panels and the hybrid/UV $12+\log(O/H)$ on the right panels, showing as a reference the Paper I measurements. The lower panels of Figure 12 show the difference in dex between the various estimates and the values from Paper I. The dashed and dotted horizontal lines in the main and minor panels show the median values of the plotted quantities, respectively, while the shaded regions in the bottom panels represent the 68% intrinsic scatter of each distribution, color coded accordingly.

While there is an offset between $12+\log(O/H)$ from Paper I and the different estimates of $12+\log(O/H)$, it is mainly within ± 0.3 dex. In general, we find that this offset (the median value and its distribution, shown in the bottom panels of Figure 12) is consistent between the value derived using $T_{e,opt}$ and the one using $T_{e,hybrid}$, when measured with different density diagnostics. As commented in Section 4, if possible it is important to take the diagnostics of the same ionization zone into account because the lack of co-spatiality in estimating the ISM properties could lead to incorrect estimates of physical and chemical properties. Despite this fact, the method based on the $[S II]$ and the optical $[O III]$ ratios used in Paper I is the most common, even though $[S II]$ emission is not co-spatial with $[O III]$ emission (e.g., see Figure 4 from Nicholls et al. 2020). Using for instance $[Ar IV]$ or $[N IV]$ diagnostics to measure the density would be more ideal, but in practice these alternative optical density diagnostic lines are faint, and thus not available for all the CLASSY targets.

Overall, we conclude that the hybrid UV–optical temperature diagnostic, $T_{e,hybrid}$, is not dominated by potential systematic uncertainties and can be used as a reliable tracer of the electron temperature in the systems covered here. We also conclude that the hybrid UV–optical T_e allows to estimate the gas-phase metallicity with a scatter of ± 0.3 dex with respect to the optical $12+\log(O/H)$, again without showing systematic discrepancies. This is particularly important as in our sample we find that the $O III] \lambda 1666$ flux is on average ~ 0.3 dex brighter than the $[O III] \lambda 4363$, and thus it could be more easily observed in high- z galaxies than the weaker and less detectable $[O III] \lambda 4363$ emission.

While we have shown that $O III] \lambda 1666$ can allow us to reliably and directly estimate the metallicity of the ionized gas, the $T_{e,hybrid}$ method still depends on us having access to the optical $[O III] \lambda \lambda 4959, 5007$ emission. To the best of our knowledge the only work in the literature that proposed promising $12+\log(O/H)$ diagnostics using exclusively UV

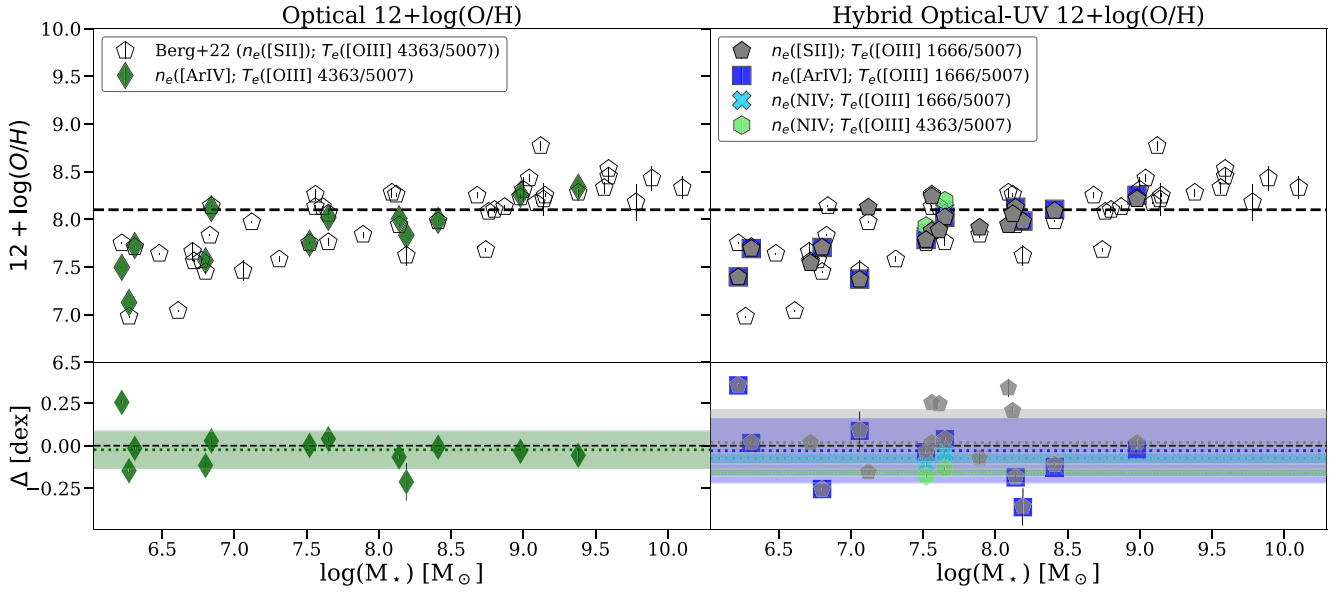


Figure 12. Top panels: comparison of $12+\log(\text{O}/\text{H})$ from Paper I, with the estimates obtained using the combination of with either $n_e([\text{Ar IV}])$ or $n_e([\text{N IV}])$, and either $T_e([\text{O III}]\lambda 4363/\lambda 5007)$ or $T_e([\text{O III}]\lambda 1666/\lambda 5007)$, as indicated in the legend, as a function of the stellar mass. For clarity reasons, the optical and hybrid optical–UV measurements of $12+\log(\text{O}/\text{H})$ are shown on the left and right, respectively, while $12+\log(\text{O}/\text{H})$ from Paper I is shown in both panels. The uncertainties on the displayed quantities are shown in both axes. Bottom panels: difference in dex between Paper I $12+\log(\text{O}/\text{H})$ and the other estimates, keeping the same symbols and colors as in the top panel.

emission lines is Byler et al. (2020; B20 hereafter). Using Cloudy modeling, these authors derived calibrations from $\text{He II}\lambda 1640/\text{C III}\lambda\lambda 1907,9$ versus $\text{O III}\lambda 1666/\text{C III}\lambda\lambda 1907,9$ (He2-O3C3 hereafter) and $\text{Si III}\lambda\lambda 1883,92/\text{C III}\lambda\lambda 1907,9$ versus $\text{O III}\lambda 1666/\text{C III}\lambda\lambda 1907,9$ (Si3-O3C3 hereafter). The typical statistical errors for these relations are ± 0.08 dex and ± 0.14 dex, respectively (Byler et al. 2020). In Figure 13, we compare the optical-based $12+\log(\text{O}/\text{H})$ values derived in Paper I with the values we derive here from the He2-O3C3 and Si3-O3C3 calibrations, shown as blue stars and magenta pluses, respectively. A clear disagreement can be seen between the $12+\log(\text{O}/\text{H})$ values derived from the UV diagnostics and optical direct method. The comparison with the 1:1 relation shows the difference between optical and UV $12+\log(\text{O}/\text{H})$. The Si3-O3C3 values are systematically higher with an offset of up to ~ 0.6 dex with respect to the optical $12+\log(\text{O}/\text{H})$ from Paper I, which decreases at increasing $12+\log(\text{O}/\text{H})$. However, we do not have enough Si III $\lambda\lambda 1883,92$ measurements to robustly evaluate the level of this trend. The He2-O3C3 estimates instead show a larger scatter of $\sim \pm 0.5$ dex, overpredicting the metallicity at $12+\log(\text{O}/\text{H}) < 8$, and underpredicting it at $12+\log(\text{O}/\text{H}) > 8$. This is in agreement with what was found by Rigby et al. (2021), who compared UV and optical $12+\log(\text{O}/\text{H})$ diagnostics for a single gravitationally lensed source, finding that the UV estimates from B20 are $\sim 0.50.8$ dex lower than the optical estimates, found in the range $12+\log(\text{O}/\text{H}) \sim 8.20 - 8.60$.

In order to investigate this offset further, we tested whether the optical and UV diagnostic $12+\log(\text{O}/\text{H})$ offset correlates with any optical or UV quantities that we measured here, or with CLASSY galaxy properties in general. We only found correlations with the optical $12+\log(\text{O}/\text{H})$, as it can be seen in Figure 13. The dotted–dashed blue and magenta best-fit relations in Figure 13 allow us to essentially recalibrate the B20 equations and to obtain the optical $12+\log(\text{O}/\text{H})$ from UV-only quantities, which we show in the following

expressions:

$$12 + \log(\text{O}/\text{H}) = (0.39 \pm 0.06) \times (12 + \log(\text{O}/\text{H}))_{\text{He2}} - (4.68 \pm 0.47), \quad (4)$$

$$12 + \log(\text{O}/\text{H}) = (0.42 \pm 0.20) \times (12 + \log(\text{O}/\text{H}))_{\text{Si3}} - (4.81 \pm 1.59), \quad (5)$$

with a scatter of 0.08 and 0.03 dex, respectively, while the dashed and dotted lines represent the 1σ and 2.6σ around the best fits.

6.4. UV Diagnostics for the Metallicity and Ionization Parameter

There have been many attempts to infer the gas-phase metallicity using a combination of photoionization models and UV emission lines (e.g., Fosbury et al. 2003; Chevallard & Charlot 2016; Feltre et al. 2016; Gutkin et al. 2016; Jaskot & Ravindranath 2016; Pérez-Montero & Amorín 2017; Byler et al. 2018; Nakajima et al. 2018) and/or measuring the metallicity directly with the UV O III] auroral line (e.g., Erb et al. 2010; Berg et al. 2018; James et al. 2018). However, few $12+\log(\text{O}/\text{H})$ calibrations have been proposed using exclusively UV emission lines (e.g., C IV $\lambda\lambda 1548,51$, He II $\lambda 1640$, O III] $\lambda 1666$, and C III] $\lambda\lambda 1907,9$; see Byler et al. 2020; Pérez-Montero & Amorín 2017), because UV lines are also strongly sensitive to other properties, such as the ionization parameter and shape of the ionizing continuum (Feltre et al. 2016; Gutkin et al. 2016; Nakajima et al. 2018; Maiolino & Mannucci 2019). The parameter space coverage of CLASSY and the high frequency of UV line detections throughout the sample allow us to explore how UV lines vary with the gas-phase metallicity $12+\log(\text{O}/\text{H})$ and ionization parameter, $\log(U)$, which we infer from reliable optical diagnostics.

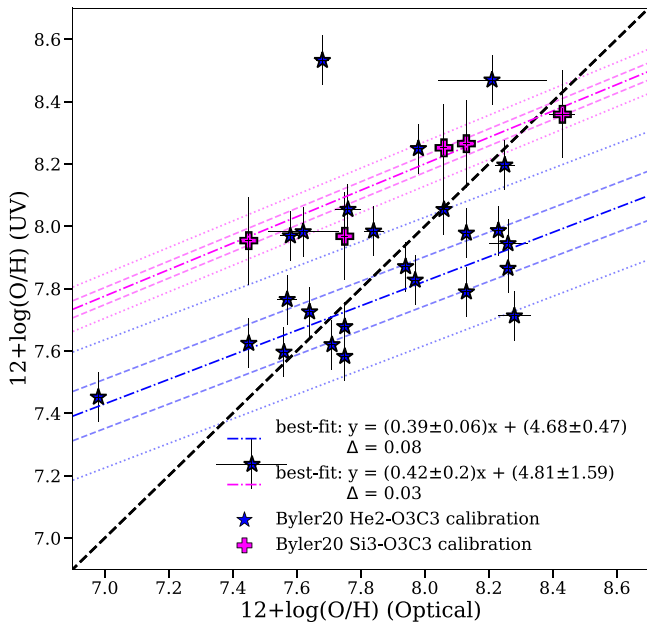


Figure 13. Comparison of optical and UV metallicities, comparing Paper I $12 + \log(\text{O}/\text{H})$ with the exclusively UV He2-O3C3 and Si3-O3C3 calibrations proposed by B20, shown as blue stars and magenta pluses. The uncertainties on the displayed quantities are shown in both axes. The dashed black line indicates the 1:1 relation. The dotted-dashed blue and magenta lines show the best fits of the $12 + \log(\text{O}/\text{H})_{\text{UV}}$ as a function of the optical $12 + \log(\text{O}/\text{H})$, as reported in the legend. The blue and magenta dashed and dotted lines represent the 1σ and 2.6σ around each best fit.

In order to fully explore the utility of UV diagnostic lines as possible tracers for these ISM properties, in this work we investigated a suite of derived quantities including: $\text{O III}] \lambda 1666 / \text{He II } \lambda 1640$; $\text{C III}] \lambda \lambda 1907,9 / \text{He II } \lambda 1640$; $\text{C III}] \lambda \lambda 1907,9 / \text{O III}] \lambda 1666$; $\text{C IV } \lambda \lambda 1548,51 / \text{C III}] \lambda \lambda 1907,9$; $\text{EW}(\text{He II } \lambda 1640)$; $\text{EW}(\text{O III}] \lambda 1666)$; $\text{EW}(\text{C III}] \lambda \lambda 1907,9)$; $\text{EW}(\text{C IV } \lambda \lambda 1548,51)$. Because after $\text{Ly}\alpha$, $\text{C III}] \lambda \lambda 1907,9$ and $\text{C IV } \lambda \lambda 1548,51$ are among the brightest UV emission lines in star-forming galaxies (e.g., Ravindranath et al. 2020), it is particularly useful, if possible, to exploit them to find reliable calibrations to infer the metallicity and ionization parameter for galaxies with properties comparable to those of the CLASSY sample.

In Figure 14 we show how these quantities vary as a function of $12 + \log(\text{O}/\text{H})$ (derived with the direct method, Paper I), color coded as a function of $\log(U)$ derived from O3O2 (top panel), and vice versa (bottom panel). In particular, we show only the measurements for which the S/N of the lines used to derive the quantities is higher than the chosen threshold ($\text{S}/\text{N} > 3$). In each panel we also provide the Pearson correlation factor and relative p value. Among these quantities, we find that $\log(\text{C III}] / \text{O III}]$, $\log(\text{EW}(\text{O III}])$, and $\log(\text{EW}(\text{C III}])$ show the most promising relation with $12 + \log(\text{O}/\text{H})$, with the highest Pearson factor found for $\text{C III}] / \text{O III}]$ (Pearson correlation factor ~ 0.68 and p value ~ 0.001). $\text{O III}] \lambda 1666 / \text{He II } \lambda 1640$ is clearly increasing as metallicity decreases with a turnover at $12 + \log(\text{O}/\text{H}) \sim 7.7$. We also notice that the presence of nebular C IV in pure emission can be used as well as a metallicity indicator, as it comes uniquely from $12 + \log(\text{O}/\text{H}) \lesssim 8$ (see also Senchyna et al. 2019; Berg et al. 2021; Schaerer et al. 2022; Senchyna et al. 2022). A slight anticorrelation between $\log(\text{C IV} / \text{C III}])$, $\log(\text{EW}(\text{C IV}))$, and $\log(\text{EW}(\text{He II}))$ with metallicity (Pearson: $r \sim -0.40$, $r \sim -0.35$ and $r \sim -0.20$, respectively) could be due instead to residuals

in the subtraction of stellar features, which would be most prominent at increasing metallicities.

In the left panel of Figure 15, we highlight the $\text{C III}] / \text{O III}]$ as a function of the $12 + \log(\text{O}/\text{H})$, color coded with respect to $\log(U)$. $\text{C III}] / \text{O III}]$ clearly increases at increasing metallicities, following the C/O abundance ratio (e.g., Garnett 1990; Izotov & Thuan 1999; Garnett et al. 2004; Erb et al. 2010; Guseva et al. 2011). Indeed, $\text{C III}] / \text{O III}]$ is considered a good tracer of C/O, because of the similar excitation and ionization potentials of C^{+2} and O^{+2} (i.e., 6–8 eV for excitation and 24.8–35.1 eV for ionization, respectively), and its minimal uncertainty due to reddening, given that the interstellar attenuation curve is nearly flat over the wavelength 1600–2000 Å (Garnett et al. 1995; Berg et al. 2016).

The metallicity dependence of C/O was also shown in Jaskot & Ravindranath (2016), who attribute it either to the weaker winds of low-metallicity massive stars or to the longer timescales to enrich the ISM for lower-mass stars (see also Maeder 1992; Henry et al. 2000; Chiappini et al. 2003). However, this relation is also characterized by a scatter that largely increases at low metallicities ($12 + \log(\text{O}/\text{H}) < 8$; see Figure 6(a) of Berg et al. (2016), Figure 3 of Amorín et al. (2017) or Figure 11 of Berg et al. (2019b)) because at low metallicity, C/O can be sensitive to different physical conditions, including SF histories, SF efficiency, inflow rates, and variations in the IMF (Skillman 1998; Berg et al. 2016; Amorín et al. 2017; Berg et al. 2019b). In agreement with Stark et al. (2014), and the predictions of Jaskot & Ravindranath (2016), $\text{C III}] / \text{O III}] > 1$ for all the CLASSY galaxies (the lowest value is $\text{C III}] / \text{O III}] \sim 1.70$ for J1323-0132). Jaskot & Ravindranath (2016) predict that $\text{C III}]$ should only become comparable to $\text{O III}]$ in photoionization models with metallicity of $Z < 0.004$, only if both C/O ratios are low ($\text{C}/\text{O} \leq 0.12$) and the ionization parameter is high ($\log(U) \geq -2$), which is consistent with the values of $12 + \log(\text{O}/\text{H})$ and $\log(U)$ we measure in this work.

The best-fit relation between $\text{C III}] / \text{O III}]$ and the direct-method metallicity $12 + \log(\text{O}/\text{H})$, shown as the red solid line in the left panel of Figure 15, is represented by:

$$12 + \log(\text{O}/\text{H}) = (0.80 \pm 0.26) \times \log(\text{C III}] 1907, 9 / \text{O III}] 1666) + (7.34 \pm 0.18) \quad (6)$$

with an intrinsic scatter of 0.18 dex. The dashed and dotted black lines indicate the 1σ and 2.6σ scatter from the relation, respectively. The scatter in this relation, which is expected as we commented in the previous paragraph, can also be partly explained by a secondary dependence to $\log(U)$, given the difference of the ionization potentials of the C and O lines (Jaskot & Ravindranath 2016). We will investigate in detail the behavior of $\text{C III}] / \text{O III}]$ with the C/O ratio and its scatter with respect to O/H in CLASSY in a forthcoming paper, focused on detailed photoionization modeling of the CLASSY galaxies.

The right panel of Figure 15 highlights the anticorrelation between $\text{EW}(\text{C III}])$ and $12 + \log(\text{O}/\text{H})$. Here we also include values found for local star-forming galaxies studied in recent works (Rigby et al. 2015; Berg et al. 2016; Senchyna et al. 2017, 2019; Berg et al. 2019a; Schaerer et al. 2022), in which $12 + \log(\text{O}/\text{H})$ was computed with the direct method, as in this work. As found by Rigby et al. (2015), Nakajima et al. (2018), and Ravindranath et al. (2020) low-metallicity galaxies tend to have a stronger $\text{EW}(\text{C III}])$, showing a linear anticorrelation

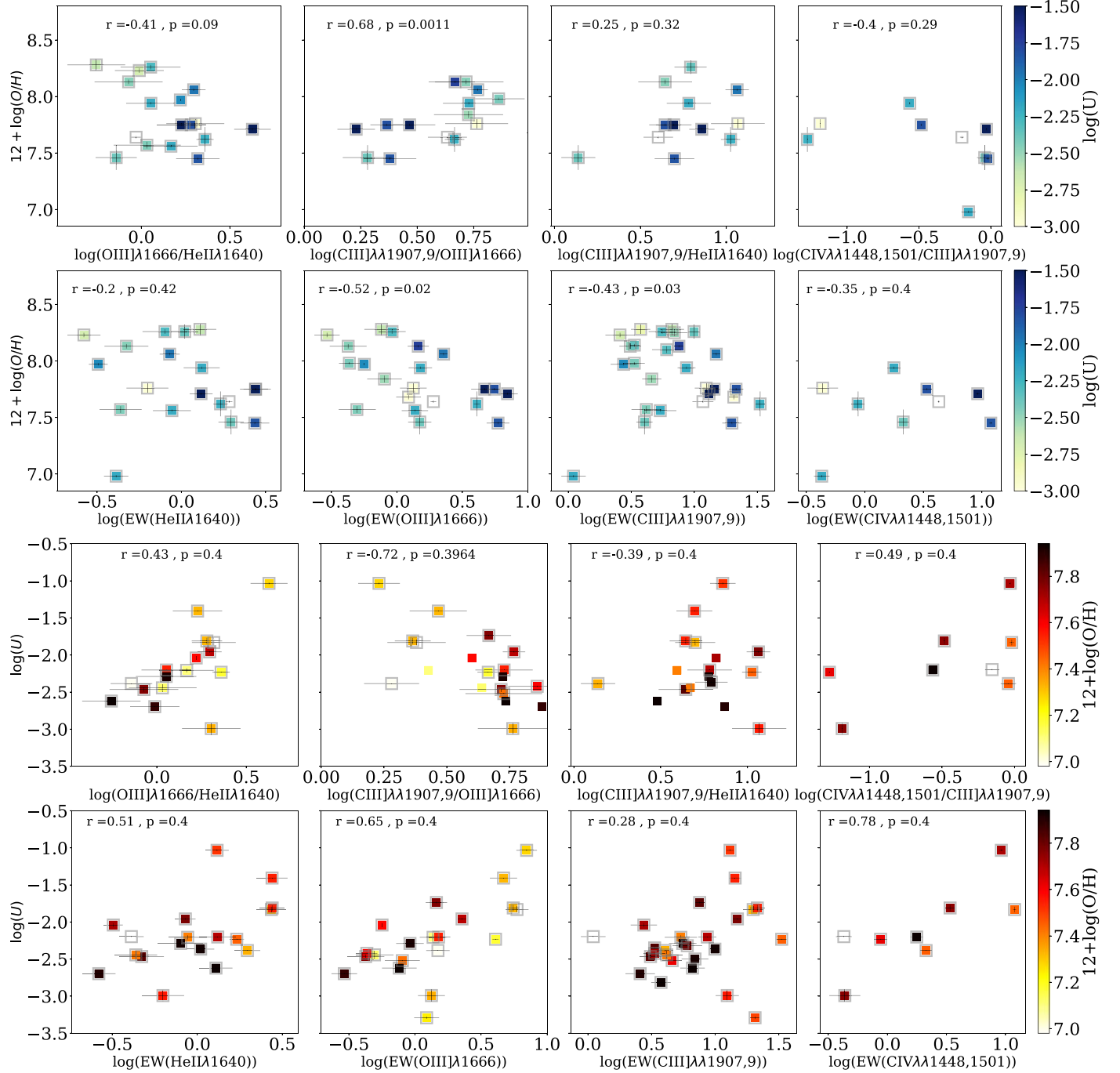


Figure 14. Top panel: $12 + \log(\text{O}/\text{H})$ as a function of the O III] $\lambda 1666/\text{He II } \lambda 1640$, C III]/O III] $\lambda 1666$, C III]/He II $\lambda 1640$, and C IV/C III] line ratios (upper panels), and EW(He II $\lambda 1640$), EW(O III] $\lambda 1666$), EW(C III]), and EW(C IV) (lower panels), color coded as a function of the ionization parameter $\log(U)$ derived from O3O2. The uncertainties on the displayed quantities are shown in both axes. All the quantities are in logarithm, and the Pearson factor and p value are shown in each panel. Overall the most promising relations are between C III]/[O III] $\lambda 1666$, $\text{EW}(\text{O III] } \lambda 1666) < 4 \text{ \AA}$ and $\text{EW}(\text{C III])}$ with $12 + \log(\text{O}/\text{H})$, but there is scatter in the plots, partly due to a degeneracy with the ionization parameter, as it can be appreciated from the color coding. Bottom panel: same for $\log(U)$, color coding as a function of $12 + \log(\text{O}/\text{H})$ from Paper I.

down to $\text{EW}(\text{C III])} > 5 \text{ \AA}$ for galaxies with $12 + \log(\text{O}/\text{H}) \lesssim 8.25$. A similar transition at $\text{EW}(\text{C III])} > 5 \text{ \AA}$ at $12 + \log(\text{O}/\text{H}) \lesssim 8.4$ is found and discussed in Senchyna et al. (2017, 2019). However, as shown in Figure 15, for galaxies with $\text{EW}(\text{C III])} < 5 \text{ \AA}$ there is clearly a large scatter toward lower metallicities, due to the fact that galaxies with $12 + \log(\text{O}/\text{H}) \lesssim 7.5$ can show $\text{EW}(\text{C III])} < 5 \text{ \AA}$ as well. As such, the $\text{EW}(\text{C III])}$ – $12 + \log(\text{O}/\text{H})$

relation is double-branched with a turnover point at $12 + \log(\text{O}/\text{H}) \sim 7.5$.

Indeed, as discussed in Jaskot & Ravindranath (2016), metallicity sets the shape of the ionizing SED and defines the nebular gas temperature, which enhances C III] emission at low metallicity due to the larger amount of ionizing photons and higher collisional excitation rates (e.g., Erb et al. 2010;

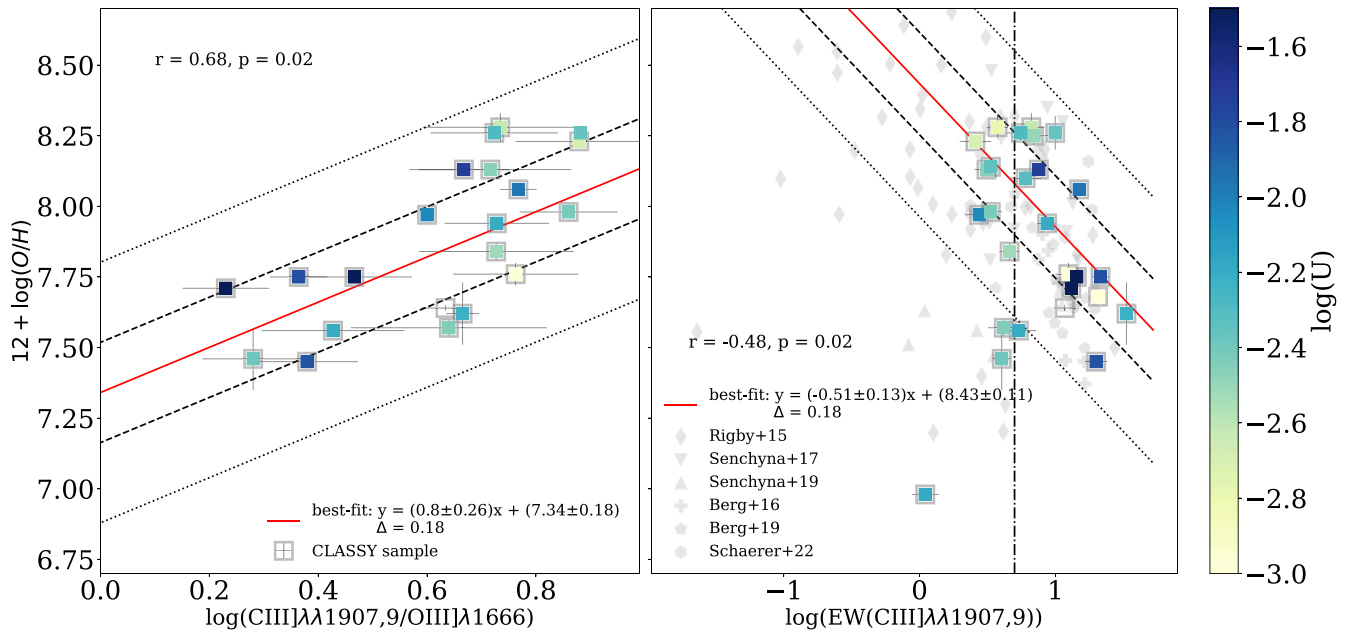


Figure 15. Gas-phase metallicity, $12 + \log(\text{O}/\text{H})$, as a function of $\text{C III]}/\text{O III] } \lambda 1666$ (left panel) and $\text{EW}(\text{C III]})$ (right panel), color coded as a function of $\log(U)$. The uncertainties on the displayed quantities are shown in both axes. Our best-fit linear relations are shown by the solid red lines, while the dashed and dotted black lines represent the 1σ and 2.6σ around the best fit. The scatter in both panels can be partly explained by a secondary dependence on the ionization parameter. In the right panel we also include values found for star-forming galaxies studied in recent works (Rigby et al. 2015; Berg et al. 2016; Senchyna et al. 2017, 2019; Berg et al. 2019a; Schaerer et al. 2022), in which $12 + \log(\text{O}/\text{H})$ was computed with the direct method, comparably to this work. This figure shows the most promising UV tracers of metallicity.

Stark et al. 2014). However, at these low metallicities, the carbon abundance decreases as well, suppressing C III] emission (e.g., Rigby et al. 2015). Moreover, as also discussed in Section 6.2, the strength of C III] emission is not only affected by metallicity, but also by the ionization parameter, stellar age, and gas density, with increasing equivalent widths predicted to reach values $\gtrsim 10\text{--}15 \text{ \AA}$ at ages $< 3 \text{ Myr}$ and $\log(U) > -2$ (Jaskot & Ravindranath 2016; Nakajima et al. 2018; Ravindranath et al. 2020). This explains why J0934+5514 (i.e., I Zw 18), characterized by the lowest metallicity among the CLASSY targets ($12 + \log(\text{O}/\text{H}) \sim 6.98$), has $\text{EW}(\text{C III])} \sim 1.10 \text{ \AA}$ despite a relative high ionization parameter ($\log(U) \sim -2.20$), as already acknowledged by Rigby et al. (2015).

Overall, the best-fit relation between $\log(\text{EW}(\text{C III]})\lambda\lambda 1907,9)$ and the direct-method metallicity, valid at $12 + \log(\text{O}/\text{H}) > 7.5$, is shown in the right panel of Figure 15 by the red solid line and is represented by:

$$12 + \log(\text{O}/\text{H}) = (-0.51 \pm 0.13) \times \log(\text{EW}(\text{C III]})\lambda\lambda 1907,9) + (8.43 \pm 0.11) \quad (7)$$

with an intrinsic scatter of 0.18 dex. The dashed and dotted black lines indicate the 1σ and 2.6σ scatter from the relation, respectively.

Returning to Figure 14, $\log(\text{C III]}/\text{O III])$, $\log(\text{C IV}/\text{C III])$, $\log(\text{EW}(\text{O III}))$, and $\log(\text{EW}(\text{C IV}))$ show the most promising relations with $\log(U)$, with the highest Pearson factors for $\text{EW}(\text{C IV})$ ($r \sim 0.78$). Overall, many of the shown quantities in Figure 14 show a dependence on both $12 + \log(\text{O}/\text{H})$ and $\log(U)$, as typically happens for UV tracers (e.g., Maiolino & Mannucci 2019; Ravindranath et al. 2020), with $\text{C III]}/\text{O III]}$ increasing with increasing $12 + \log(\text{O}/\text{H})$ and decreasing $\log(U)$, while $\text{EW}(\text{O III])}$ and $\text{EW}(\text{C III])}$ show the opposite

behavior. We further investigate the most promising correlations with ionization parameter in Figure 16, where we separate $\log(U)$ estimates for the low- (purple squares; from S3S2), intermediate- (green diamonds; from O3O2), and high-ionization regions (orange circles; from Ar4Ar3, as discussed in Section 5.4). The first three rows with three panels each show the relations of $\log(\text{C IV}/\text{C III])}$ (C4C3), and $\log(\text{C III]}/\text{O III])$, with S3S2, O3O2, and Ar4Ar3 $\log(U)$, respectively. The solid red lines show the best fit to each of the UV-based $\log(U)$ measurements from CLASSY, while the dashed and dotted lines represent the 1σ and 2.6σ around the best fit. The equations for the best-fit correlations and their intrinsic scatter are reported in the legend of each panel, alongside the corresponding Pearson factors. In general, the UV emission-line properties are more tightly correlated to O3O2 and Ar4Ar3 $\log(U)$, and only slightly or mostly not related to S3S2 $\log(U)$. This could be due to the fact that the three $\log(U)$ diagnostics are tracing different ionizing regions (see Section 4.4), and the considered UV lines are coming from intermediate- or high-ionization regions (Berg et al. 2021). Overall, the most promising UV-based diagnostics for $\log(U)$ are the following.

Using $\log(\text{C IV}/\text{C III])}$:

$$\log(U(\text{O3O2})) = (0.41 \pm 0.26) \times \log(\text{C4C3}) - (1.97 \pm 0.16), \quad (8)$$

$$\log(U(\text{Ar4Ar3})) = (0.36 \pm 0.2) \times \log(\text{C4C3}) - (1.33 \pm 0.11). \quad (9)$$

Using $\log(\text{EW}(\text{C IV}))$:

$$\log(U(\text{O3O2})) = (0.31 \pm 0.18) \times \log(\text{EW}(\text{C IV})1548, 51) - (2.2 \pm 0.1), \quad (10)$$

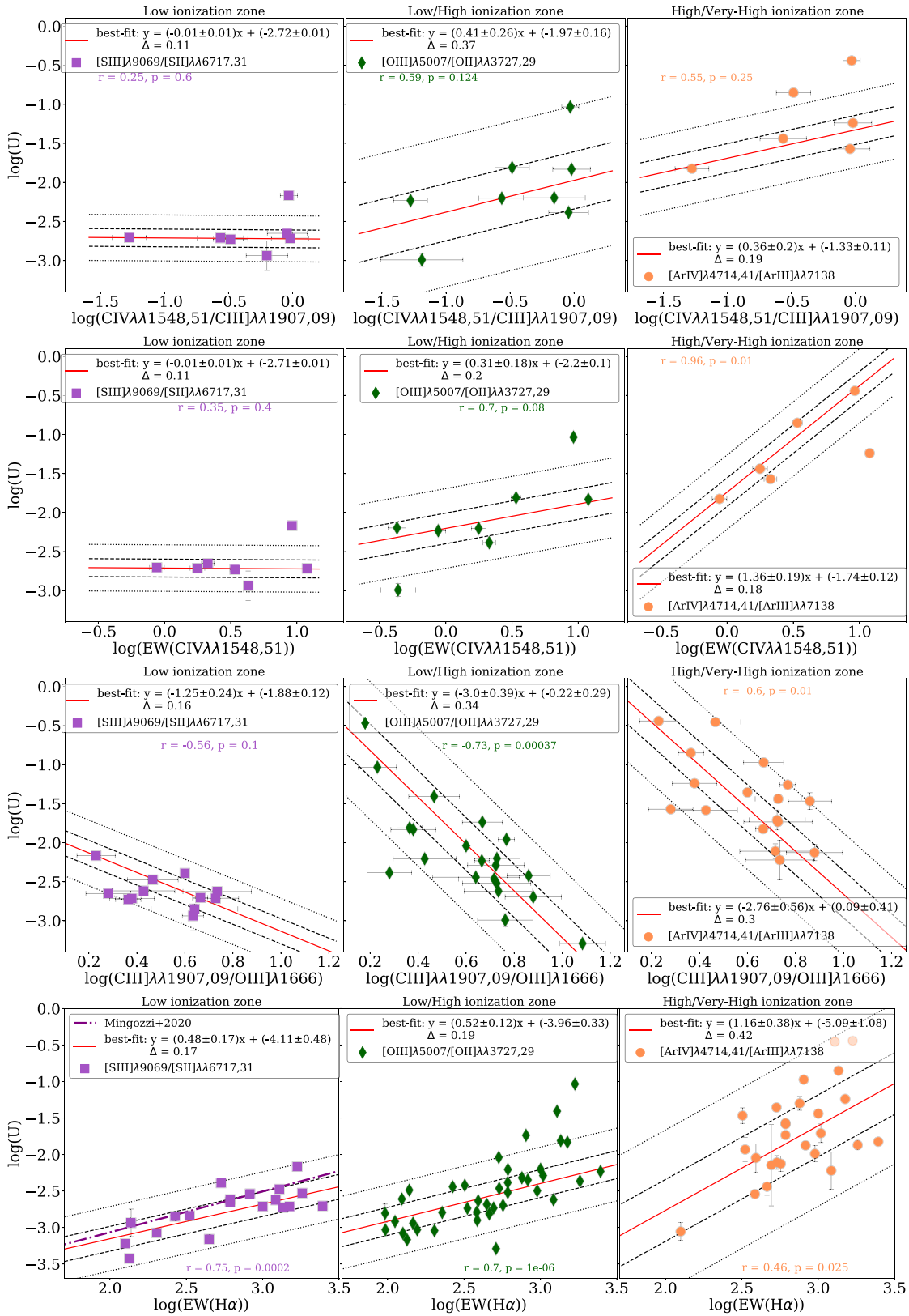


Figure 16. $\log(U)$ estimated for low- (purple squares; S3S2 line ratio), intermediate- (green diamonds; O3O2 line ratio), and high-ionization regions (orange circles; Ar4Ar3 line ratio) as a function of $\text{C IV } \lambda\lambda 1548,51/\text{C III } \lambda\lambda 1907,09$, $\log(\text{EW}(\text{C IV } \lambda\lambda 1548,51))$, $\text{C III } \lambda\lambda 1907,09/\text{O III } \lambda 1666$, and $\log(\text{EW}(\text{H}\alpha))$. The uncertainties on the displayed quantities are shown in both axes. The red solid lines represent the best fit that we calculated between the observables shown and the three $\log(U)$ values, while the dashed and dotted lines show the 1σ and 2.6σ scatter around the relation. The best-fit equations as well as the intrinsic scatter are reported in the legend in each panel. The dashed-dotted purple line in the bottom figure, left panel, is the correlation found by Mingozzi et al. (2020) between $\log(U)$ and $\log(\text{EW}(\text{H}\alpha))$. This figure shows the most promising UV tracers of $\log(U)$.

$$\log(U(\text{Ar4Ar3})) = (1.36 \pm 0.19) \times \log(\text{EW}(\text{CIV1548}, 51)) - (1.74 \pm 0.012). \quad (11)$$

Using $\log(\text{C III}/\text{O III})$:

$$\log(U(\text{S3S2})) = (-1.25 \pm 0.24) \times \log(\text{CIII}1907, 9/\text{OIII}1666) - (2.47 \pm 0.05), \quad (12)$$

$$\log(U(\text{O3O2})) = (-2.74 \pm 0.44) \times \log(\text{CIII}1907, 9/\text{OIII}1666) - (0.22 \pm 0.29), \quad (13)$$

$$\log(U(\text{Ar4Ar3})) = (-2.83 \pm 0.5) \times \log(\text{CIII}1907, 9/\text{OIII}1666) + (0.09 \pm 0.41). \quad (14)$$

In practice, Equations (8)–(14) in combination with Equations (6) and (7) for $12+\log(\text{O}/\text{H})$ (see Figure 15) could guide photoionization models to explore the relationship between $\log(U)$ and $12+\log(\text{O}/\text{H})$, with the hope of breaking its degeneracy.

6.4.1. A Note Regarding C IV

As a ratio of two UV emission lines from consecutive ionization states, C4C3, could trace the ionization structure of the nebula (Jaskot & Ravindranath 2016), similarly to S3S2, O3O2, and Ar4Ar3 in the optical. It is thought to be also a potential indicator of Lyman continuum (LyC) escape (Jaskot & Oey 2013; Nakajima & Ouchi 2014; Schaerer et al. 2022). Several authors have indeed proposed the use of C4C3 as a ionization parameter tracer (e.g., Pérez-Montero & Amorín 2017; Kewley et al. 2019; Schaerer et al. 2022). The first row of Figure 16 confirms a correlation between C4C3 and O3O2 and ArAr3 $\log(U)$, with a large intrinsic scatter, reported in the legend. Also EW(CIV) correlates well with $\log(U)$ derived from both O3O2 and Ar4Ar3, as shown in the second row of Figure 16.

We stress that the fitting method that we are using performs a clipping of the points out from 2.6σ of the relation (black dotted lines), which means that the best-fit equations that we find are not able to take all the available galaxies into account. This limitation is probably related to the low statistics, given that it is rare to observe pure nebular C IV emission, while the remaining galaxies showing pure absorption or P-Cygni profiles. Indeed, nebular C IV emission is rarely observed in the literature and comes uniquely from studies of systems with $12+\log(\text{O}/\text{H}) \lesssim 8$, indicative of a rapid hardening of the ionizing spectrum at low metallicities (see also Senchyna et al. 2019; Berg et al. 2021; Schaerer et al. 2022; Senchyna et al. 2022). This holds also for the galaxies of the CLASSY sample, where C IV nebular emission is coming only from objects with $12+\log(\text{O}/\text{H}) \lesssim 8$ and generally high ionization parameter $\log(U) \gtrsim -2.5$, as highlighted in Figure 16.

Senchyna et al. (2019) suggested also a correlation between EW(CIV) and EW(H β) (with galaxies characterized by C IV nebular emission having EW(H β) ≥ 100 Å). In turn, the equivalent width of the strongest hydrogen recombination lines measures the ratio of the young, ionizing stars over the old, nonionizing population (e.g., Leitherer 2005), and thus correlates with the sSFR and the degree to which the youngest stars dominate the optical (Kewley et al. 2015; Kaasinen et al. 2018;

Mingozzi et al. 2020). This partly explains the correlation between $\log(\text{EW}(\text{CIV}))$ and $\log(U)$. Indeed, Mingozzi et al. (2020) found a tight correlation between $\log(\text{EW}(\text{H}\alpha))$ and $\log(U)$ (derived from S3S2), explained in terms of the good correlation between $\log(U)$ and the age of the stellar population (Pellegrini et al. 2020), traced by EW(H α) (a similar correlation holds for EW(H β); e.g., Senchyna & Stark 2019). A comparable relation holds also for the CLASSY galaxies, as shown in the bottom panel of Figure 16, which displays the optical $\log(U)$ as a function of $\log(\text{EW}(\text{H}\alpha))$.

It should be noted, however, that diagnostics using nebular C IV emission may be difficult to employ due to strong stellar C IV P-Cygni profiles, as highlighted also in Jaskot & Ravindranath (2016). As commented in Section 3, CLASSY data benefits from a combination of relatively high S/N and high spectral resolution, which allowed us to separate the stellar and the nebular components of C IV emission via UV stellar-continuum modeling, but this may not always be the case—especially for high- z observations of faint galaxies. Another caveat to take into account for C4C3 is the different nature of C III] and C IV emission, while both are collisional nebular lines, C IV is also a resonant line affected by radiation transfer effects. This means that C IV absorption along the line of sight, which depends on the gas kinematics and column density, could contribute in reducing the observed C IV emission (e.g., Steidel et al. 2016). We will investigate in detail any differences in the kinematics of these lines and the causes that contribute to their emission in M22 (in preparation), which is dedicated to the ionization mechanisms behind the UV emission lines presented here.

7. Conclusions

In this work we investigated UV and optical diagnostics of the ISM properties by exploiting the CLASSY survey presented by Berg et al. (2022) and James et al. (2022), which represents the first high-quality, high-resolution, and broad-wavelength-range ($\sim 1200\text{--}2000$ Å) FUV spectral database of 45 nearby ($0.002 < z < 0.182$) star-forming galaxies. Specifically we focused on the main UV emission lines visible in the COS spectra apart from Ly α (i.e., N IV] $\lambda\lambda$ 1483,87, C IV $\lambda\lambda$ 1548,51, He II λ 1640, O III] $\lambda\lambda$ 1661,6, Si III] $\lambda\lambda$ 1883,92, C III] $\lambda\lambda$ 1907,9), and combine them with emission lines comprised between [O II] $\lambda\lambda$ 3727,9 and [S III] λ 9069 from optical spectroscopy of the same pointing. Our aim was to provide a *UV toolkit* of ISM diagnostics, i.e., a set of equations to diagnose $E(B-V)$, n_e , T_e , $12+\log(\text{O}/\text{H})$, and $\log(U)$, that use only UV emission lines. By carefully assessing the stratified ionization structure of our targets, we accurately calculated the physical and chemical properties using diagnostic line ratios specific to each ionization zone (constituting a set of “direct” diagnostics), then subsequently comparing and calibrating each property with the well-known optical diagnostics to derive a series of “indirect” diagnostic UV-based equations. In the following we summarize our main findings.

1. UV density diagnostics ([C III] λ 1907/C III] λ 1909, [Si III] λ 1883/Si III] λ 1892, N IV] λ 1483/N IV] λ 1487) give $\log(n_e) \sim 2$ dex higher than the optical counterparts [S II] λ 6717/[S II] λ 6731 and [O II] λ 3729/ λ 3727 and ~ 1 dex than [Cl III] λ 5518/ λ 5538 and [Ar IV] λ 4714/ λ 4741, as summarized in Figure 6 and discussed in Section 6.2. UV n_e values are consistent with $n_e([\text{Fe III}] \lambda 4701/\lambda 4659)$, for which we can derive only

- upper limits. The UV-to-optical electron density offset enables us to derive a low-ionization zone n_e (e.g., $n_e([\text{S II}])$) for high- z targets in case optical wavelengths are not available.
2. The hybrid UV–optical temperature diagnostic $\text{O III}] \lambda 1666/\lambda 5007$ is not dominated by major systematic uncertainties, as shown in Figure 8. As such, we find this auroral line ratio to be as reliable a tracer of electron temperature as the most generally used optical ratio, $[\text{O III}] \lambda 4363/\lambda 5007$. We also find that the $\text{O III}] \lambda 1666$ flux is on average ~ 0.3 dex brighter than the $[\text{O III}] \lambda 4363$, and thus it could be more easily observed in high- z galaxies than the weaker and less detectable $[\text{O III}] \lambda 4363$ emission.
 3. On average, $\text{O III}] \lambda 1666/\lambda 5007$ gives temperatures higher than $[\text{O III}] \lambda 4363/\lambda 5007$ by ~ 1000 K. Despite this offset, we discuss in Section 6.3 that $T_e(\text{O III}] \lambda 1666/\lambda 5007)$ allows us to estimate direct-method gas-phase metallicities with only a scatter of ± 0.3 dex with respect to the optically derived $12+\log(\text{O}/\text{H})$, as shown in Figure 12. We also investigated how the optical $12+\log(\text{O}/\text{H})$ compare with metallicities derived from UV-based He2-O3C3 and Si3-O3C3 metallicity calibrations by B20 (see Figure 13). We find an offset correlating with the optical $12+\log(\text{O}/\text{H})$, and we provide expressions to recalibrate the B20 equations (i.e., Equations (4) and (5)).
 4. We derive ionization parameters in the range $-3.5 < \log(U) < 0$, using the optical diagnostics S3S2 ($[\text{S III}] \lambda \lambda 9069, 9532/[\text{S II}] \lambda \lambda 6717, 31$), O3O2 ($[\text{O III}] \lambda 5007/[\text{O II}] \lambda \lambda 3727, 29$), and Ar4Ar3 ($[\text{Ar IV}] \lambda \lambda 4714, 71/[\text{Ar III}] \lambda 7138$), as shown in Figure 9. Specifically, we find that $\log(U(\text{S3S2})) < \log(U(\text{O3O2})) < \log(U(\text{Ar4Ar3}))$, in line with the presence of a clear ionization structure in the nebular environments of our targets, as described in Section 4 and in Berg et al. (2021).
 5. In Figure 10, we investigated how the gas attenuation, $E(B-V)$ (obtained with the Balmer decrement and the Cardelli et al. 1989 attenuation law; see Section 4.1), compares with the stellar attenuation, $E(B-V)_{\text{UV}}$ (obtained from the β slope of stellar-continuum fitting and the Reddy et al. 2016 attenuation law; see Section 3.1.1). Our conclusion is that the gas and stellar attenuation factors are approximately the same at $\log(\text{sSFR}) \gtrsim -8 \text{ yr}^{-1}$, whereas at lower sSFRs the values tend toward the C97 relation, $E(B-V) \sim 2.27 \times E(B-V)_{\text{UV}}$. This relation subsequently allows us to use $E(B-V)_{\text{UV}}$ to derive $E(B-V)$ in galaxies if optical wavelengths are not accessible.
 6. Possible UV diagnostics for $12+\log(\text{O}/\text{H})$ and $\log(U)$ were explored in Section 6.4 and Figure 14, where we also confirm that UV lines are usually sensitive to both parameters. We proposed $\text{C III}] \lambda \lambda 1907, 9/\text{O III}] \lambda 1666$ and $\text{EW}(\text{C III}] \lambda \lambda 1907, 9)$ as $12+\log(\text{O}/\text{H})$ diagnostics (see Equations (6) and (7), displayed in Figure 15). We also highlight that the presence of nebular C IV $\lambda 1548, 51$ can be used as a metallicity indicator, as is revealed uniquely in galaxies with $12+\log(\text{O}/\text{H}) \lesssim 8$, in agreement with the few previous works that studied this rare spectral feature. In Figure 16, we include the most promising $\log(U)$ diagnostics, providing expressions to derive the ionization parameter from C IV $\lambda \lambda 1548, 51/\text{C III}] \lambda \lambda 1907, 9$, $\text{EW}(\text{C IV } \lambda \lambda 1548, 51)$, and

$\text{C III}] \lambda \lambda 1907, 9/\text{O III}] \lambda 1666$ (see Equations (8)–(14)). Finally, in Section 6.4.1, we discuss the limitations of using nebular C IV diagnostics.

In summary, we present an empirically calibrated *UV toolkit* of ISM diagnostics that will be fundamental in characterizing and interpreting the spectroscopic observations of high- z systems in the upcoming JWST and ELT era, for which the optical wavelength range will not be available. Specifically, NIRISS and NIRSpec JWST instruments can provide spectra in the wavelength ranges of 0.8–2.2 and 0.6–5.3 μm , respectively, covering (in full or in part) the suite of optical emission lines (from $[\text{O II}] \lambda \lambda 3727$ to $\text{H}\alpha$) together with the $\text{C III}] \lambda \lambda 1907, 9$ at $5 < z < 6$ (e.g., Curti et al. 2022; Lin et al. 2022). At higher z , optical lines are progressively shifted out of the observed range, while at $z \geq 10$ only UV lines from $\text{Ly}\alpha$ to $\text{C III}]$ will be accessible. The low-resolution ($R \sim 150$) spectroscopy of JWST/NIRISS is not enough to resolve the $\text{C III}]$ doublet, but is expected to detect the UV emission lines down to $\sim 10^{-18} \text{ erg/s/cm}^2$ (Treu et al. 2022; JWST User Documentation 2016). On the other hand, the higher spectral resolution of JWST/NIRSpec (up to $R \sim 2700$) will provide a resolved $\text{C III}]$ doublet (JWST User Documentation 2016). As demonstrated here, the CLASSY survey has provided the ideal ATLAS to create a powerful UV toolkit to explore these high- z spectra in terms of sSFR, direct gas-phase metallicity, ionization level, reddening, and nebular density, as it represents a high-quality UV and optical database for local analogs to reionization-era systems. To complete our toolkit, in the next paper on UV-based diagnostics, we will focus on the ionized gas kinematics, both of UV and optical emission, and on the diagnostics to inspect their main ionization mechanisms, to also understand the origin of the main UV emission lines taken into account.

We thank the anonymous referee for their comments and advice, which helped improve the quality of the paper. M.M., D.A.B., and X.X. are grateful for the support for this program, HST-GO-15840, that was provided by NASA through a grant from the Space Telescope Science Institute, which is operated by the Associations of Universities for Research in Astronomy, Incorporated, under NASA contract NAS5-26555. Also, M.M. is grateful to Carlo Cannarozzo for inspiring conversations and advice. B.L.J., S.H., and N.K. are thankful for support from the European Space Agency (ESA). A.F. acknowledges the support from grant PRIN MIUR2017-20173ML3WW_001. A.W. acknowledges the support of UNAM via grant agreement PAPIIT no. IN106922. R.A. acknowledges support from ANID Fondecyt Regular 1202007.

The CLASSY collaboration extends special gratitude to the Lorentz Center for useful discussions during the “Characterizing Galaxies with Spectroscopy with a view for JWST” 2017 workshop that led to the formation of the CLASSY collaboration and survey. The CLASSY collaboration thanks the COS team for all their assistance and advice in the reduction of the COS data.

Funding for SDSS-III has been provided by the Alfred P. Sloan Foundation, the Participating Institutions, the National Science Foundation, and the U.S. Department of Energy Office of Science. The SDSS-III website is <http://www.sdss3.org/>. SDSS-III is managed by the Astrophysical Research Consortium for the Participating Institutions of the SDSS-III Collaboration including the University of Arizona, the Brazilian Participation Group, Brookhaven National Laboratory,

Carnegie Mellon University, University of Florida, the French Participation Group, the German Participation Group, Harvard University, the Instituto de Astrofísica de Canarias, the Michigan State/Notre Dame/JINA Participation Group, Johns Hopkins University, Lawrence Berkeley National Laboratory, Max Planck Institute for Astrophysics, Max Planck Institute for Extraterrestrial Physics, New Mexico State University, New York University, Ohio State University, Pennsylvania State University, University of Portsmouth, Princeton University, the Spanish Participation Group, University of Tokyo, University of Utah, Vanderbilt University, University of Virginia, University of Washington, and Yale University.

This work also uses the services of the ESO Science Archive Facility, observations collected at the European Southern Observatory under ESO programs 096.B-0690, 0103.B-0531, 0103.D-0705, and 0104.D-0503, and observations obtained with the Large Binocular Telescope (LBT). The LBT is an international collaboration among institutions in the United States, Italy, and Germany. LBT Corporation partners are: The University of Arizona on behalf of the Arizona Board of Regents; Istituto Nazionale di Astrofisica, Italy; LBT Beteiligungsgesellschaft, Germany, representing the Max-Planck Society, The Leibniz Institute for Astrophysics Potsdam, and Heidelberg University; The Ohio State University, University of Notre Dame, University of Minnesota, and University of Virginia.

This research has made use of the HSLA database, developed and maintained at STScI, Baltimore, USA.

Facilities: HST (COS), LBT (MODS), APO (SDSS), KECK (ESI), VLT (MUSE, VIMOS).

Software: astropy (Astropy Collaboration 2013, 2018) BEAGLE (Chevallard & Charlot 2016), CalCOS (STScI), dustmaps (Green 2018), jupyter (Kluyver et al. 2016), LINMIX (Kelly 2007) MPFIT (Markwardt 2009), MODS reduction Pipeline, Photutils (Bradley et al. 2021), PYNEB (Luridiana et al. 2012, 2015), python, pysynphot (STScI Development Team 2013), RASCAS (Michel-Dansac et al. 2020), SALT (Scarlata & Panagia 2015), STARLIGHT (Fernandes et al. 2005b), TLAC (Gronke & Dijkstra 2014), XIDL.

Appendix A UV–Optical Flux Offset

Before comparing COS and optical data, it was necessary to check and correct optical spectra for potential UV–optical flux offsets. Below we explain in detail the procedure we carried out to check if there is alignment between the continuum flux of the two wavelength regimes. Such an offset is expected as the UV and optical spectra have been obtained via different instruments and different apertures. Specifically, we have to take into account: (i) the different aperture size of COS ($2''.5$), SDSS ($3''$), MMT ($10'' \times 1''$ slit) and LBT ($2''.5 \times 1''$ slit), while the MUSE, VIMOS and KCWI data were extracted using an aperture of $2''.5$, identical to COS; (ii) a possible different orientation of the COS and SDSS apertures, and MMT and LBT slits, for extended sources and/or targets with multi-component light profiles throughout the aperture; (iii) COS vignetting of noncompact objects; (iv) flux calibration issues specific to the instrument. Having said that, we stress that this is an issue *only* for mixed UV–optical diagnostics, such as the O III] $\lambda 1666/\lambda 5007$ line ratio, that can be used to measure the electron temperature of the gas (see Sections 4.3, 5.3 and 6.3). Indeed, Paper V analyzed the optical data of 12 CLASSY

galaxies taking into account SDSS, VLT/MUSE, and, for a subsample, LBT/MODS and Keck/ESI long-slit spectra, to assess the impact of using different aperture combinations on the determination of the ISM physical conditions (i.e., n_e , T_e , $E(B - V)$, $\log(U)$ and $12 + \log(O/H)$). Overall, Paper V found that these measurements remained roughly constant with aperture size, indicating that the optical gas conditions are relatively uniform for this sample.

To explore the UV–optical flux offset, we extended the UV stellar-continuum best fit performed in the range 1200–2000 Å with the method from S22 and C&B models as described in Section 3.1.1, to optical wavelengths up to ~ 9000 Å, taking a SMC attenuation law (Gordon et al. 2003) into account. Here we stress that the choice of the attenuation law is not affecting the results in the optical wavelength range, as the different known attenuation laws (e.g., Cardelli et al. 1989; Calzetti et al. 2000; Gordon et al. 2003) are all superimposed at $\lambda \gtrsim 3800$ Å (e.g., see Figure 3 in Shivaei et al. 2020). This is not the case in the UV wavelength range, where we adopted the most suitable Reddy et al. (2016) attenuation law, as discussed in Sections 3.1.1 and 4.1. The performed extrapolation of the UV stellar-continuum best fit toward the optical wavelengths allows us to perform a direct comparison with the optical spectrum fitted with Starlight as described in Section 3.1.2, by providing an overlapping wavelength window. This is illustrated in Figure 17, which shows the observed COS (black solid line) and optical SDSS and MUSE (gray and black dotted line, respectively) spectra for the CLASSY galaxies J0021+0052 and J1144+4012. Overlaid are the extended-UV stellar-continuum best fit (dashed blue line) and the optical stellar-continuum best fit (dashed red and magenta line for SDSS and MUSE spectra, respectively). The UV–optical flux offset is then estimated by dividing the extended-UV stellar-continuum fit by the optical stellar-continuum best fit in eight featureless wavelength windows (40 Å each in width) between 3700 and 5600 Å (highlighted in cyan), avoiding the region of the 4000 Å break, and calculating their median value and using the standard deviation as the corresponding error. The final optical spectra, corrected for the UV–optical flux offset, are shown by the green and orange solid lines for SDSS and MUSE, respectively.

The left panel of Figure 18 shows the UV–optical flux offsets measured throughout the CLASSY sample, using different symbols to indicate the SDSS, MUSE, LBT, KCWI, VIMOS, and MMT observations, as reported in the legend. An important aspect to explore is that there is no dependence of the UV–optical flux offset we measure with the galaxy extent, which for some targets can be larger than that covered by the COS and optical apertures that we are taking into account. In these cases, COS is not measuring the entire flux for these objects. For instance, under the hypothesis that the sources were filling uniformly the COS and SDSS apertures centered in the same position, the optical fluxes should be scaled by the ratio of their apertures ($(2''.5/3''.0)^2$ (i.e., dashed magenta line). The dashed-dotted blue line in Figure 18 represents the median value of the SDSS UV–optical offset, considering the 24 galaxies with an average half-light radius (r_{50}) larger than the optical extent, calculated by plotting the fraction of the optical flux from Pan-STARRS imaging (taken from Table 6 in Paper I and reported in Table 1). This value is close to the magenta line, but offsets obtained for the SDSS galaxies (blue dots) are spread in the range ~ 0.5 – 1.3 , demonstrating that there are other factors at

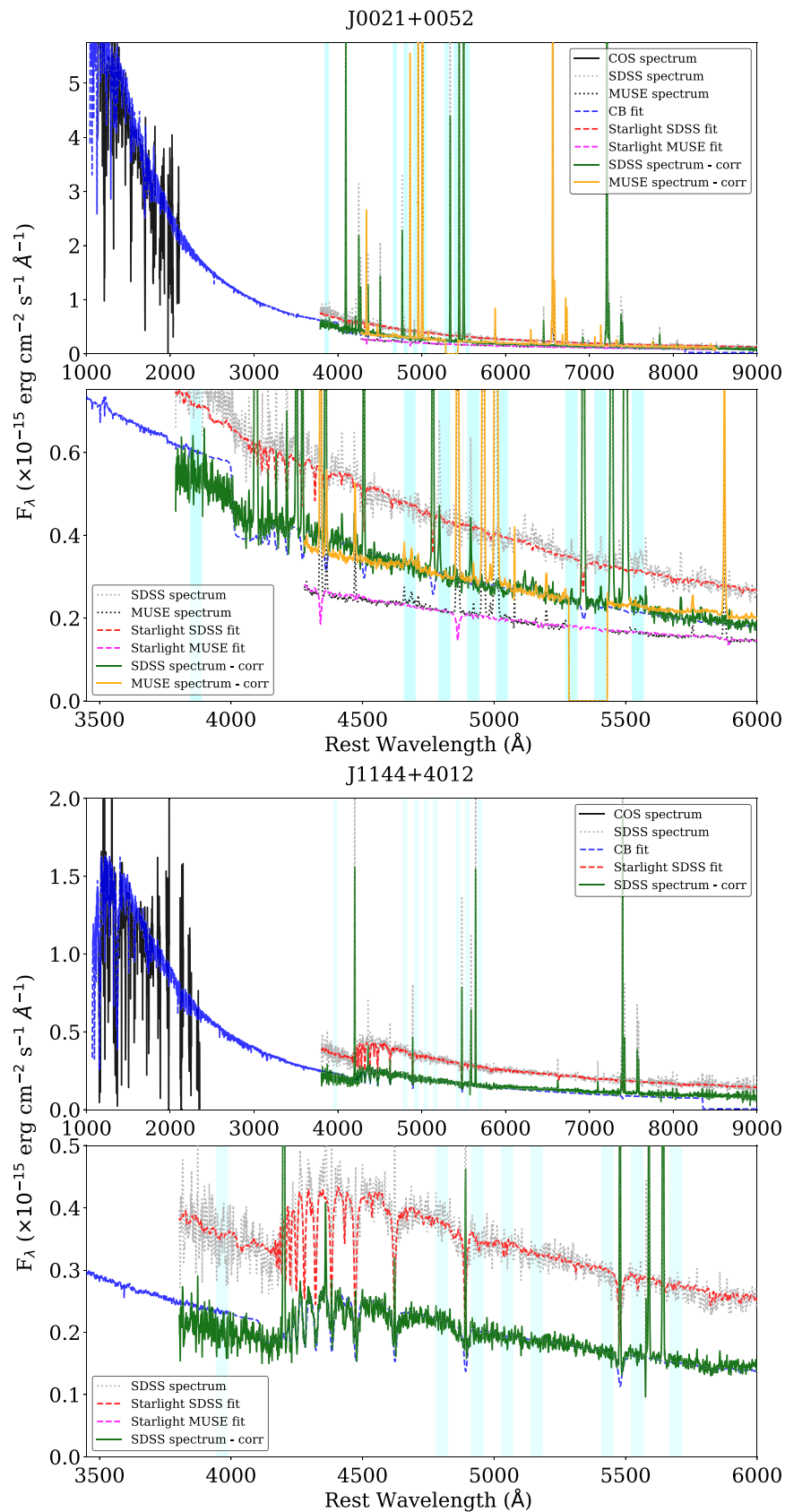


Figure 17. Upper panels: COS, SDSS, and MUSE spectra of galaxy J0021+0052. The COS spectrum is shown with a black solid line, while the original SDSS and MUSE optical spectra with a dotted gray and black line, respectively. The UV–optical flux offset is estimated comparing the UV–extended stellar–continuum fitting (dashed blue line) and optical stellar–continuum fitting (dashed red line for SDSS and magenta for MUSE) in several featureless wavelength ranges of 40 Å between 4000 and 5600 Å, highlighted in cyan. The UV–optical flux offset corrected spectra are shown from the green and orange solid lines, for SDSS and MUSE, respectively. The bottom panel shows a zoom on the optical region of the spectra. Lower panels: same for galaxy J1144+4012.

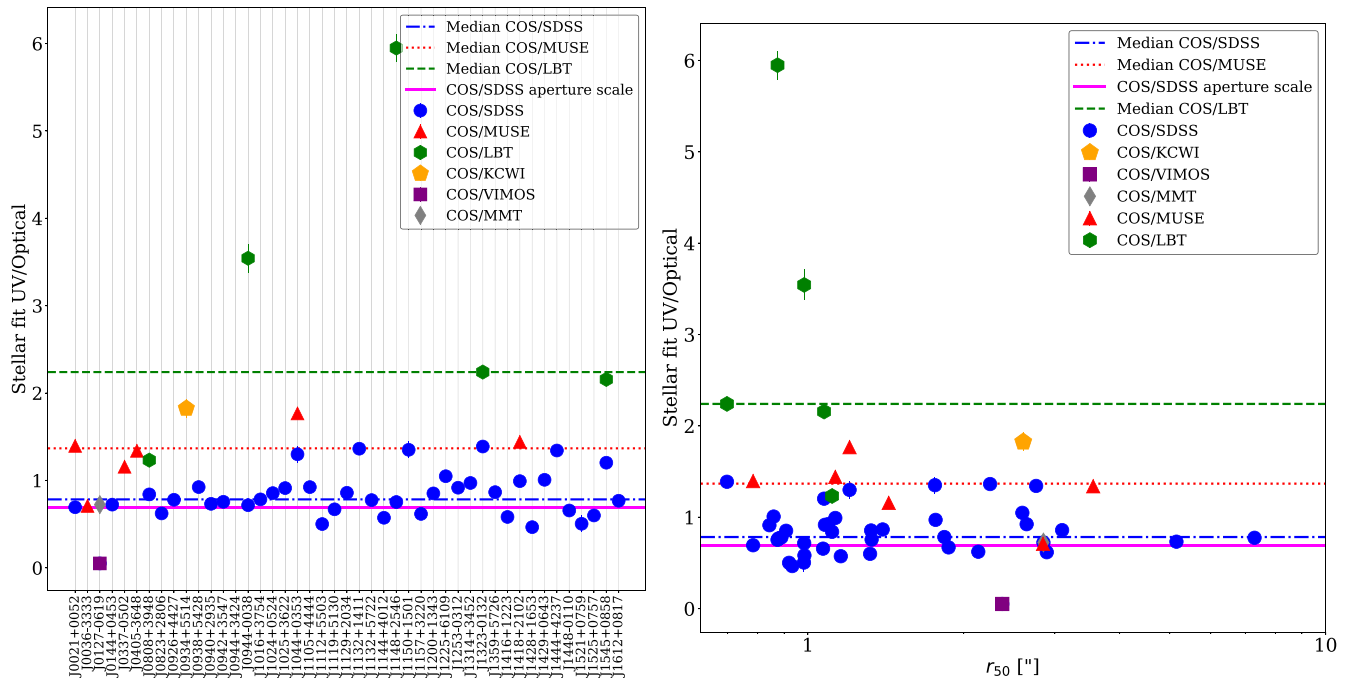


Figure 18. Left panel: UV–optical flux offset for each CLASSY galaxy, obtained from the comparison of extended-UV stellar-continuum fitting and optical stellar-continuum fitting of SDSS (blue circles), MUSE (red triangles), KCWI (gold pentagon), VIMOS (purple square), LBT (green hexagons), and MMT (gray diamond) data. Right panel: UV–optical flux offset as a function of the average half-light radius (r_{50}) taken from Paper I and calculated from Pan-STARRS imaging. The solid magenta horizontal lines are centered at the ratio of the COS/SDSS aperture (i.e., $(2''.5/3'')^2$), while the dashed–dotted blue, dotted red, and dashed green horizontal lines show the median UV–optical flux offsets for the SDSS, MUSE, and LBT spectra, respectively. The uncertainties are shown for all the displayed quantities.

play. Furthermore, in the right panel of Figure 18 we show the UV–optical offset as a function of r_{50} , and reassuringly we notice that there is no correlation between the two (Pearson factor of ~ 0.02 , with p value of ~ 0.90). The dotted red and dashed green horizontal lines in both the left and right panels of Figure 18 show the median UV–optical flux offsets for the MUSE and LBT spectra, respectively. In particular, the COS and MUSE–KCWI–VIMOS data are aperture matched. Indeed, these optical spectra were obtained by selecting the same aperture and position of COS (see Section 2), and thus the difference in aperture size can be completely ruled out as the origin of the flux offset. Nevertheless, the flux offset calculated can be far different than 1, down to ~ 0.05 for the VIMOS data and up to ~ 1.95 for the KCWI, and with values closer to ~ 1 for MUSE. In these cases, apart from flux calibration issues, there are other effects within the COS aperture that may cause a flux offset here, such as vignetting (see Paper II for details).

We stress that, as already reported in Section 3.1, the C&B models include the nebular continuum. Specifically, the nebular continuum emits significantly in the UV blueward of the Balmer break, accounting for $\sim 5\%$ – 10% of the total flux in the range 900–1800 Å and up to $\sim 20\%$ in the range 1800–4000 Å (Byler et al. 2017), increasing the overall continuum level. Also, its impact increases if the gas is characterized by a high ionization parameter and low metallicity, typical of CLASSY objects (see, e.g., Figure 12 of Byler et al. (2017)). Therefore, it is fundamental to take its contribution into account for our

comparison. A caveat of our approach is that in the UV stellar-continuum best fit, we fixed the ionization parameter to $\log(U) = -2.5$, which sets the overall intensity of the nebular continuum spectrum, as recombination emission depends on the number of incident photons (Byler et al. 2017). However, we tested to what extent the variation in the stellar population ionization parameter in the range $[-3; -1]$ could influence the nebular continuum shape to estimate the UV–optical offset, finding minimal variations (< 0.05 dex compared to the case with $\log(U) = -2.5$) in the 4000–6000 Å wavelength range considered for the comparison. Overall, we conclude that the observed UV–optical flux offsets are primarily due to systematic effects of the instruments such as the COS aperture vignetting and/or uncertainties in the flux calibration.

To summarize, the need to use hybrid line ratios such as $\text{O III } \lambda 1666 / [\text{O III}] \lambda 4363$ from UV and optical spectra, where each line is measured using different instruments, makes it essential to align the continuum fluxes using scaling factors. Deriving this scaling factor is not trivial, as it is not related to a single cause such as the aperture difference but could instead be due to a combination of instrumental systematics beyond our control (e.g., flux calibration, vignetting). Therefore, we consider the method described above as our best avenue in estimating this important flux offset. This offset is reported in Table 5 for the first five galaxies of the CLASSY sample, as an example. The complete table covering all CLASSY galaxies is available on the [CLASSY MAST Webpage](#).

Appendix B UV Emission-line Fits

In Figures 19–23 we show each of the UV emission-line detections (i.e., corresponding to $S/N > 3$) for N IV] $\lambda\lambda 1483,87$, He II $\lambda 1640$, O III] $\lambda\lambda 1661,6$, [N III] $\lambda 1750$, and Si III] $\lambda\lambda 1883,92$. The analog figures for C IV $\lambda\lambda 1548,51$ and C III] $\lambda\lambda 1907,09$ are shown in Section 3.2.3 (Figure 2). The observed flux and the best-fit model are shown in black and red, respectively, while their uncertainties are given by the gray and red shades. The dashed vertical lines indicate the position of the emission features according to the literature z , reported in Table 1. In each figure, the

color of the frames indicates which data set and binning are used for the fit: HR rebinned of 15 pixels spectra in blue, HR rebinned of 30 in cyan, MR rebinned of 6 in dark green, MR rebinned of 12 in light green. The dereddened fluxes of the fitted UV lines (expressed in $10^{-15} \text{ erg s}^{-1} \text{ cm}^{-2}$) and the equivalent widths (in \AA) shown in this paper are reported in Table 4 for the first five galaxies of the CLASSY sample, as an example. The complete table covering all CLASSY galaxies is available on the [CLASSY MAST Webpage](#). The $E(B - V)$ taken into account (see Sections 4.1 and 5.1) is also reported. The fluxes for undetected lines are given as less than their 3σ upper limits.

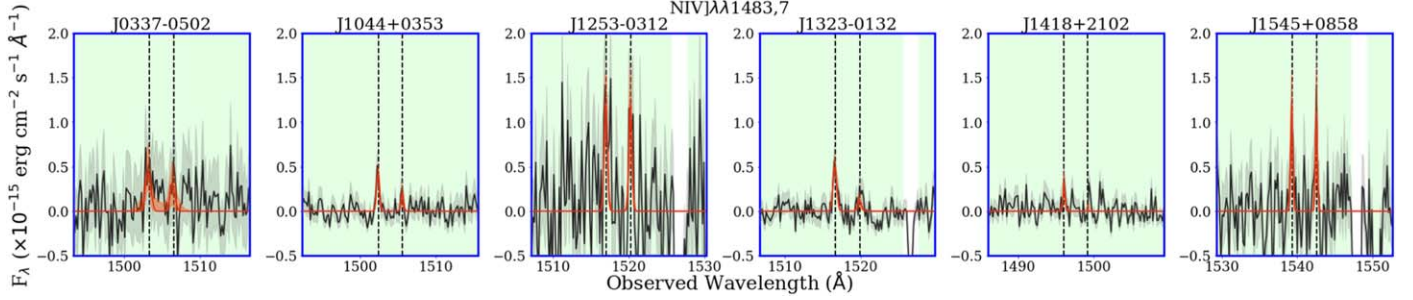


Figure 19. Fit of the N IV] $\lambda\lambda 1483,87$ emission-line doublet, with one of the lines detected with a $S/N > 3$ in 6 out of 44 galaxies. The observed flux and the best-fit model are shown in black and red, respectively, while their uncertainties are given by the gray and red shades. The black dashed vertical lines indicate the line positions, taking z_{lit} into account.

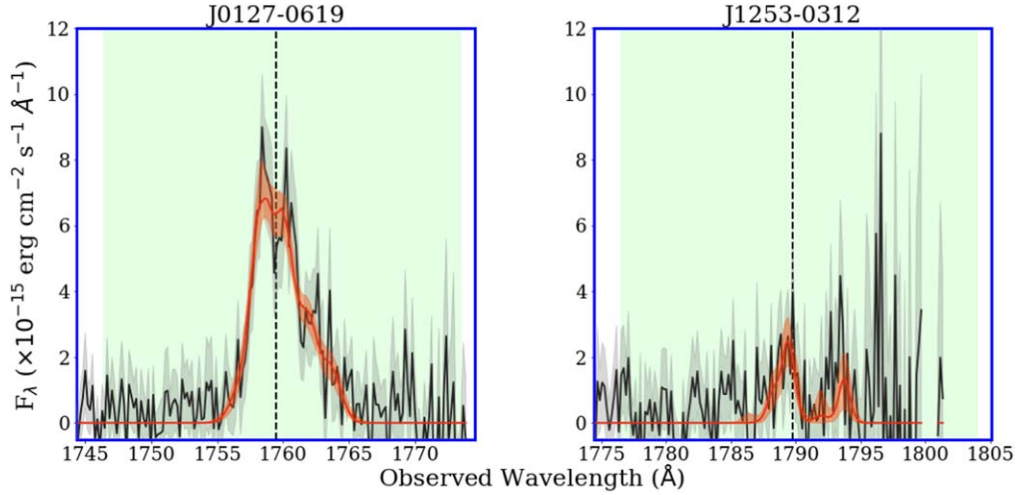


Figure 20. Same as Figure 19 for the [N III] $\lambda 1750$ multiplet in the CLASSY survey detected with a $S/N > 3$ in 2 out of 44 galaxies.

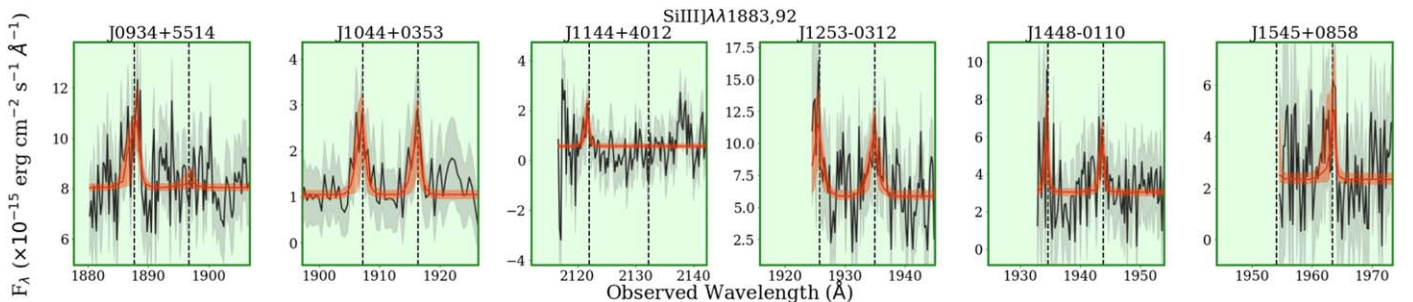


Figure 21. Same as Figure 19 for the Si III] $\lambda\lambda 1883,92$ doublet, with one of the lines detected with a $S/N > 3$ in 6 out of 44 galaxies.

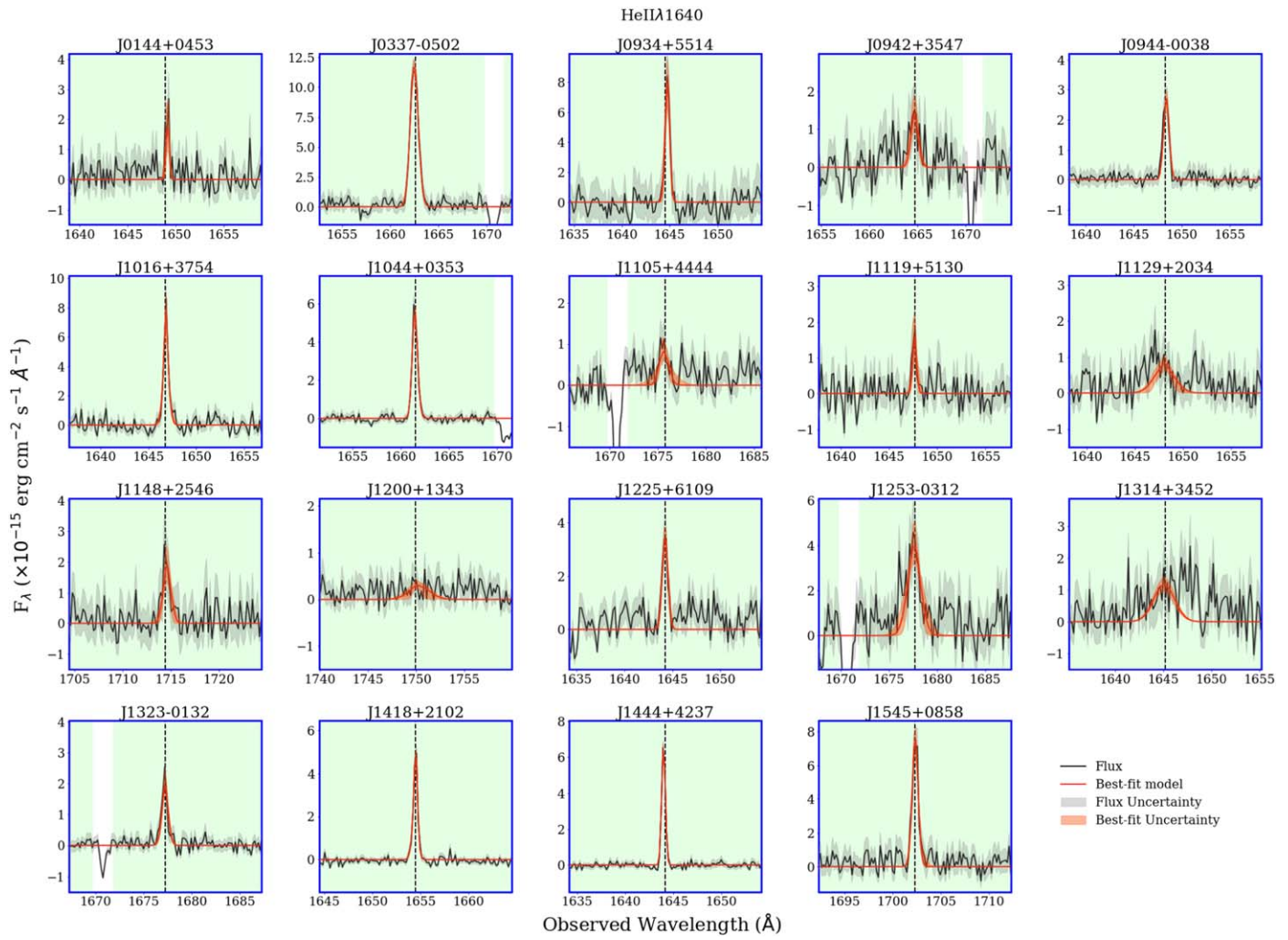


Figure 22. Same as Figure 19 for the He II $\lambda 1640$ emission line in emission, detected with a $S/N > 3$ in 19 out of 44 galaxies.

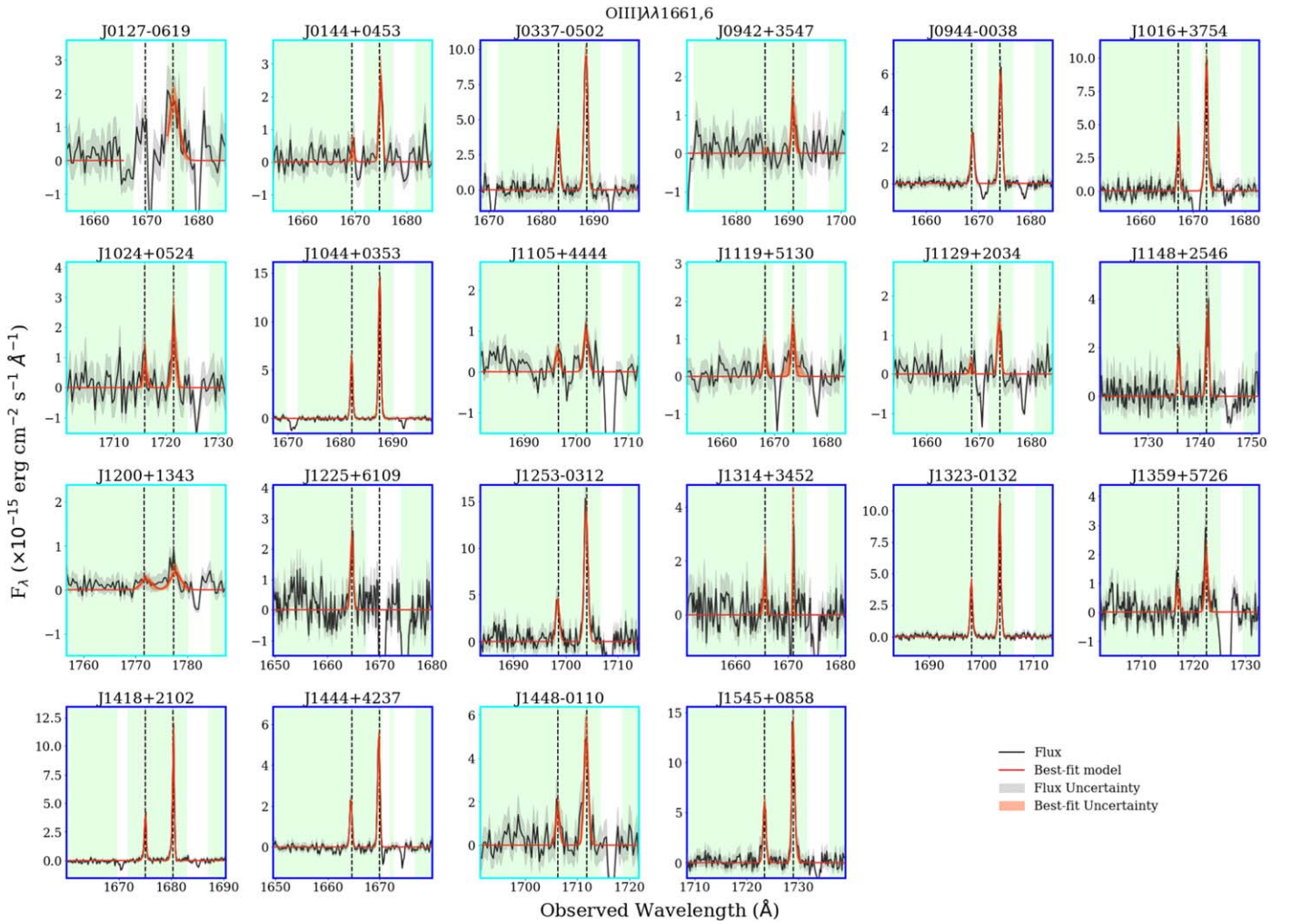


Figure 23. Same as Figure 19 for [O III] $\lambda 1661,6$ emission line in the CLASSY survey detected with a $S/N > 3$ in 22 out of 44 galaxies.

Table 4
FUV Emission-line Fluxes from HST/COS for the First Five Galaxies of the CLASSY Survey

Ion	J0021+0052	J0036-3333	J0127-0619	J0144+0453	J0337-0502
Si II $\lambda 1265.00$	5.84 ± 2.07	144.04 ± 18.59	...	0.98 ± 0.28	...
Si IV $\lambda 1393.76$
O IV $\lambda 1401.16$	<1.31
Si IV $\lambda 1402.77$	1.23 ± 0.39
O IV $\lambda 1404.81$	<0.42	2.18 ± 0.53
S IV $\lambda 1406.02$
O IV $\lambda 1407.38$...	<23.98	0.98 ± 0.32
O IV $\lambda 1410.00$...	33.76 ± 12.23
S IV $\lambda 1416.89$
S IV $\lambda 1423.85$	<0.60
N IV] $\lambda 1483.33$	0.89 ± 0.34
N IV] $\lambda 1486.50$
Si II* $\lambda 1533.43$	3.53 ± 1.22	21.59 ± 6.90	33.66 ± 9.75	<0.80	...
C IV $\lambda 1548.19$	<0.45	15.99 ± 2.20
C IV $\lambda 1550.77$	<0.51	6.86 ± 1.26
He II $\lambda 1640.42$	<51.99	1.27 ± 0.37	18.30 ± 3.17
O III] $\lambda 1660.81$	<1.03	5.53 ± 1.67
O III] $\lambda 1666.15$...	<24.27	161.28 ± 35.14	2.56 ± 0.61	13.21 ± 2.70
[Si III] $\lambda 1883.00$
Si III] $\lambda 1892.03$	<4.24	...	<182.77
C III] $\lambda 1906.68$	1185.31 ± 146.28	8.61 ± 2.66	14.73 ± 3.40
[C III] $\lambda 1908.72$	<4.04	<105.54	773.70 ± 68.09	6.22 ± 1.69	10.46 ± 1.55
EW(C IV)	2.13 ± 0.24
EW(He II)	0.63 ± 0.18	1.97 ± 0.34
EW(O III] $\lambda 1666$)	1.23 ± 0.27	1.33 ± 0.31	1.49 ± 0.31
EW(C III)	20.58 ± 1.68	12.44 ± 2.61	4.02 ± 0.60

Note. The complete table covering all CLASSY galaxies is available on the [CLASSY MAST Webpage](#). The fluxes are expressed in $10^{-15} \text{ erg s}^{-1} \text{ cm}^{-2}$ and are corrected for the dust attenuation using the Reddy et al. (2016) law. Fluxes for undetected lines are given as less than their 3σ upper limits. The EWs are in \AA .

Appendix C Optical Emission-line Fits

In Table 5 we report the fluxes of the fitted optical lines (expressed in 10^{-15} erg s $^{-1}$ cm $^{-2}$) and the H α EWs (in \AA) for the first five galaxies of the CLASSY sample. The complete table covering all CLASSY galaxies is available on the

CLASSY MAST Webpage. The fluxes for undetected lines are given as less than their 3σ upper limits. We also report the telescope and instrument taken into account for each galaxy, and the UV–optical flux offsets calculated and used to correct the optical line fluxes (see Appendix A). The $E(B - V)$ taken into account (see Sections 4.1 and 5.1) is reported in Table 4.

Table 5
Optical Emission-line Fluxes for the First Five Galaxies of the CLASSY Survey

Ion	J0021+0052	J0036-3333	J0127-0619	J0144+0453	J0337-0502
[O II] λ 3727.092	14.55 \pm 0.45
[O II] λ 3729.875	16.39 \pm 0.05
[S II] λ 4069.749	0.52 \pm 0.05
H δ λ 4102.892	5.20 \pm 0.16
H γ λ 4341.691	9.64 \pm 0.19	...	155.11 \pm 2.04
[O III] λ 4364.436	0.50 \pm 0.10
[Fe III] λ 4659.35	0.32 \pm 0.04	0.61 \pm 0.00	9.78 \pm 0.60	...	0.10 \pm 0.00
He II λ 4687.015	0.34 \pm 0.04	0.25 \pm 0.01	4.94 \pm 0.54	<0.40	1.42 \pm 0.00
[Fe III] λ 4702.85	<0.12	0.12 \pm 0.00	4.80 \pm 0.48	...	0.03 \pm 0.00
[Ar IV] λ 4712.69	...	0.02 \pm 0.01	0.41 \pm 0.00
[Ar IV] λ 4741.49	0.34 \pm 0.00
H β λ 4862.691	22.71 \pm 0.30	30.04 \pm 0.01	423.38 \pm 3.33	<5.22	38.64 \pm 0.02
[O III] λ 5008.240	110.54 \pm 1.00	94.62 \pm 0.02	1553.65 \pm 4.44	26.42 \pm 5.62	133.51 \pm 0.04
[Cl III] λ 5519.25	...	0.12 \pm 0.00	1.86 \pm 0.28	...	0.03 \pm 0.00
[Cl III] λ 5539.43	<0.09	0.15 \pm 0.00	<1.39	...	0.01 \pm 0.00
[N II] λ 5756.240	...	0.69 \pm 0.00
[O I] λ 6302.046	1.13 \pm 0.06	2.70 \pm 0.00	18.77 \pm 0.67	...	0.28 \pm 0.00
[S II] λ 6313.8	0.29 \pm 0.05	0.37 \pm 0.00	9.66 \pm 1.13	...	0.27 \pm 0.00
H α λ 6564.632	71.82 \pm 0.75	125.23 \pm 0.03	1934.23 \pm 19.79	50.76 \pm 2.07	89.08 \pm 0.03
[N II] λ 6585.271	3.76 \pm 0.11	21.81 \pm 0.01	125.97 \pm 3.15	...	0.44 \pm 0.00
[S II] λ 6718.294	4.13 \pm 0.10	13.85 \pm 0.01	108.59 \pm 0.77	2.24 \pm 0.15	0.79 \pm 0.00
[S II] λ 6732.674	2.98 \pm 0.09	9.05 \pm 0.01	99.22 \pm 0.71	1.50 \pm 0.32	0.64 \pm 0.00
[O II] λ 7322.01	0.58 \pm 0.06	1.18 \pm 0.00	24.29 \pm 1.51	...	0.22 \pm 0.00
[O II] λ 7332.0	0.45 \pm 0.07	0.90 \pm 0.00	20.00 \pm 1.48	...	0.17 \pm 0.00
[Ar III] λ 7137.8	1.96 \pm 0.07	3.77 \pm 0.00	61.35 \pm 1.29	...	0.81 \pm 0.00
[S III] λ 9071.1	...	9.64 \pm 0.01	1.28 \pm 0.00
EW(H α)	385.94 \pm 4.06	125.95 \pm 0.03	512.35 \pm 5.24	0.00 \pm 0.00	611.40 \pm 0.22
Instrument/Telescope	APO/SDSS	VLT/MUSE	VLT/VIMOS	MMT	VLT/MUSE
UV-Opt offset	0.69 \pm 0.05	0.71 \pm 0.01	0.05 \pm 0.01	0.73 \pm 0.02	1.16 \pm 0.01

Note. The complete table covering all CLASSY galaxies is available on the CLASSY MAST Webpage. The fluxes are expressed in 10^{-15} erg s $^{-1}$ cm $^{-2}$ corrected for dust attenuation using the Cardelli et al. (1989) law, but not multiplied yet by the UV–optical offset, which is also reported. Fluxes for undetected lines are given as less than their 3σ upper limits. The EW(H α) is expressed in \AA . The last line of each block indicates from which instrument and telescope the data are taken.

Appendix D Interstellar Medium Properties

In Table 6 we report the densities, temperatures, ionization parameters of the low, high- and intermediate-ionization zones,

as well as the $E(B - V)$ used to correct the optical and UV emission lines, and optical and UV metallicities for the first five galaxies of the CLASSY sample.

Table 6
ISM Properties for the First Five CLASSY Galaxies

	J0021+0052	J0036-3333	J0127-0619	J0144+0453	J0337-0502
Low-ionization Zone					
n_e ([S II],[N II])	21 ± 2	...	488 ± 1	...	155 ± 1
n_e ([O II],[N II])
n_e ([S II],[S II])	394 ± 1	...	155 ± 1
n_e ([O II],[S II])
n_e ([S II],[O II])	39 ± 2	...	394 ± 1	...	155 ± 1
n_e ([O II],[O II])
T_e ([S II],[N II])	23763 ± 140
T_e ([O II],[N II])
T_e ([S II],[S II])	15854 ± 149
T_e ([O II],[S II])
T_e ([S II],[O II])	12123 ± 28	...	15854 ± 149
T_e ([O II],[O II])
$T_{e,low-G92}$	11610 ± 11610	...	15854 ± 15854
$\log(U)$ (S3S2)	...	-3.22 ± 0.00	-2.65 ± 0.00
Intermediate-ionization Zone					
n_e ([Cl III],[S III])	...	4119 ± 12	272 ± 2019
n_e ([Fe III],[S III])	31819 ± 461332	2440 ± 507
n_e ([Si III],[S III])
n_e ([C III],[S III])	3308 ± 4532	4258 ± 1067
T_e ([Cl III],[S III])	...	11961 ± 1	15854 ± 149
T_e ([Fe III],[S III])	11610 ± 142	21466 ± 8
T_e ([Si III],[S III])
T_e ([C III],[S III])	15854 ± 149	...	21850 ± 9
$T_{e,int-G92}$	11610 ± 142	...	15854 ± 149
$\log(U)$ (O3O2)	-2.90 ± 0.01	-3.08 ± 0.00	-3.29 ± 0.02	-2.99 ± 0.08	-2.38 ± 0.00
High-ionization Zone					
n_e ([S II],[O III])	39 ± 1	...	415 ± 1	...	155 ± 1
n_e ([S II],[O III] _{UV})	645 ± 2	...	180 ± 1
n_e ([N IV],[O III])
n_e ([N IV],[O III] _{UV})
n_e ([Ar IV],[O III])	1107 ± 5
n_e ([Ar IV],[O III] _{UV})	1003 ± 7
T_e ([S II],[O III])	12300 ± 12
T_e ([S II],[O III] _{UV})	55513 ± 849	23172 ± 148	19330 ± 63
T_e ([N IV],[O III])
T_e ([N IV],[O III] _{UV})	19330 ± 62
T_e ([Ar IV],[O III])
T_e ([Ar IV],[O III] _{UV})	19323 ± 63
$\log(U)$ (Ar4Ar3)	-2.54 ± 0.03	-3.06 ± 0.12	-1.57 ± 0.01
$E(B-V)$ (100 cm^{-3} ; 10^4 K)	0.12 ± 0.02	0.38 ± 0.00	0.47 ± 0.01	0.04 ± 0.03	0.05 ± 0.01
$E(B-V)$	0.14 ± 0.01	0.38 ± 0.00	0.50 ± 0.01	0.04 ± 0.01	0.05 ± 0.00
$(12+\log(O/H))$ ([S II],[O III] _{UV})	7.37 ± 0.01
$(12+\log(O/H))$ ([Ar IV],[O III])
$(12+\log(O/H))$ ([Ar IV],[O III] _{UV})	7.37 ± 0.01
$(12+\log(O/H))$ ([N IV],[O III])
$(12+\log(O/H))$ ([N IV],[O III] _{UV})
$(12+\log(O/H))_{\text{He2}}$...	8.47	8.53	8.05	7.24
$(12+\log(O/H))_{\text{Si3}}$

Note. The complete table covering all CLASSY galaxies is available on the [CLASSY MAST Webpage](#). n_e , T_e , and $\log(U)$ derived for the different ionization zones, where the first and second species listed in parenthesis indicate the diagnostics used to calculate n_e and T_e , respectively (see Section 4 for details). $T_{e,low-G92}$ and $T_{e,int-G92}$ are the low- and intermediate-ionization temperatures derived with the Garnett (1992) relations, as explained in Section 4.3. $E(B - V)$ derived assuming $n_e \sim 100 \text{ cm}^{-3}$ and $T_e = 10^4 \text{ K}$, the $E(B - V)$ used to correct the optical and UV emission lines, and the different estimates of $12+\log(O/H)$.

ORCID iDs

Matilde Mingozi  <https://orcid.org/0000-0003-2589-762X>
 Bethan L. James  <https://orcid.org/0000-0003-4372-2006>
 Karla Z. Arellano-Córdova  <https://orcid.org/0000-0002-2644-3518>
 Danielle A. Berg  <https://orcid.org/0000-0002-4153-053X>
 Peter Senchyna  <https://orcid.org/0000-0002-9132-6561>
 John Chisholm  <https://orcid.org/0000-0002-0302-2577>
 Jarle Brinchmann  <https://orcid.org/0000-0003-4359-8797>
 Alessandra Aloisi  <https://orcid.org/0000-0003-4137-882X>
 Ricardo O. Amorín  <https://orcid.org/0000-0001-5758-1000>
 Stéphane Charlot  <https://orcid.org/0000-0003-3458-2275>
 Anna Feltre  <https://orcid.org/0000-0001-6865-2871>
 Matthew Hayes  <https://orcid.org/0000-0001-8587-218X>
 Timothy Heckman  <https://orcid.org/0000-0003-1127-7497>
 Alaina Henry  <https://orcid.org/0000-0002-6586-4446>
 Svea Hernandez  <https://orcid.org/0000-0003-4857-8269>
 Nimisha Kumari  <https://orcid.org/0000-0002-5320-2568>
 Claus Leitherer  <https://orcid.org/0000-0003-2685-4488>
 Mario Llerena  <https://orcid.org/0000-0003-1354-4296>
 Crystal L. Martin  <https://orcid.org/0000-0001-9189-7818>
 Themiya Nanayakkara  <https://orcid.org/0000-0003-2804-0648>
 Swara Ravindranath  <https://orcid.org/0000-0002-5269-6527>
 Evan D. Skillman  <https://orcid.org/0000-0003-0605-8732>
 Yuma Sugahara  <https://orcid.org/0000-0001-6958-7856>
 Aida Wofford  <https://orcid.org/0000-0001-8289-3428>
 Xinfeng Xu  <https://orcid.org/0000-0002-9217-7051>

References

- Abazajian, K. N., Adelman-McCarthy, J. K., Agueros, M. A., et al. 2009, *ApJS*, 182, 543
- Acharyya, A., Kewley, L. J., Rigby, J. R., et al. 2019, *MNRAS*, 488, 5862
- Albareti, F. D., Prieto, C. A., Almeida, A., et al. 2017, *ApJS*, 233, 25
- Amorín, R., Fontana, A., Pérez-Montero, E., et al. 2017, *NatAs*, 1, 0052
- Amorín, R., Vílchez, J. M., Hägele, G. F., et al. 2012, *ApJL*, 754, L22
- Arellano-Córdova, K. Z., Esteban, C., Garcia-Rojas, J., & Mendez-Delgado, J. E. 2020, *MNRAS*, 496, 1051
- Arellano-Córdova, K. Z., Mingozi, M., Berg, D. A., et al. 2022, *ApJ*, 935, 74
- Asplund, M., Grevesse, N., Sauval, A. J., & Scott, P. 2009, *ARA&A*, 47, 481
- Astropy Collaboration, Price-Whelan, A. M., Sipőcz, B. M., et al. 2018, *AJ*, 156, 123
- Astropy Collaboration, Robitaille, T. P., Tollerud, E. J., et al. 2013, *A&A*, 558, A33
- Bayliss, M. B., Rigby, J. R., Sharon, K., et al. 2014, *ApJ*, 790, 144
- Berg, D. A., Chisholm, J., Erb, D. K., et al. 2019a, *ApJL*, 878, L3
- Berg, D. A., Chisholm, J., Erb, D. K., et al. 2021, *ApJ*, 922, 170
- Berg, D. A., Erb, D. K., Auger, M. W., Pettini, M., & Brammer, G. B. 2018, *ApJ*, 859, 164
- Berg, D. A., Erb, D. K., Henry, R. B. C., Skillman, E. D., & McQuinn, K. B. W. 2019b, *ApJ*, 874, 93
- Berg, D. A., James, B. L., King, T., et al. 2022, *ApJS*, 261, 31
- Berg, D. A., Skillman, E. D., Croxall, K., et al. 2015, *ApJ*, 806, 16
- Berg, D. A., Skillman, E. D., Henry, R. B. C., Erb, D. K., & Carigi, L. 2016, *ApJ*, 827, 126
- Bian, F., Kewley, L. J., Dopita, M. A., & Juneau, S. 2016, *ApJ*, 822, 62
- Binette, L., Matadamas, R., Hägele, G. F., et al. 2012, *A&A*, 547, A29
- Bosch, G., Hägele, G. F., Amorín, R., et al. 2019, *MNRAS*, 489, 1787
- Bradley, L., Sipőcz, B., Robitaille, T., et al. 2021, *astropy/photutils*: 1.1.0, v1.1.0, Zenodo, doi:10.5281/zenodo.4624996
- Brinchmann, J., Kunth, D., & Durret, F. 2008, *A&A*, 485, 657
- Bruzual, G., & Charlot, S. 2003, *MNRAS*, 344, 1000
- Byler, N., Dalcanton, J. J., Conroy, C., et al. 2018, *ApJ*, 863, 14
- Byler, N., Dalcanton, J. J., Conroy, C., & Johnson, B. D. 2017, *ApJ*, 840, 44
- Byler, N., Kewley, L. J., Rigby, J. R., et al. 2020, *ApJ*, 893, 1
- Calzetti, D. 1997, in *AIP Conf. Ser.* 408, *The Ultraviolet Universe at Low and High Redshift*, ed. W. H. Waller (Melville, NY: AIP), 403
- Calzetti, D., Armus, L., Bohlin, R. C., et al. 2000, *ApJ*, 533, 682
- Calzetti, D., Kinney, A. L., & Storchi-Bergmann, T. 1994, *ApJ*, 429, 582
- Cappellari, M., Scott, N., Alatalo, K., et al. 2013, *MNRAS*, 432, 1709
- Cardelli, J. A., Clayton, G. C., & Mathis, J. S. 1989, *ApJ*, 345, 245
- Chabrier, G. 2003, *PASP*, 115, 763
- Chevallard, J., & Charlot, S. 2016, *MNRAS*, 462, 1415
- Chiappini, C., Romano, D., & Matteucci, F. 2003, *MNRAS*, 339, 63
- Chisholm, J., Rigby, J. R., Bayliss, M., et al. 2019, *ApJ*, 882, 182
- Christensen, L., Laursen, P., Richard, J., et al. 2012, *MNRAS*, 427, 1973
- Crowther, P. A. 2007, *ARA&A*, 45, 177
- Crowther, P. A., & Smith, L. J. 1997, *A&A*, 320, 500
- Curti, M., Cresci, G., Mannucci, F., et al. 2017, *MNRAS*, 465, 1384
- Curti, M., D'Eugenio, F., Carniani, S., et al. 2022, *MNRAS*, in press
- Dopita, M. A., & Evans, I. N. 1986, *ApJ*, 307, 431
- Dopita, M. A., Fischera, J., Sutherland, R. S., et al. 2006, *ApJ*, 647, 244
- Dopita, M. A., Rich, J., Vogt, F. P. A., et al. 2014, *Ap&SS*, 350, 741
- Eisenstein, D. J., Weinberg, D. H., Agol, E., et al. 2011, *AJ*, 142, 72
- Eldridge, J. J., & Stanway, E. R. 2016, *MNRAS*, 462, 3302
- Erb, D. K., Pettini, M., Shapley, A. E., et al. 2010, *ApJ*, 719, 1168
- Erb, D. K., Steidel, C. C., Shapley, A. E., et al. 2006, *ApJ*, 646, 107
- Feltre, A., Charlot, S., & Gutkin, J. 2016, *MNRAS*, 456, 3354
- Ferland, G. J., Porter, R. L., van Hoof, P. A. M., et al. 2013, *RMxAA*, 49, 137
- Fernandes, I. F., Gruenwald, R., & Viegas, S. M. 2005b, *MNRAS*, 364, 674
- Fernandes, R. C., Mateus, A., Sodre, L., Stasinska, G., & Gomes, J. M. 2005a, *MNRAS*, 358, 363
- Fosbury, R. A. E., Villar-Martín, M., Humphrey, A., et al. 2003, *ApJ*, 596, 797
- Garnett, D. R. 1990, *ApJ*, 363, 142
- Garnett, D. R. 1992, *AJ*, 103, 1330
- Garnett, D. R., Edmunds, M. G., Henry, R. B. C., Pagel, B. E. J., & Skillman, E. D. 2004, *AJ*, 128, 2772
- Garnett, D. R., Skillman, E. D., Dufour, R. J., et al. 1995, *ApJ*, 443, 64
- Geen, S., Pellegrini, E., Bieri, R., & Klessen, R. 2020, *MNRAS*, 492, 915
- Giuliani, J. L., Jr. 1981, *ApJ*, 245, 903
- Gordon, K. D., & Clayton, G. C. 1998, *ApJ*, 500, 816
- Gordon, K. D., Clayton, G. C., Misselt, K. A., Landolt, A. U., & Wolff, M. J. 2003, *ApJ*, 594, 279
- Green, G. M. 2018, *JOSS*, 3, 695
- Green, G. M., Schlafly, E. F., Finkbeiner, D. P., et al. 2015, *ApJ*, 810, 25
- Gronke, M., & Dijkstra, M. 2014, *MNRAS*, 444, 1095
- Guseva, N. G., Izotov, Y. I., Fricke, K. J., & Henkel, C. 2017, *A&A*, 599, A65
- Guseva, N. G., Izotov, Y. I., Stasińska, G., et al. 2011, *A&A*, 529, A149
- Gutkin, J., Charlot, S., & Bruzual, G. 2016, *MNRAS*, 462, 1757
- Hainline, K. N., Shapley, A. E., Kornei, K. A., et al. 2009, *ApJ*, 701, 52
- Henry, R. B. C., Edmunds, M. G., & Köppen, J. 2000, *ApJ*, 541, 660
- Hogarth, L., Amorín, R., Vílchez, J. M., et al. 2020, *MNRAS*, 494, 3541
- Hoopes, C. G., & Walterbos, R. A. M. 2003, *ApJ*, 586, 902
- Izotov, Y. I., & Thuan, T. X. 1999, *ApJ*, 511, 639
- Izotov, Y. I., & Thuan, T. X. 2007, *ApJ*, 665, 1115
- James, B. L., Auger, M., Pettini, M., et al. 2018, *MNRAS*, 476, 1726
- James, B. L., Berg, D. A., King, T., et al. 2022, *ApJS*, 262, 37
- James, B. L., Pettini, M., Christensen, L., et al. 2014, *MNRAS*, 440, 1794
- James, B. L., Tsamis, Y. G., Barlow, M. J., et al. 2009, *MNRAS*, 398, 2
- Jaskot, A. E., & Oey, M. S. 2013, *ApJ*, 766, 91
- Jaskot, A. E., & Ravindranath, S. 2016, *ApJ*, 833, 136
- Juan de Dios, L., & Rodríguez, M. 2017, *MNRAS*, 469, 1036
- Juan de Dios, L., & Rodríguez, M. 2021, *MNRAS*, 507, 5331
- JWST User Documentation 2016, JWST User Documentation (JDox), JWST Kaasinen, M., Kewley, L., Bian, F., et al. 2018, *MNRAS*, 477, 5568
- Kaplan, K. F., Jogee, S., Kewley, L., et al. 2016, *MNRAS*, 462, 1642
- Kashino, D., Silverman, J. D., Rodighiero, G., et al. 2013, *ApJL*, 777, L8
- Keenan, F. P., Dufton, P. L., Feibelman, W. A., et al. 1994, *ApJ*, 423, 882
- Keenan, F. P., Ramsbottom, C. A., Bell, K. L., et al. 1995, *ApJ*, 438, 500
- Kelly, B. C. 2007, *ApJ*, 665, 1489
- Kennicutt, R. C., Jr., Bresolin, F., & Garnett, D. R. 2003, *ApJ*, 591, 801
- Kewley, L. J., & Dopita, M. A. 2002, *ApJS*, 142, 35
- Kewley, L. J., Nicholls, D. C., & Sutherland, R. S. 2019, *ARA&A*, 57, 511
- Kewley, L. J., Zahid, H. J., Geller, M. J., et al. 2015, *ApJL*, 812, L20
- Kluyver, T., Ragan-Kelley, B., Perez, F., et al. 2016, in *Positioning and Power in Academic Publishing: Players, Agents and Agendas*, ed. F. Loizides & B. Schmidt (Amsterdam: IOS Press), 87
- Kojima, T., Ouchi, M., Nakajima, K., et al. 2017, *PASJ*, 69, 44
- Komarova, L., Oey, M. S., Krumholz, M. R., et al. 2021, *ApJL*, 920, L46
- Kroupa, P. 2001, *MNRAS*, 322, 231
- Leitherer, C. 2005, in *AIP Conf. Ser.* 783, *The Evolution of Starbursts*, ed. S. Hüttemeister et al. (Melville, NY: AIP), 280
- Leitherer, C., Ortiz Otálvaro, P. A., Bresolin, F. o., et al. 2010, *ApJS*, 189, 309

- Leitherer, C., Schaerer, D., Goldader, J. D., et al. 1999, *ApJS*, **123**, 3
- Lin, X., Cai, Z., Zou, S., et al. 2022, arXiv:2209.03376
- Llerena, M., Amorín, R., Cullen, F., et al. 2022, *A&A*, **659**, A16
- Luridiana, V., Morisset, C., & Shaw, R. A. 2012, in IAU Symp. 283 Planetary Nebulae: An Eye to the Future (Cambridge: Cambridge Univ. Press) 422
- Luridiana, V., Morisset, C., & Shaw, R. A. 2015, *A&A*, **573**, A42
- Madau, P., & Haardt, F. 2015, *ApJL*, **813**, L8
- Maeder, A. 1992, *A&A*, **264**, 105
- Mainali, R., Kollmeier, J. A., Stark, D. P., et al. 2017, *ApJL*, **836**, L14
- Mainali, R., Zitrin, A., Stark, D. P., et al. 2018, *MNRAS*, **479**, 1180
- Maiolino, R., & Mannucci, F. 2019, *A&ARv*, **27**, 3
- Markwardt, C. B. 2009, in ASP Conf. Ser. 411, Astronomical Data Analysis Software and Systems XVIII, ed. D. A. Bohlender, D. Durand, & P. Dowler (San Francisco, CA: ASP), 251
- Maseda, M. V., Brinchmann, J., Franx, M., et al. 2017, *A&A*, **608**, A4
- McLure, R. J., Pentericci, L., Cimatti, A., et al. 2018, *MNRAS*, **479**, 25
- Méndez-Delgado, J. E., Esteban, C., García-Rojas, J., et al. 2021, *MNRAS*, **502**, 1703
- Michel-Dansac, L., Blaizot, J., Garel, T., et al. 2020, *A&A*, **635**, A154
- Mingozzi, M., Belfiore, F., Cresci, G., et al. 2020, *A&A*, **636**, A42
- Morisset, C., Luridiana, V., García-Rojas, J., et al. 2020, *Atoms*, **8**, 66
- Nagao, T., Murayama, T., & Taniguchi, Y. 2001, *ApJ*, **549**, 155
- Nakajima, K., & Ouchi, M. 2014, *MNRAS*, **442**, 900
- Nakajima, K., Schaerer, D., Le Fèvre, O., et al. 2018, *A&A*, **612**, A94
- Nanayakkara, T., Brinchmann, J., Boogaard, L., et al. 2019, *A&A*, **624**, A89
- Nicholls, D. C., Kewley, L. J., & Sutherland, R. S. 2020, *PASP*, **132**, 033001
- Osterbrock, D. E. 1989, *Astrophysics of Gaseous Nebulae and Active Galactic Nuclei* (Sausalito, CA: University Science Books)
- Osterbrock, D. E., & Ferland, G. J. 2006, *Astrophysics of Gaseous Nebulae and Active Galactic Nuclei* (Sausalito, CA: University Science Books)
- Pannella, M., Elbaz, D., Daddi, E., et al. 2015, *ApJ*, **807**, 141
- Patrício, V., Christensen, L., Rhodin, H., Canameras, R., & Lara-Lopez, M. A. 2018, *MNRAS*, **481**, 3520
- Patrício, V., Richard, J., Verhamme, A., et al. 2016, *MNRAS*, **456**, 4191
- Pellegrini, E. W., Rahner, D., Reissl, S., et al. 2020, *MNRAS*, **496**, 339
- Pérez-Montero, E., & Amorín, R. 2017, *MNRAS*, **467**, 1287
- Plat, A., Charlot, S., Bruzual, G., et al. 2019, *MNRAS*, **490**, 978
- Price, S. H., Kriek, M., Brammer, G. B., et al. 2014, *ApJ*, **788**, 86
- Puglisi, A., Rodighiero, G., Franceschini, A., et al. 2016, *A&A*, **586**, A83
- Qin, J., Zheng, X. Z., Wuyts, S., Pan, Z., & Ren, J. 2019, *ApJ*, **886**, 28
- Quider, A. M., Pettini, M., Shapley, A. E., & Steidel, C. C. 2009, *MNRAS*, **398**, 1263
- Raiter, A., Fosbury, R. A. E., & Teimoorinia, H. 2010, *A&A*, **510**, A109
- Ravindranath, S., Monroe, T., Jaskot, A., Ferguson, H. C., & Tumlinson, J. 2020, *ApJ*, **896**, 170
- Reddy, N. A., Erb, D. K., Pettini, M., Steidel, C. C., & Shapley, A. E. 2010, *ApJ*, **712**, 1070
- Reddy, N. A., Kriek, M., Shapley, A. E., et al. 2015, *ApJ*, **806**, 259
- Reddy, N. A., Steidel, C. C., Pettini, M., & Bogosavljevic, M. 2016, *ApJ*, **828**, 107
- Rickards Vaught, R. J., Sandstrom, K. M., & Hunt, L. K. 2021, *ApJL*, **911**, L17
- Rigby, J. R., Bayliss, M. B., Gladders, M. D., et al. 2015, *ApJL*, **814**, L6
- Rigby, J. R., Bayliss, M. B., Sharon, K., et al. 2018, *AJ*, **155**, 104
- Rigby, J. R., Florian, M., Acharyya, A., et al. 2021, *ApJ*, **908**, 154
- Robertson, B. E., Ellis, R. S., Furlanetto, S. R., & Dunlop, J. S. 2015, *ApJL*, **802**, L19
- Rousseuw, P. J., & Van Driessen, K. 2006, *Data Min. Knowl. Discov.*, **12**, 29
- Sanders, R. L., Shapley, A. E., Reddy, N. A., et al. 2020, *MNRAS*, **491**, 1427
- Scarlata, C., & Panagia, N. 2015, *ApJ*, **801**, 43
- Schaerer, D., Izotov, Y. I., Worseck, G., et al. 2022, *A&A*, **658**, L11
- Schmidt, K. B., Huang, K.-H., Treu, T., et al. 2017, *ApJ*, **839**, 17
- Schmidt, K. B., Kerutt, J., Wisotzki, L., et al. 2021, *A&A*, **654**, A80
- Senchyna, P., & Stark, D. P. 2019, *MNRAS*, **484**, 1270
- Senchyna, P., Stark, D. P., Charlot, S., et al. 2021, *MNRAS*, **503**, 6112
- Senchyna, P., Stark, D. P., Charlot, S., et al. 2022, *ApJ*, **930**, 105
- Senchyna, P., Stark, D. P., Chevallard, J., et al. 2019, *MNRAS*, **488**, 3492
- Senchyna, P., Stark, D. P., Vidal-García, A., et al. 2017, *MNRAS*, **472**, 2608
- Shapley, A. E., Steidel, C. C., Pettini, M., & Adelberger, K. L. 2003, *ApJ*, **588**, 65
- Shivaei, I., Reddy, N., Rieke, G., et al. 2020, *ApJ*, **899**, 117
- Shivaei, I., Reddy, N. A., Shapley, A. E., et al. 2015, *ApJ*, **815**, 98
- Skillman, E. D. 1998, in *Stellar Astrophysics for the Local Group: VIII Canary Islands Winter School of Astrophysics*, ed. A. Aparicio, A. Herrero, & F. Sánchez (Cambridge: Cambridge Univ. Press), 457
- Stanghellini, L., & Kaler, J. B. 1989, *ApJ*, **343**, 811
- Stanway, E. R., Eldridge, J. J., & Becker, G. D. 2016, *MNRAS*, **456**, 485
- Stark, D. P. 2016, *ARA&A*, **54**, 761
- Stark, D. P., Richard, J., Charlot, S., et al. 2015, *MNRAS*, **450**, 1846
- Stark, D. P., Richard, J., Siana, B., et al. 2014, *MNRAS*, **445**, 3200
- Steidel, C. C., Rudie, G. C., Strom, A. L., et al. 2014, *ApJ*, **795**, 165
- Steidel, C. C., Strom, A. L., Pettini, M., et al. 2016, *ApJ*, **826**, 159
- STScI Development Team, Lim, P. L., Diaz, R. I., & Laidler, V. 2013, ppsynphot: Synthetic Photometry Software Package, Astrophysics Source Code Library, ascl:1303.023
- Theios, R. L., Steidel, C. C., Strom, A. L., et al. 2019, *ApJ*, **871**, 128
- Thuan, T. X., Izotov, Y. I., & Lipovetsky, V. A. 1996, *ApJ*, **463**, 120
- Treu, T., Roberts-Borsani, G., Bradac, M., et al. 2022, *ApJ*, **935**, 110
- Vanzella, E., De Barros, S., Cupani, G., et al. 2016, *ApJL*, **821**, L27
- Vanzella, E., Grazian, A., Hayes, M., et al. 2010, *A&A*, **513**, A20
- Vidal-García, A., Charlot, S., Bruzual, G., & Hubeny, I. 2017, *MNRAS*, **470**, 3532
- Villar-Martín, M., Cervino, M., & Gonzalez Delgado, R. M. 2004, *MNRAS*, **355**, 1132
- Wei, Z. 1988, *ApL&C*, **27**, 275
- Wild, V., Charlot, S., Brinchmann, J., et al. 2011a, *MNRAS*, **417**, 1760
- Wild, V., Groves, B., Heckman, T., et al. 2011b, *MNRAS*, **410**, 1593
- Wise, J. H., Demchenko, V. G., Halicek, M. T., et al. 2014, *MNRAS*, **442**, 2560
- Wofford, A., Vidal-García, A., Feltre, A., et al. 2021, *MNRAS*, **500**, 2908